SURFACE ACTIVITY OF NEW CLASS OF IONIC NANOPARTICLES AND POLYMER COMPOSITES

A Dissertation

Presented to the Faculty of the Graduate School

of Cornell University

In Partial Fulfillment of the Requirements for the Degree of

Doctor of Philosophy

by

Chiachen Fang

February 2010

SURFACE ACTIVITY OF NEW CLASS OF IONIC NANOPARTICLES AND POLYMER COMPOSITES

Chiachen Fang, Ph. D.

Cornell University 2010

The introduction of nanoparticles into a polymer to form organic-inorganic nanocomposites can greatly enhance the properties of the host polymer. Nanoscale ionic materials, NIMs are new hybrid particles comprised of an inorganic core functionalized with a soft organic shell. Because of the hybrid nature, their properties can be controlled by varying the chemical composition and structure of the core and the canopy. This thesis discusses the synthesis, characterization and bulk and surface properties of a series of new NIMs and NIMs based nanocomposite materials.

A new series of NIMs and NIMs based nanocomposites was synthesized. The surface and bulk properties are characterized and discussed in terms of possible polymer-particle interactions by considering a variety of cores (silica and carbon) and a range of polymer matrices (polystyrene, polyethylene glycol, and PDMS-polyurea copolymers). By tailoring the polarity and surface energy between particle-particle and particle-polymer it is possible to control the geometry, size and dispersion of the nanoparticles in the nanocomposites.

A simple yet general coating method to plasma treated polymeric substrates is also presented. The method is based on electrostatic interactions between the surface functionalized nanoparticles and the charged substrate and leads to stable and solvent resistant multilayer coatings. The coatings render PP hydrophilic and in the case of PP fabric superhydrophilic. The superhydrophilicity is attributed to the topography and

increased roughness of the fabric compared to a planar, smooth substrate.

Finally, a series of new PDMS-polyurea segmented copolymers and nanocomposites was synthesized and their settlement and fouling release behavior was evaluated. The extent of microphase separation and the ability of different domains to crystallize affect the surface and bulk properties of the copolymers. By varying the amount of the soft PDMS segment as well as using nanoparticles we were able to develop copolymers and nanocomposites with moduli spanning a range of more than four orders of magnitude. All copolymers and nanocomposites are stronger (in some cases by orders of magnitude) than PDMS. Surface studies using profilometry and AFM show surface nanostructuring due to phase separation with both nano and microscale features. The morphology can be further modified by the presence of fluorinated groups in the copolymer or the presence of nanoparticles in the nanocomposites. Preliminary studies on settlement and removal of sporelings of Ulva show that the critical pressure to remove 50% of the sporelings is at least comparable and in some cases lower compared to a PDMS elastomer. Additionally a series based on mono-, bifunctional PEG segments shows improved settlement behavior of barnacle larvae compared to standard PDMS. These findings are quite significant as the new coatings combine and at times exceed the fouling release performance of PDMS but are much stronger and tougher.

BIOGRAPHICAL SKETCH

Chiachen Fang was born in Taipei on April 29 1976 and spent most of his time right there. In the summer of 1998, he earned the Bachelor of Science degree from National Chung Hsing University in Chemistry. In the summer of the 2000, he finished his Master of Science degree from National Chiao Tung University in Applied Chemistry. Over the next two years, he served in the Army of the Republic of China. He continued his academia on to study at Cornell University Materials Science and Engineering MS/PhD program, where his work culminated in this thesis.

To my family and friend, past, present and future.

ACKNOWLEDGMENTS

I would like to start by thanking my advisor, Prof. Emmenuel P. Giannelis, for his confidence, support and never-relenting enthusiasm for research. He does a great inspiration during my stay at Cornell. Thanks must also go to my committee members Prof. Christopher Ober, and Prof. Lynden Archer. I would never have able to get through this without your guidance.

There are so many people ever contributed to this work, and companied with me to experience sadness of the depression and delight of the achievement. My dear friends: KM, Sam, Jack couples, Yuwei couples, Robin couples, Chu Chu, Pichun, Poshin, Arthur, Shengwei, Golden, Dongyan, Liangfeng, Haris, Alex, Rafael, Robert, Loan, Nikolaos, Suran, Antonios, Rama, Pat, Aaron, Ian, Evan, Drew, Erik, Lou, Michelle, Melissa, Carol. Research related: John Grazul (microtone, TEM), John Hunt (SEM, optical microscope), Maura (XRD, SAXS); Mick (Keck-SEM), Yuanming (DMA), Jon (AFM), Steven (Instron), David (marine test), Prof. Umbach (profilometer, AFM), Tony (TGA, DSC), Greg Kowalke, Lenora (marine test), Dr. John Finlay and Maureen Callow (marine test). Finally, I have to thank whole my family members Dad, Mom, Granny, and Uncle. You are the sunlight in gloomy Ithaca. Every step I achieved, it's because of you. Allow me to share the glory with you

TABLE OF CONTENTS

LIST OF FIGURES

LIST OF TABLES

LIST OF SCHEMES

LIST OF ABBREVIATIONS

NIMs = Nanoparticles-based Ionic Materials

AFM = Atomic Force Microscopy

HS-30 = Ludox HS-30 Silica

SIT = 3-(trihydroxysilyl)-1-propane sulfuric acid

MWCO = Molecular Weight Cut Off

Ethomeen = $(C_{18}H_{37})N[(CH_2CH_2O)_mH]-[(CH_2CH_2O)_nH]$

Silane3 = N-Trimethyoxysilylpropyl-N,N,N-trimethylammonium chloride

M5 = Cab-O-Sil M-5 Fumed Silica

CBf = Carboxyl-terminated Carbon Black

CBg = Sulfonate-terminated Carbon Black

XTJ-505 = Jeffamine, $CH_3(CH_2CH_2O)_x(CH_2CHCH_3O)_yNH_2$, MW=600, x/y=1/9

M-2070 = Jeffamine, $CH_3(CH_2CH_2O)_x(CH_2CHCH_3O)_yNH_2$, MW=2000, x/y=31/10

$(TMS)_2S$ = Hexamethyldisilathiane

ODE = 1-Octadecene

QDs = Quantum Dots

XTJ-506 = Jeffamine, $CH_3(CH_2CH_2O)_x(CH_2CHCH_3O)_yNH_2$, MW=1000, x/y=19/3

FT-IR = Fourier Transform Infrared Spectroscopy

DLS = Dynamic Light Scattering

DH = Hydrodnamic Diameter

DSC = Differential Scanning Calorimetry

TGA = Thermal Gravimetric Analysis

Tg = Glass Transition Temperature

NP = Nanoparticles

PTFE = Polytetrafluoroethylene

PEO = Polyethylene Oxide

PPO = Polypropylene Oxide

CMC = Critical Micelle Concentration

PDMS = Polydimethylsiloxane

SAM = Self-assembled Monolayer

XPS = X-ray Photo electron Spectroscopy

L-b-L = Layer-by-layer

SiNIMs = Silica-based ionic nanomaterials

CBf-M2070 = Carbon Black-based Ionic nanoparticles

CBg-M2070 = Carbon Black-based Ionic nanoparticles

HS30-SIT-M2070 = Silica-based Ionic nanoparticles

PS = Polystyrene

SEM = Scanning Electron Microscopy

PEG = polyethylene Glycol

MEG = Multiple-exciton-generation

TEM = Transmission Electron Microscopy

VTF = Vogel-tammann-fulcher

PL = Photoluminescence

THF = Tetrahydrofuran

TBT = Tributyltin

AF = Antifouling

FR= Fouling Release

MDI = 4,4-methylenebis (phenyl isocyanate)

F8 = 4,4'-Diaminooctafluorobiphenyl

XTJ502 = Jeffamine, $NH_2CHCH_3CH_2(CH_2CHCH_3O)_x\ (CH_2CH_2O)_y\ (CH_2CHCH_3O)_z$-$NH_2$, MW=2000, y/x+z =39/6

T403 = Jeffamine, $(NH_2\ (CH_2CHCH_3O)_x\ )_3\ (CH_2)_nC_5H_9$, MW=440, 3x=5-6

POSS = Polyhedral Oligomeric Silsesquioxane

DMA = Dynamic Mechanic Analysis

DCA = Dynamic Contact Angle

A12M, A15M, A32M = Pure PDMS-polyurea segment copolymers

A12MF8 = Fluorinated Three-component random copolymer

A12MXTJ502, A12MXTJ506, A12MT403 = PEG containing three-component copolymers

A12MPOSS = POSS-terminated PDMS-polyurea copolymer

A12MPDMS-clay = PDMS-polyurea copolymer blend with PDMS modified clay

A12MNIMs = PDMS-polyurea copolymer blend with ionic nanoparticles

UV-VIS = Ultraviolet-visible Spectroscopy

F3 = 2-Methoxy-5-(trifluoromethyl)aniline

F6 = 4",4"'-(Hexafluoroisopropylidene)bis(4-phenoxyaniline)

25A = Cloisite® 25A is a natural montmorillonite modified with a quaternary ammonium salt

30B = Cloisite® 30B is a natural montmorillonite modified with a quaternary ammonium salt.

Polymer S = Poly(1,4-butylene succinate), extended with 1,6-diisocyanatohexan

CHAPTER 1

GENERAL INTRODUCTION

1.1 Motivation

1.1.1 Nanomaterials

Why nano? Nobel Prize-winner Dr. Horst Störmer once said that the nanoscale is more interesting than the atomic scale because the nanoscale is the first point where we can assemble something; it's not until we start putting atoms together that we can make anything useful.

Nano (from the ancient Greek for "dwarf") is the prefix for units of 10^{-9}. The nano size range is usually defined as smaller than 100 nm. Generally, materials have strikingly different properties at nanoscale, compared with their macro-forms, so the dimension of particles or the scale of their features are the most important attributes of nanomaterials—one of the reasons that "nano" has become so special. Nanoscience is concerned with understanding all the effects that happen at this scale, and nanotechnology controls these unique phenomena and enables novel applications.

Nobel Prize-winner Richard Feynman once said, "I want to build a billion tiny factories—models of each other—which are manufacturing simultaneously. The principles of physics, as far as I can see, do not speak against the possibility of maneuvering things atom by atom. It is not an attempt to violate any laws; it is something, in principle, that can be done; but in practice, it has not been done because we are too big." Feynman's comment was the first time that a scientist gave "nanotechnology" an initial definition.

Nanoparticles, created by living creatures or environmental activity, have existed in the natural world for millions of years. Ancient Egyptians, Greek and

Romans were using lead-based nanoparticles to dye their hair several thousand years ago. Today, pioneering scientists are using lead compounds to generate lead sulfide (PbS) nanocrystals with diameters of less than 5 nanometers, for potential electronic and optical devices. Gold nanoparticles are used in alternative Ayurvedic medicine treatments, which are the traditional medical systems of India and are described in *The Vedas*, the oldest known writing in world. Today, gold nanoparticles are used for detection of colorimetric oligonuceotides, based on their amazing optical properties. This method is outperforming the conventional sequence DNA detection applied in the diagnosis of genetic diseases. There is no doubt that nanotechnology is closely linked with our daily lives and that it has played an important role in human history.

This thesis presents some recent discoveries in nanoparticle-based systems. In particular, it highlights the surface properties of neat nanoparticles and specific nanocomposites systems.

In preparing nanoparticles, stabilizing agents directly affect the stabilization and prevention of uncontrolled growth and aggregation of the nanoparticles. Bourlinos [1-6] utilized primarily charged surface modifiers to develop the first generation of nanoparticle-based ionic materials (NIMs). This is a new family of functionalized nanoparticles, which exhibit liquid-like behavior in the absence of solvents and preserve their nanostructure in the liquid state. The solvent-less nanoparticle fluids are typically synthesized by attaching a corona of flexible organic chains onto an inorganic core. Counter-ion interactions frequently appear in complex fluids [7-11] and colloid assembly [12-19] studies; however, these interactions were for the first time used to stabilize the core-corona-canopy ensemble.

These charged nanoparticles or nanosalts have no volatility and can easily maintain their liquid form in a wide temperature range. They can dissolve in either polar or apolar solvents. The approach is very general and has been successfully

utilized to modify silica(SiO_2), maghemite(γ-Fe_2O_3), ZnO, carbon nanotubes, layer-like organosilicate, anatase(TiO_2), and DNA nanomaterials. These surface functionalized particles are a new class of hybrid nanomaterials that are distinguished from covalently bonded nanocomposites [20-33] or particle suspensions used in layer-by-layer assembly [34-54].

1.1.2 Surface Properties

John B. Hudson gave "surface" the most general definition in his book, Surface science [55]: surfaces or interfaces exist in a system when there is an abrupt change in the system with distance. His idea distinguishes the fundamental differences between the surface and the bulk in an individual system. Surface should be included in all interfaces between solids, polymers, nanostructures, liquids, gases and vacuums.

The most important study of surface phenomena was contributed by Nobel Prize-winner Ivan Langmuir, whose Langmuir adsorption equation relates the adsorption of molecules on a solid surface to gas pressure or concentration of a medium at a constant temperature:

$$\theta = \frac{K\alpha}{1 + K\alpha} \quad ,$$

(Where θ is fractional coverage of the surface; α is concentration of gas or liquid; and K is the equilibrium constant)

In the past forty years, studies of material surface (chemical/physical) properties entered the mainstream of science and technology. Surface properties studied include absorptivity, adsorption, brightness, roughness, frictional resistance, surface temperature, surface tension, surface texture, emissivity, and wettability, amongst others.

The fundamental research of surface properties on wettability, topography and pattern formation[56-61], superhydrophilic surfaces [62-64], polymer adsorption [65], silane based covalently attached monolayers [66,67] (Fig. 1.1), polymer and inorganic surface modification [68-71], adhesion and friction, and molecular dynamics in confined geometry [72-75] have influenced material property studies.

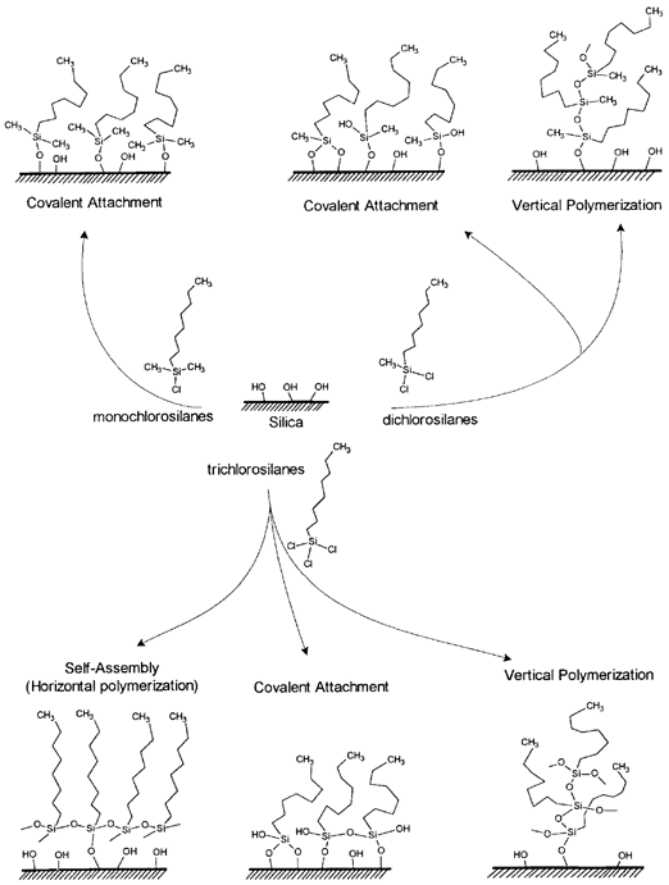

Figure 1.1 Possible products of the reaction of alkylchlorosilanes with silicon dioxide surfaces. [67]

The high surface to volume ratios of the nanoparticles makes them valuable in diverse research fields where surface functionality, interfacial correlation, and an ability to change material properties are extremely important.

Chapter three of this thesis presents a series of surface studies based on ionic nanoparticles. These new materials are hybrid particles comprised of an inorganic core functionalized with a soft organic shell. Because of their hybrid nature, their physical properties can be manipulated by varying the chemical composition and structure of the core and canopy.

The first part of Chapter four focuses on lead salt quantum dot QD, Ionic liquids. The QD ionic liquids are solvent-free and exhibit excellent photostability. In the second part of Chapter 4, I discuss a general one-step deposition process to produce super hydrophilic coatings using charged nanoparticles.

Finally Chapter 5 presents a series of PDMS-polyurea segmented copolymers and nanocomposites and discusses their fouling release behavior. The approach is scalable and large scale coatings can be produced readily.

REFERENCES

1. Bourlinos, A. B.; Herrera, R.; Archer, L. A.; Giannelis, E. P.; *Advance Materials*, ***2005***, 17, 234-237
2. Bourlinos, A. B.; Stassinopoulos, A.; Giannelis, E. P.; *Small*, ***2006***, 2, 513-516
3. Bourlinos, A. B.; Georgakilas, V.; Giannelis, E. P.; *Small*, ***2006***, 2, 1188-1191
4. Bourlinos, A. B.; Chowdhury, S. R.; Archer, L. A.; Giannelis, E. P.; *Small*, ***2005***, 1, 80-82
5. Bourlinos, A. B.; Chowdhury, S. R.; Archer, L. A.; Giannelis, E. P.; *Adv. Funct. Mater.*, ***2005***, 15, 1285-1290
6. Bourlinos, A. B.; Raman, K.; Archer, L. A.; Giannelis, E. P.; *J. Am. Chem. Soc*., ***2004***, 126, 15358-15359
7. Ogden. A. L.; Lewis, J. A.; *Langmuir*, ***1996***, 12, 3413-3424
8. Chan. A. T.; Lewis, J. A.; *Langmuir*, ***2005***, 21, 8576-8579
9. Plunkett. K. N.; Mohraz. A.; Lewis, J. A.; Moore, J. S.; *J. Am. Chem. Soc*., ***2005***, 127, 15574-14575
10. Tohver, V.; Chan, A. T.; Sakurada, O.; Lewis, J. A.; *Langmuir*, ***2001***, 17, 8414-8421
11. Tohver, V.; Smay, J. E.; Lewis, J. A.; *Proceedings of the National Academy of Science*, ***2001***, 98, 8950-8954
12. Gilchrist, J. F.; Chan. A. T.; Lewis, J. A.; *Langmuir*, ***2005***, 21, 11040-11047
13. Rhodes, S. K.; Lewis, J. A.; *J. Am. Ceram. Soc.*, ***2006***, 89, 1840-1846
14. Braem, A. D.; Biggs, S.; Prieve, D. C.; Tilton, R. D.; *Langmuir*, ***2003***, 19, 2736-2744
15. Braem, A. D.; Prieve, D. C.; Tilton, R. D.; *Langmuir*, ***2001***, 17, 883-890

16. Berglund, K. D.; Timko, A. E.; Przybycien, T. M.; Tilton, R. D.; *Progr. Colloid Polym. Sci.*, ***2003***, 122, 56-66

17. Kumar, N.; Varanasi, K.; Tilton, R. D.; Garoff, S.; *Langmuir*, ***2003***, 19, 5366-5373

18. Saleh, N.; Sarbu, T.; Sirk, K.; Tilton, R. D.; *Langmuir*, ***2005***, 21, 9873-9878

19. Liu, Y.; Majetich, S. A.; Tilton, R. D.; Sholl, D. S.; Lowry, G. V.; *Environ. Sci. Technol.*, ***2005***, 39, 1338-1345

20. Li, C.; Han, J.; Ryu, C. Y.; Benicewicz, B. C.; *Macromolecules,* ***2006***, 39, 3175-3183

21. Li, C.; Benicewicz, B. C.; *Macromolecules,* ***2005***, 38, 5929-5936

22. Li, Y.; Benicewicz, B. C.; *Macromolecules,* ***2008***, 41, 7986-7992

23. Schadler, L, S.; Kumar, S. K.; Benicewicz, B, C.; Lewis S. L.; Harton, S. E.; *MRS BULLETIN,* ***2007***, 32, 335-340

24. Dell'Acqua-Bellavitis, L. M.; Siegel, R. W.; *Langmuir,* ***2008***, 24, 957-964

25. Ash, B. J.; Siegel, R. W.; Schadler, L. S.; *Macromolecules,* ***2004***, 37, 1358-1369

26. Jiang, K.; Eitan, A.; Siegel, R. W.; Terrones M.; *Nano Letters,* ***2003***, 3, 275-277

27. Ajayan, P. M.; Nugent, J, M.; Siegel, R. W.; Wei, B.; Kohler-Redlich. Ph.; *Nature,* ***2000***, 404, 243

28. Glogowski, E.; Tangirala, R.; Emrick, T.; *Nano Letters,* ***2007***, 7, 389-393

29. Rathnayake, H. P.; Emrick, T.; *Macromolecules,* ***2008***, 41, 2969-2971

30. Sudeep, P. K.; Emrick, T.; *Polymer Reviews,* ***2007***, 47, 155-163

31. Glogowski, E.; Tangirala, R.; Russell, T. P.; Emrick, T.; *Journal of Polymer Science: Part A: Polymer Chemistry,* ***2006***, 44, 5076-5086

32. Glogowski, E.; He. Jinbo.; Russell, T. P.; Emrick, T.; *Chem. Commun.,* ***2005***, 4050-4052

33. Boker, A.; Lin, Y.; Emrick, T.; Russell, T. P.; *Nature Materials,* ***2004***, 3, 302-306

34. Caruso, F.; Caruso, R. A.; Mohwald, H.; *Science,* ***1998***, 282, 1111-1114

35. Caruso, F.; *Adv. Mater.,* ***2001***, 13, 11-22

36. Yap, H. P.; Quinn, J. F.; Caruso, F.; *Langmuir*, ***2005***, 21, 4328-4333

37. Katagiri, K.; Caruso, F.; *Macromolecules*, ***2004***, 37, 9947-9953

38. Park. M. K.; Onishi. K.; Lockin, J.; Caruso, F.; Advincula, R. C.; *Langmuir*, ***2003***, 19, 8550-8554

39. Laing, Z.; Susha, A.; Caruso, F.; *Chem. Mater.*, ***2003***; 15, 3176-3183

40. Caruso, F.; Caruso, R. A.; Mohwald, H.; *Chem. Mater.*, ***1999***, 11, 3309-3314

41. Mayya. K. S.; Schoeler, B.; Caruso, F.; *Adv. Funct. Mater.*, ***2003***, 13, 183-188

42. Caruso, F.; Mohwald, H.; *Langmuir*, ***1999***, 15, 8276-8281

43. Kumaraswamy, G.; Dibaj, A. M.; Caruso, F.; *Langmuir*, ***2002***, 18, 4150-4154

44. Caruso, F.; Spasova, M.; Susha, A.; Caruso, R. A.; *Chem. Mater.*, **2001**, 13, 109-116

45. Caruso, F.; Susha, A.; Giersig, M.; Mohwald, H.; *Adv. Mater.*, ***1999***, 11, 950-953

46. Caruso, F.; *Chem. Eur. J.,* ***2000***, 6, 413-419

47. Caruso, F.; *Aust. J. Chem.,* ***2001***, 54, 349-353

48. Susha, A. S.; Caruso, F.; Mohwald, H.; Giersig, M.; Eychmuller, A. Weller, H.; *Colloids and Surfaces A: Physicochemical and Engineering Aspects,* ***2000***, 163, 39-44

49. Caruso, F.; Giersig, M.; Mohwald, H.; *J. Am. Chem. Soc.,* ***1998***, 120, 8523-8524

50. Decher, G.; *Science,* ***1997***, 277, 1232-1237

51. Schneider, G.; Decher, G.; *Nano Letters,* ***2004***, 4, 1833-1839

52. Schneider, G.; Decher, G.; Nerambourg , N.; Praho, R.; Werts, M. H.; Blanchard-Desce, M.; *Nano Letters,* ***2006***, 6, 530-536

53. Lvov, Y.; Hass, H.; Decher, G.; Moehwald, H.; Kalachev, A.; *J. Phys. Chem.,* ***1993***, 97, 12835-12841

54. Schneider, G.; Decher, G.; *Langmuir,* ***2008***, 24, 1778-1789

55. Hudson J. B.; *Surface Science*, 1

56. Gao, L.; McCarthy, T. J.; *Langmuir, **2006***, 22, 6234-6237

57. Gao, L.; McCarthy, T. J.; *Langmuir, **2007***, 23, 9125-9127

58. Gao, L.; McCarthy, T. J.; *Langmuir, **2008***, 24, 9183-9188

59. Gao, L.; McCarthy, T. J.; *Langmuir, **2006***, 22, 2966-2967

60. Takeshita, N.; Paradis, L. A.; McCarthy, T. J.; Chen, Wei.; *Langmuir, **2004***, 20, 8131-8136

61. Gao, L.; McCarthy, T. J.; *Langmuir, **2006***, 22, 5998-6000

62. Wier, K. A.; McCarthy, T. J.; *Langmuir, **2006***, 22, 2433-2436

63. Ner, D.; McCarthy, T. J.; *Langmuir, **2000***, 16, 7777-7782

64. Chen. W.; Fadeev, A. Y.; Youngblood, J.; McCarthy, T. J.; *Langmuir, **1999***, 15, 3395-3399

65. Stafford, C. M.; Fadeev, A. Y.; Russell, T. P.; McCarthy, T. J.; *Langmuir, **2001***, 17, 6547-6552

66. Fadeev, A. Y.; McCarthy, T. J.; *Langmuir, **1999***, 15, 3759-3766

67. Fadeev, A. Y.; McCarthy, T. J.; *Langmuir, **2000***, 16, 7268-7274

68. Alonso, M. H.; McCarthy, T. J.; Jia, X.; *Langmuir, **2006***, 22, 1646-1651

69. Alonso, M. H.; McCarthy, T. J.; Jia, X.; *Langmuir, **2004***, 20, 9184-9189

70. Fadeev, A. Y.; McCarthy, T. J.; *Langmuir, **1998***, 14, 5586-5593

71. Lee, J. A.; McCarthy, T. J.; *Macromolecules, **2007***, 40, 3965-3969

72. Sethi, S.; Ge, L.; Ci, L.; Ajayan, P. M.; Dhinojwala, A.; *Nano Letters, **2008***, 8, 822-825

73. Niewiarowskil, P. H.; Lopez, S.; Ge, L.; Hagan, E.; Dhinojwala, A.; *PLoS ONE, **2008***, 3(5), 1-7

74. Li, G.; Prasad, S.; Dhinojwala, A.; *Langmuir, **2007***, 23, 9929-9932

75. Yurdumakan, B.; Harp, G. P.; Dhinojwala, A.; *Langmuir, **2005***, 21, 10316-10319

CHAPTER 2

SYNTHESIS AND CHARACTERIZATION OF IONIC NANOPARTICLES

2.1 Introduction

Generally, the preparation of the nanoparticles is carried out in the presence of stabilizing agents, which either chemically or physically bind with the surface atoms of the nanoparticles. The main functionality of the capping agents is to stabilize and prevent uncontrolled growth and aggregation of the nanoparticles. The optimal coupling ratio can be determined by means of a flocculation assay [1-3].

In the case of nanoparticles that are stabilized by anionic ligands such as citrate acid, the biomolecules couple through non-covalent electrostatic interactions. Silver nanoparticles, for example, are produced by the citrate method and have been functionalized at high pH values (above the isoelectric point), which allows an effective binding between the cation (amino acid side chains of the protein) and the anion (citrate groups of the colloids). The addition of electrolytes to silver nanoparticles causes flocculation and provides the repulsive layer that can stabilize nanoparticles.

However, in contrast to dispersed nanoparticles, colloid aggregation [2-4] is also widely used in many industrial processes. For example, some polymers and particle assemblies are successfully utilized in waste water treatment and mineral recovery. In fact, colloid instability can also be induced by surface modifications, depending on the nature and the concentration of the destabilizing agent. Neutralization of surface charges could be a major factor in the destabilization of

colloids. The possible charge screening demonstrates that charge plays an essential role.

Thus, optimization of the surface modification of particles is of extreme importance. In this thesis we focus on new synthesis, characterization, and processing for developing novel, stable and functional core/corona/canopy type nanomaterials.

2.2 Synthesis of Ionic Nanoparticles

The first generation of liquid-like ionic nanoparticles was prepared by following the procedure described by Bourlinos et al. (Fig. 2.1) [5-8]: 3.5 ml of silica colloid (Ludox-SM, 30 wt%, mean particle diameter: 7nm, surface area 350m^2/g) was diluted with 20 ml deionized water followed by the addition of a solution of 5 ml of $(CH_3O)_3Si(CH_2)_3N^+$-$(CH_3)(C_{10}H_{21})_2Cl^-$ in methanol (40%, Gelest). The white precipitate that formed immediately was aged for 24 h at room temperature, after which the solvent was discarded and the solid was rinsed three times with water and twice with ethanol. The solid was resuspended in ethanol, poured into a dish and dried at 70^{o}C. The corresponding sulfonate nanosalt was prepared by treating 1 g of the chloride analog with 15 ml of an aqueous (11%) solution of Poly(ethylene glycol) 4-nonylphenyl 3-sulfopropyl ether potassium salt, $(R(CH_2CH_2)_7O(CH_2)_3SO_3^-K^+$, Aldrich) in water at 70^{o}C for 24 h, after which the solvent was discarded and the material was washed several times with water and dried at 70^{o}C. The volume fraction of the silica nanoparticle is approximately 13%.

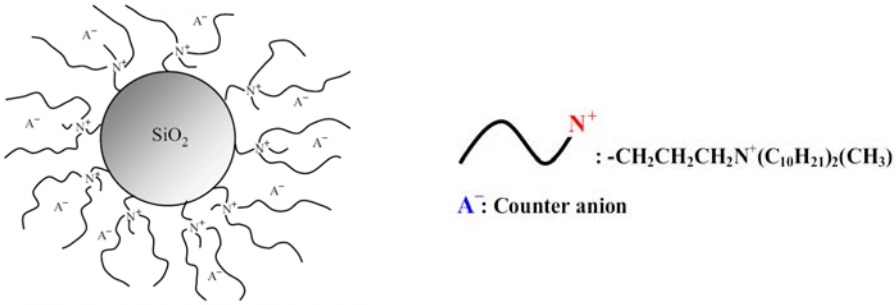

Figure 2.1 Nanoparticle salt based on surface-functionalized silica nanoparticles. [6]

The second generation of liquid-like ionic nanoparticles began with the work of Dr. R. Hererra and R. Rodriguez, who switched the core-shell main mechanism from ionic exchange to acid-base neutralization (Scheme 2.1) [9]. In one flask, Ludox HS-30 (diameter=7nm, Sigma Aldrich) colloidal silica (3 g) was diluted with deionized water (22 mL). At the same time 3-(trihydroxysilyl)-1-propane sulfonic acid (SIT, 40 wt %, Gelest) (4 g) was diluted with deionized water (20 mL). The silica suspension was slowly added to the SIT suspension while being stirred vigorously. To this mixture, a solution of sodium hydroxide (1 M) was added dropwise until the reaction pH was about 5. The entire solution was then heated to 70^{o}C and stirred vigorously for 24 h. Next, the suspension was placed into SnakeSkin dialysis tubing (10k MWCO, Pierce) and dialyzed using deionized water for 48 h. After dialysis, the functionalized silica solution was run through an ion exchange column (Dowex, HCR-W2 ion exchange resin) to remove Na^{+} ions and fully protonate the sulfonate groups present. NIMs were prepared by dissolving the desired amount of Ethomeen 18/25 ($(C_{18}H_{37})N[(CH_2CH_2O)_mH]$-$[(CH_2CH_2O)_nH]$, Azko-Nobel) in deionized water to a concentration of 10 wt%. The Ethomeen 18/25 solution was then added dropwise to the silica solution while the pH was monitored. Once the silica and amine were reacted, the solvent was slowly removed by placing the solution in a vacuum oven and drying

at 35°C until all the water was evaporated. Equivalence point plots were used to determine the 1:1 ratio of nanoparticle cores/counter ion and synthesize stoichiometric NIMs, as well as NIMs with varying nanoparticle core content below and above the equivalence point.

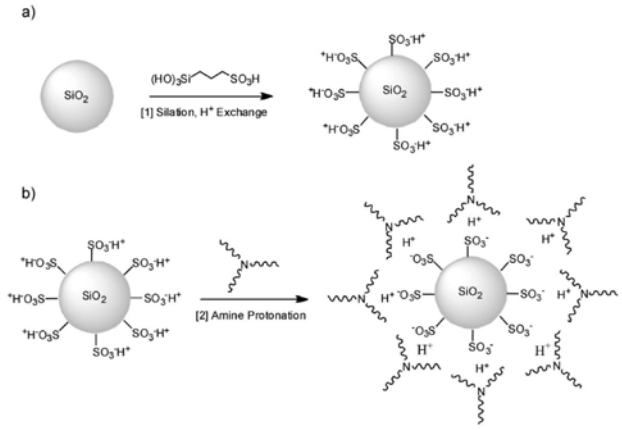

Scheme 2.1 Standard synthesis of NIMs. a) Surface-functionalized by condensation with a sulfonate organosilane (corona). b) The acidic particles are neutralized with the tertiary amine (canopy). [9]

2.2.1 Synthesis of Cationically-charged Silica-based Nanoparticles

Two general approaches were used to synthesize cationically-charged SiO_2 nanoparticles. The first procedure is a typical two-step process in aqueous solution (Scheme 2.2) [10]. The hydrolysis and condensation of organosilanes were performed via the successive addition of HCl and NaOH as catalysts. 3 grams of colloidal silica (HS-30) was diluted with deionized water (30 mL) and sonicated for 30 min. A concentrated solution of HCl (1.0 N) was added to the dispersion followed by the addition of 3.2 g of N-Trimethoxysilylpropyl-N,N,N-trimethylammonium chloride (50 wt %, Gelest). The mixture was stirred at 60 °C for 10 min. NaOH (0.1 M) was added to adjust the pH to ~5 and the mixture was stirred continuously at 60 °C for 24 h to

complete the reaction. Subsequently, the suspension was dialyzed in deionized water using SnakeSkin tubing (3.5k MWCO, Pierce) for 48 h.

The second procedure is a typical one-step process in ethanol solution. 1 gram of M-5 sub-micro silica (Cab-O-Sil M-5 fumed silica) was dispersed in deionized water (30 mL) and then sonicated for 30 min. The suspension was ran through an ion exchange column to remove Na^+ ions and fully protonate the surface groups. The solution was then discarded and the solids were washed wish water. The remaining silica was re-dispersed into ethanol. Organosilane silane (3 g) was added to the silica dispersion and the mixture was stirred at 60^{o}C for 24 h to allow condensation to take place. After that, the suspension was placed into SnakeSkin dialysis tubing (3.5k MWCO, Pierce) and dialyzed using deionized water for 48 h.

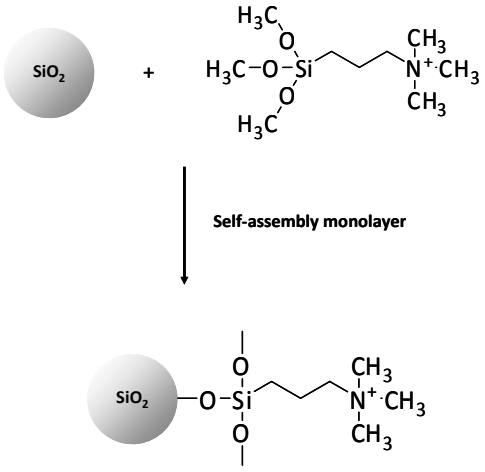

Scheme 2.2 Synthesis of silica-based ionic nanoparticles

2.2.2 Carbon black-based Ionic Nanoparticles

Ionic nanoparticles based on carbon black were also synthesized for this study. Carbon black was obtained from Cabot and used as received. Two types of carbon black particles were selected as precursors—carboxyl-terminated (CBf) and sulfonate-terminated (CBg) (Scheme 2.3) (diameter = 50-100nm, CABOT)—based on their dispersibility, polarity, reactivity, and surface charges. Scheme 2.4 shows the detailed procedure, which is similar to that of silica modification. The reaction of acid in the form of the carboxyl/sulfonate functionalized carbon black nanoparticles with an amine transforms the powders to black molten salts. The salt's fluidity can be adjusted by controlling the volume fraction of cores. Because carbon black particles tend to aggregate more than silica, a low concentration is necessary to maintain a good dispersion and prevent particle aggregation.

In one flask, modified carbon black powder CBg (5 g) was diluted with de-ionized water (500 ml). The solution was placed into an ultrasonic bath for 30 min. After reaching ideal dispersion (verified by light scattering), the functionalized carbon black solution was run through an ion exchange column to remove Na^+ ions and to fully protonate the sulfonate groups present.

Carbon black-based ionic nanoparticles were prepared by dissolving the appropriate amount of polyetheramines ($CH_3(CH_2CH_2O)_x(CH_2CHCH_3O)_yNH_2$, Jeffamine XTJ-505/M2070, Huntsman) in de-ionized water. The polyetheramines solution was then added dropwise to the carbon black solution while the pH was monitored. Once the sulfonic acid and amine were reacted, the solvent was slowly removed by placing the solution in a vacuum oven to dry at 35 °C until all the water evaporated. NIMs with varying carbon black core content (5wt.%-60 wt.%.) were synthesized.

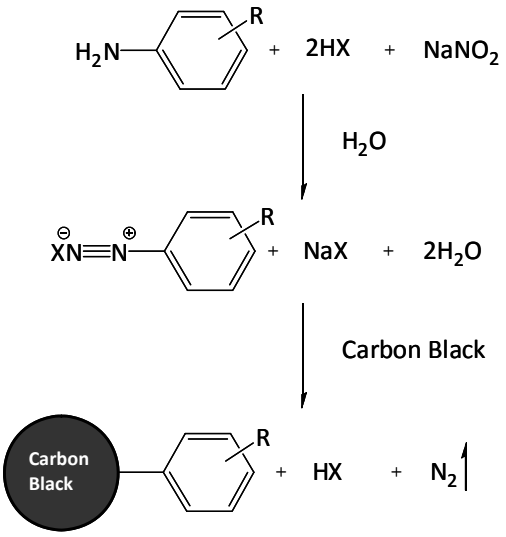

Scheme 2.3 Schematic of carbon-black functionalization: (1) Primary aromatic amine with nitrous acid, (2) Highly reactive arene diazoniun salt, (3) Nucleophile replacement.

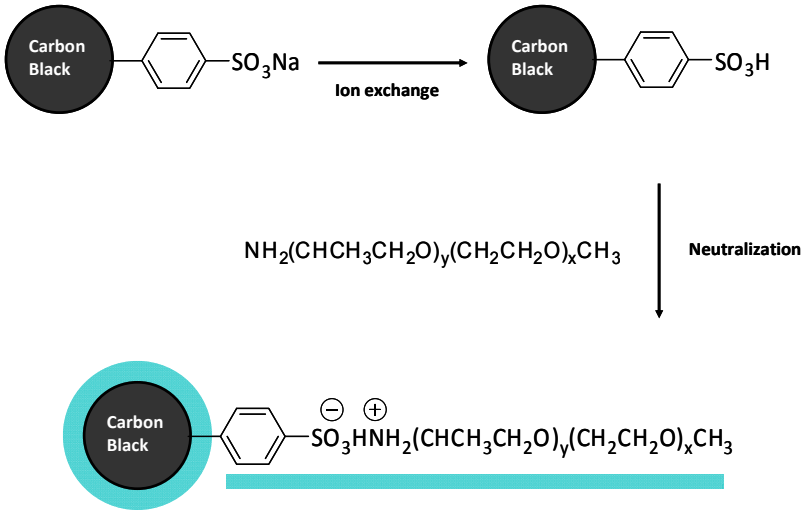

Scheme 2.4 Carbon black-based NIMs synthesis. a) Protonated through ionic exchange (corona), b) Neutralized with the polyetheramines (canopy).

2.2.3 Gold-based Ionic Nanoparticles

Gold colloids were synthesized by $NaBH_4$ reduction (Scheme 2.5) [11]. 0.26g (1.4mmole) of sodium 3-mercapto-1-propanesulfonate was dissolved in 10ml methanol and placed into an ice bath. 10 ml methanol mixed with 0.6g gold(III) chloride solution (HAuCl4•HCl, 99.99%, 30 wt. % in dilute HCl, Sigma-Aldrich) was added dropwise into the previous solution with gentle stirring. 2.5ml of acetic acid was added to avoid deprotonation. The last step was to add 0.17g of sodium borohydride (NaBH4, >96%, Sigma-Aldrich), which is a stronger reducing agent, with 5ml H_2O to reduce the gold under an ice bath. The solution color gradually changed from yellow to light gray and a precipate was formed. The reaction took place over a period of 24 hours at room temperature. Then the ionic particles were purified through centrifugation and washing using a mixed solvent system (methanol : water = 4 : 1).

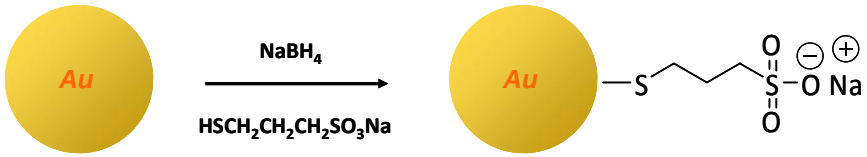

Scheme 2.5 Synthesis of gold-based ionic nanoparticles

2.2.4 Quantum Dots-based Ionic Nanoparticles

Synthesis of colloidal PbS QDs

Lead(II) oxide (220 mg, 1 mmol, 99.999%), oleic acid (0.64 mL, 2 mmol, 90%), and 1-octadecene (ODE, 9.36 mL, 90%) were mixed and stirred at 150^{o}C in a pure nitrogen environment. At the same time, a 0.1M hexamethyldisilathiane ($(TMS)_2S$, 126 mL, 0.6mmol) in ODE (6 mL) was stirred in a glove box for at least 30 minutes. After the reaction solution (containing PbO) turned clear, the temperature was set to 90^{o}C and allowed to stabilize. Then 5 mL of the $(TMS)_2S$ /ODE solution (0.5 mmol sulfur) was drawn into a syringe and injected into the reaction solution. After reacting for 1 minute, the reaction solution was rapidly cooled in an ice bath. The growth solution was then mixed with 5 mL hexane. Excess oleic acid and unreacted precursors were removed by precipitating the particles using incompatible solvents, e.g. methanol. The nanocrystals were then re-dispersed in toluene and stored in a light-deprived environment.

Synthesis of ionic liquid ligands

Sodium 3-mercapto-1-propanesulfonate (0.2g, 1.12mmol, technical grade, 90%) was dissolved in 4ml de-ionized water. The solution was run through an ion-exchange column (Dowex, HCR-W2 ion-exchange resin) to remove Na+ ions and fully protonate the sulfonate groups present. The fully protonated solution showed a distinct pH value change (from 2.75 to 0). Polyetheramine (0.67g, 1.12mmol, Jeffamine XTJ505) was prepared with 3 ml de-ionized water and then was added dropwise to the sulfuric solution while the pH was monitored. Once the equilibrium point was reached, the reaction mixture was kept shaking at room temperature overnight. The next step was to remove the solvent by leaving the solution in a vacuum oven drying at 35 °C, until all the solvent was removed. Equivalence point

plots were used to determine the 1:1 ratio of counter ions. The final liquid-like, solvent-free materials were then purified by centrifugation (Scheme 2.6).

Synthesis of PbS QD ionic liquids

Polar condition: As-synthesized PbS QDs (0.5 mL) in toluene solution (concentration about 10 mg/mL) was added to a 0.5 mL of ionic liquid (XTJ505-based IL) in a centrifuge tube. The molar ratio of PbS QDs to ionic liquid ligands was about 1:10000. The excess ligands prevented QDs from aggregating. Initially, the ionic liquid and QD toluene solution were phase-separated, showing a layer of brown QD toluene solution on the top and a layer of transparent ionic liquid on the bottom. The QDs in the toluene slowly diffused into the ionic liquid phase and, finally, the whole solution turned uniformly brown. The solution was then centrifuged at a speed of 14500 rpm for 5 minutes. No precipitation was observed. The mixed solution was then loaded into a vacuum oven and dried at 40^{o}C until all of the toluene solvent was removed. The final volume of the solution was about 0.5 mL. (Scheme 2.7)

Apolar condition: As-synthesized PbS QDs (0.4 mL) in toluene solution (concentration about 2 mg/mL) were added to 0.4 mL (concentration about 16.7%) of the ionic liquid aqueous solution (XTJ506 based, more hydrophilic) in a centrifuge tube. Initially, the ionic liquid aqueous and QD toluene solution were phase-separated, showing a layer of brown QD toluene solution on the top and a layer of transparent ionic liquid in water on the bottom. After 20 hours of steady shaking, the QDs (brown) in the toluene slowly extracted into the ionic liquid aqueous phase. The original stabilizer oleic acid was expected to stay in the toluene phase. The aqueous layer was collected and centrifuged at a speed of 14500 rpm for 5 minutes. No precipitation was observed. The solution was then loaded into a vacuum oven and dried at 40^{o}C until all

of the water was removed. The final volume of the solution was about 0.4 mL. (Fig. 2.2)

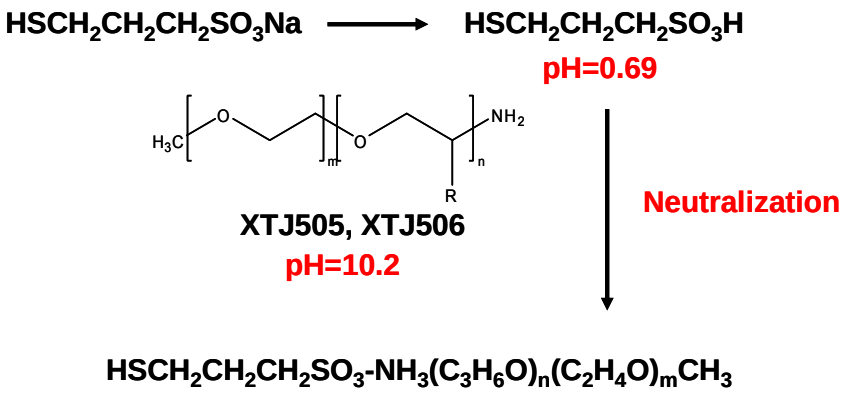

Scheme 2.6 Preparing ionic-liquid ligands

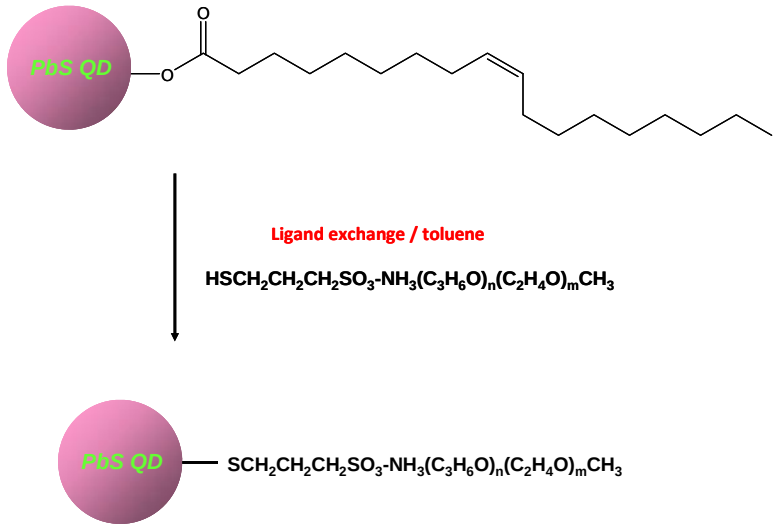

Scheme 2.7 One-step grafting-from technique for PbS QD-based ionic liquids

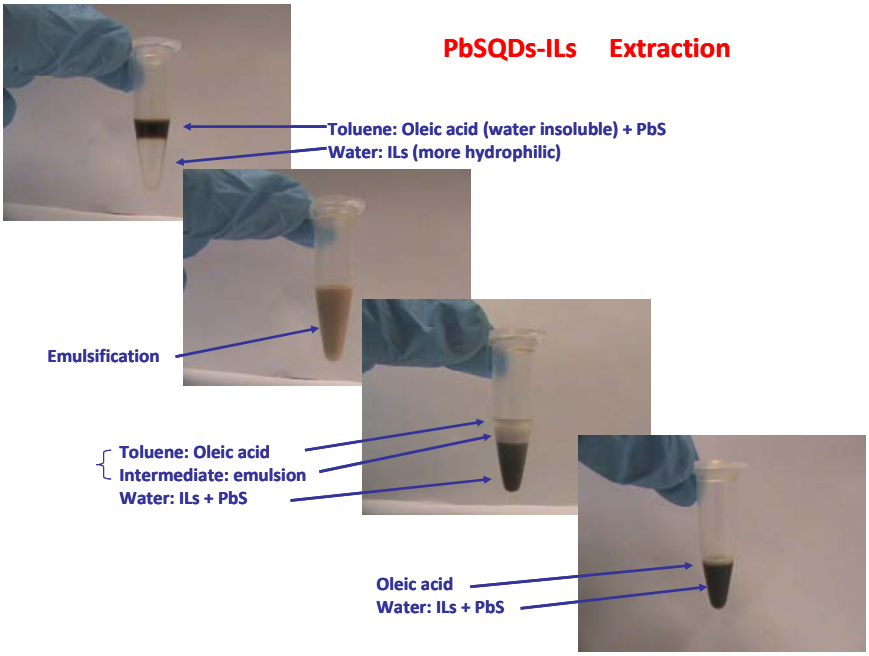

Figure 2.2 Extraction of PbSQD-based ionic liquids

2.3 FT-IR Characterization

Fourier transform infrared spectroscopy (FT-IR) is a reliable source for chemical characterization that can be used to characterize the level of completion of reactions, the possible formation of side products, and chemical compositions [3].

The starting silica nanoparticles should theoretically contain hydroxyl groups carried over from the precursor and bound to their surfaces. However, their intensities were not strong enough to be identified via FT-IR. The FT-IR spectrum of the silica nanosalt exhibits the broad absorption band characteristic of the surface modifier (silane3) (Fig. 2.3). The broad band 1099cm^{-1} also indicates the existence of covalent bonding, Si-O-Si, between the silica core and silane modifier. The disappearance of

the CH_3-O stretch at 2380cm^{-1} could be explained as a reaction of silane with the silica surface and as self-polymerization [12-14].

In the case of carbon black particles two different types were selected as precursors: carboxyl-terminated (CBf) and sulfonate-terminated (CBg). However, it is difficult to identify the surface functional ligands through FT-IR. Pure CBg (Fig. 2.4) doesn't show the signal of sulfonate ligands (ex: S=O, S-O). After neutralization and purification, the new nanosalt CBg-M2070 shows the signals that corresponded to the surface modifier M2070 (C-H stretching 2874cm^{-1}; C-H bending 1350, 1466 cm^{-1}; C-O-C stretching 1107cm^{-1}; C-H out-of-plane bending 947cm^{-1}) and the carbon black (peaks 1960~2156cm^{-1}).

Figure 2.5 shows the comparison between the surface functionalized gold nanosalts and the surface modifier (mercaptosulfonate). The ionic gold nanoparticles exhibit strong absorption band characteristic of the new surface functional groups after removing excess reagents. The signals of the new surface ligand include splits of the S=O asymmetric stretching in the region of 1150~1250cm^{-1}, a S=O symmetric stretching at 1051cm^{-1}, and a S-O stretching at 732cm^{-1}. This information indicates that the main functional groups grafted onto the surface of gold nanocrystals are sulfonate. However, the disappearance of the thiol ligand (S-H, 2548cm^{-1}) is not sufficiently clear proof of the formation of bonds between the gold and the surface modifier.

As seen in Figure 2.6, sodium 3-mercapto-1-propanesulfonate demonstrated a S-H stretching at 2548cm^{-1}, splits of S=O asymmetric stretching in the region of 1150~1250cm^{-1}, a S=O symmetric stretching at 1051cm^{-1}, and a S-O stretching at 732cm^{-1}. Another starting reagent, polyetheramine, showed splits of C-H stretching in the region of 2979~2868cm^{-1}, a pair of C-H bending at 1461,1378 cm^{-1}, a strong C-O-C stretching at 1101cm^{-1}, and a C-H out-of-plane and bending at 925cm^{-1}. This

information provides an important blueprint for surface functionalized PbS quantum dots.

The ionic liquid ligands also appeared with splits of C-H stretching in the region of 2979~2868cm^{-1}, a pair of C-H bending at 1461,1378 cm^{-1}, a strong C-O-C stretching at 1101cm^{-1} from polyetheramine; an S=O symmetric stretching at 1051cm^{-1}, an S-O stretching at 732cm^{-1} from mercapto-sulfuric, and the ionic liquid passivated PbS quantum dots. There was no signal indicating the presence of toluene or water, confirming that the product was a solvent-free material.

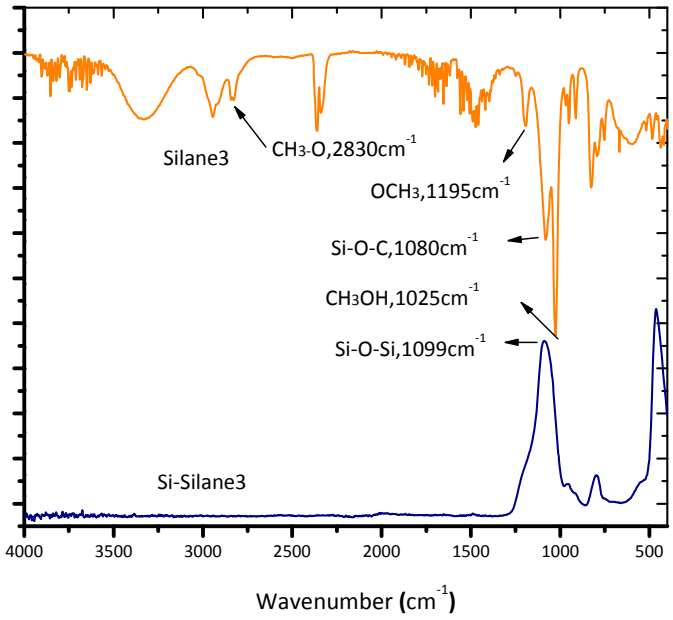

Figure 2.3 FT-IR spectrum of silica-based ionic nanoparticles

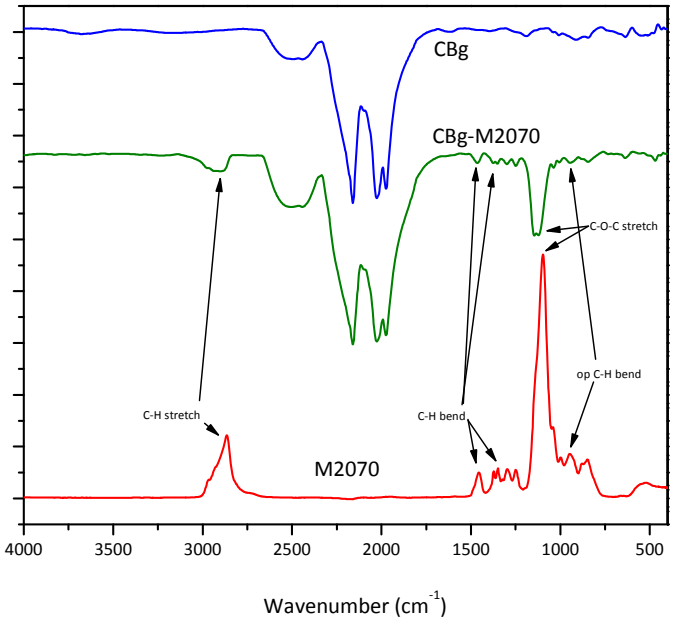

Figure 2.4 FT-IR spectrum of carbon black-based ionic nanoparticles

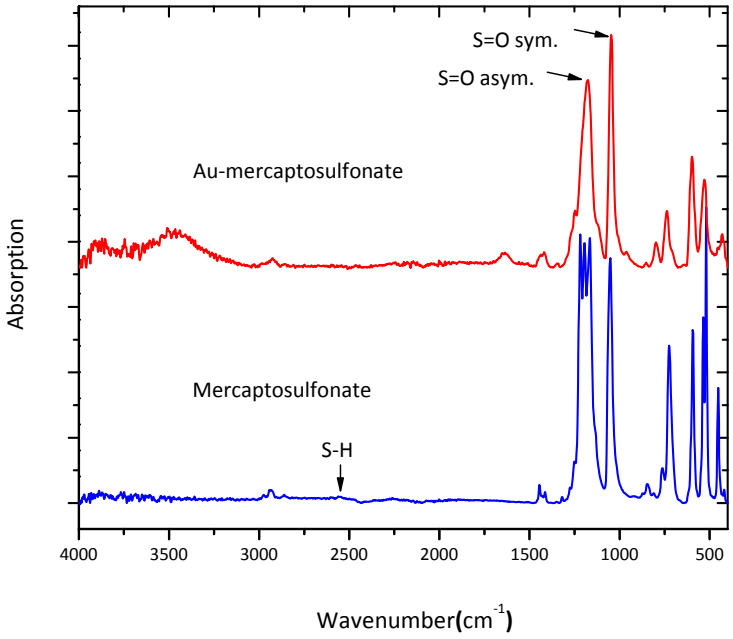

Figure 2.5 FT-IR spectrum of gold-based ionic nanoparticles

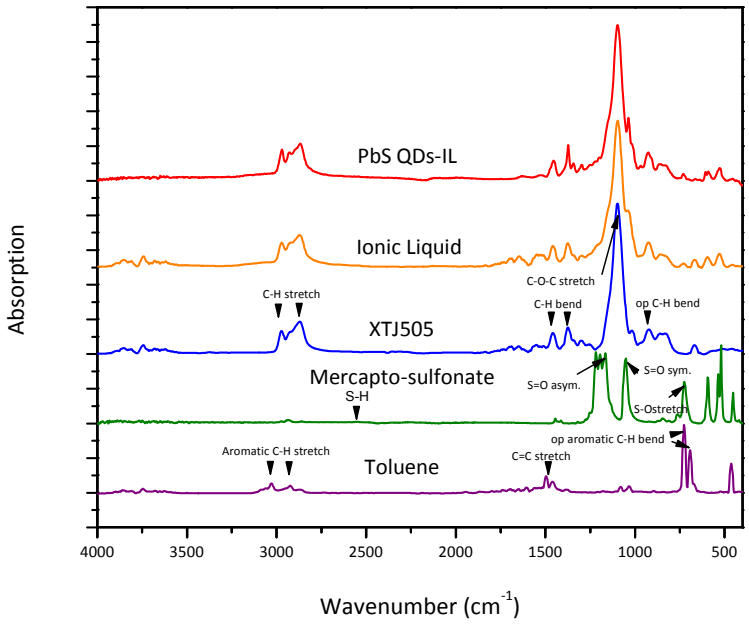

Figure 2.6 FT-IR spectrum of PbS quantum dot-based ionic nanoparticles

2.4 DLS Characterization

2.4.1 Size distribution

Dynamic Light Scattering (DLS) is the same as Photon Correlation Spectroscopy (PCS) and provides a way to characterize particles and molecules inside liquid medium. By using this technique, information can be collected about the particle size, zeta potential, and molecular weight. The theory is based on detecting the particles' Brownian motion by analyzing the intensity fluctuations in the scattered light and correlating them with the size of the particles. All of the measurements in this section were carried out using the Malvern Zetasizer Nano-ZS (Malvern Instruments, England) with an He-Ne laser at 633nm. Viscosities and refractive indices needed for the data analysis were taken from the literature. The measured data in a DLS plot is the correlation curve. When approximations are made that these

particles have spherical geometry at infinite dilution, the Stokes-Einstein relation [15] can be used to estimate the effective hydrodynamic diameter (DH).

The Stokes-Einstein equation for the hydrodynamic diameter is:

$$D_H = \frac{kT}{F} = \frac{kT}{3\pi\eta D}$$

D_H : Hydrodynamic diameter

k : Boltzmann constant

F : Particle frictional coefficient

η : Solvent viscosity

T : Absolute temperature

D : Diffusion coefficient

Purification is critical for DLS measurements, and the preparation of the sample solution has a strong impact on the results. All nanoparticle or polymer solutions (1~20mg/ml) were prepared by dilution of the stock solutions (spectro grade). Dust-free solutions for DLS were obtained more than 12 h before measurement by filtration through nylon membrane filters with a pore size of (0.2-0.45 μm) (GE Nylon ® Syringe Filter), directly into specific cuvettes that had been cleaned with acetone.

The unmodified nanosilica HS-30 showed a hydrodynamic diameter of about 9.7nm (Fig. 2.7a), which was close to that reported by the supplier (7~8 nm). The hydrodynamic diameter measured by DLS can sometimes be overestimated when the macromolecules or particles have imperfect geometry. The diameter calculated from the diffusion properties of the particles indicates the particles' mobile dimension, which was related to stationary particle size. Figure 2.7b shows the HS-SIT particle size (32.8 nm), which was surface-functionalized by condensation with a sulfonate organosilane. The increased diameter was due to the formation of a self-assembled

monolayer of silane onto the silica surface. A similar explanation would apply in the case of ionic nanosilica HS30-Silane3 (Fig. 2.7c); depending on the initial loading of the ammonium-terminated silane, the size of the charged nanosilica could be adjusted from 15.8 to 22.5 nm. According to the literature [10], the average diameter of silica particles modified with organo-silane is a function of the silica content at a fixed monomer concentration or a function of the silane loading at a fixed silica concentration. The final particle size increased as the initial organo-silane concentration increased, which was confirmed by the regular growth on the surface of the silica particles. Submicro silica-based ionic particles of M5-Silane3 (Fig. 2.7d) have a diameter (~280 nm). Those two scales of ionic particles could be utilized to study the impact of particle size, surface area, ionic strength and bonding density to material properties.

In carbon black-based ionic particle systems, both carboxyl (Fig. 2.7e) and sulfonate (Fig. 2.7f) functionalized carbon blacks have similar diameters (50-100 nm). Even after introducing the canopy, the dimensions of CBg-M2070 (Fig. 2.7g) are close to that of the seed particles (117 nm).

The gold-based ionic particles (Fig. 2.7h) also showed a diameter of 16.7nm. The sodium borohydride leads to seed particle (gold colloid) smaller than the citrate reduction did. Even after grafting sulfonate-terminated functional groups onto the gold surface, the whole gold ionic particle size is still smaller than the citrate reduction gold colloid (> 20nm) [16]. The dimensions of the colloidal PbS quantum dots (Fig. 2.7i) were 6.9nm without photobleach or aggregation.

2.4.2 Zeta potential distribution

In an ionic nanoparticle system, the free ions in solution distribute themselves between the relatively larger particles, according to the laws of electrostatics and

thermodynamics. The charged particle surface and the diffuse layer of the mostly oppositely charged ions surrounding it comprise the electrical "double layer" [17,18]. The way to estimate the stability of a colloidal-type nanoparticle is determined by the balance between the repulsive and attractive forces when the particles approach each other.

DLS estimates the zeta potential by determining the electrophoretic mobility and then applying the Henry equation, shown below. The magnitude of the zeta potential gives an indication of the stability and charge density, which strongly implies the degree of surface modification of the ionic nanoparticles. If particles in suspension have a large negative or positive zeta potential, they will tend to repel each other without a tendency to flocculate. However, if the particles have low zeta potential values, there is no force to prevent the particles from coming together and flocculating. Generally, particles with zeta potentials more positive than +30mV or more negative than -30mV are considered to be stable.

The Henry equation is:

$$U_E = \frac{2\varepsilon z f(ka)}{3\eta}$$

z : Zeta potential

U_E : Electrophoretic mobility

ε : Dielectric constant

η : Viscosity

f(ka) : Henry's function (using either 1.5 or 1.0 as an approximation)

The interesting part of ionic particles is their charge behavior, which results in mutual repulsion at extended distances. Ideally, the repulsive forces are sufficiently strong to prevent the particles from diffusing close to each other, where short-range Van der Waals attractive forces dominate and lead to aggregation.

From the zeta potential results (Fig. 2.8a,b,c), we show that the silica particles carry adequate net charge, either positive or negative. Even if the core materials are switched from silica to carbon black or gold nanocrystals, the high zeta potential (>37 mV) (Fig. 2.8d,e) confirmed their stability and implied the high completion of surface functionalization, both of which are important for assembly.

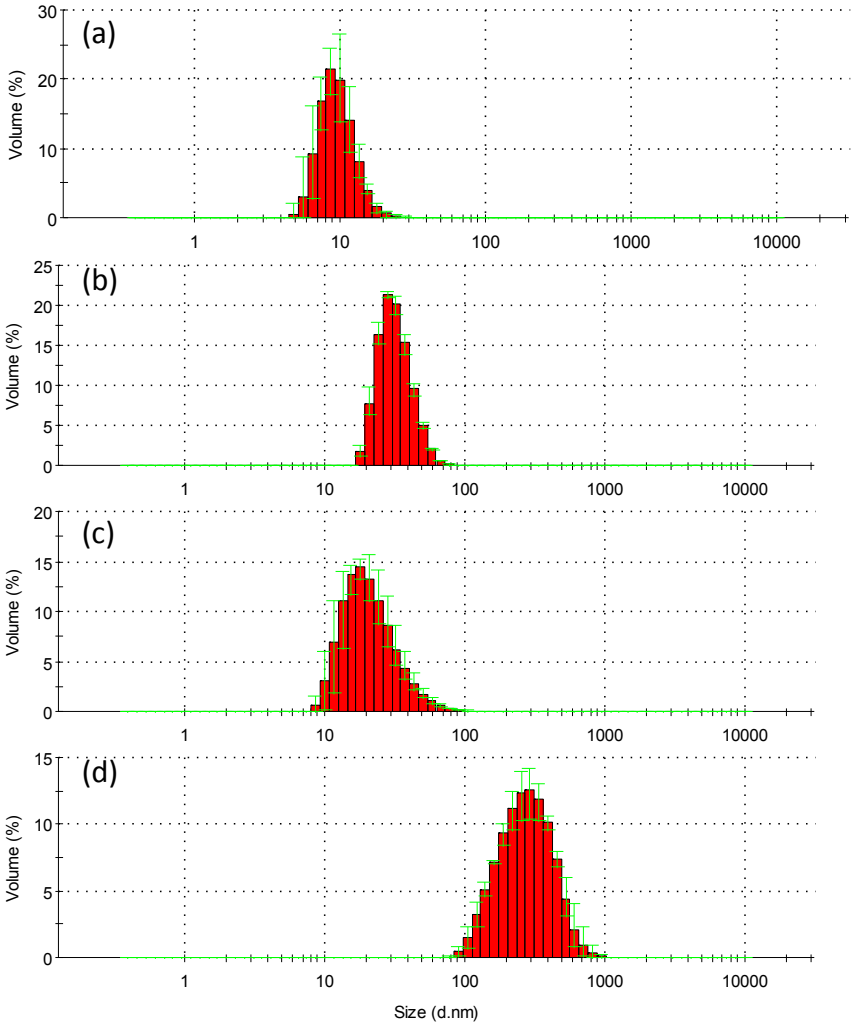

Figure 2.7 DLS particle size distribution by volume - statistics graph (a)HS30, (b)HS30-SIT, (c)HS30-Silane3, (d)M5-Silane3, (e)CBf, (f)CBg, (g)CBg-M2070, (h)Au-sulfonate, (i)PbSQDs/oleic acid (toluene)

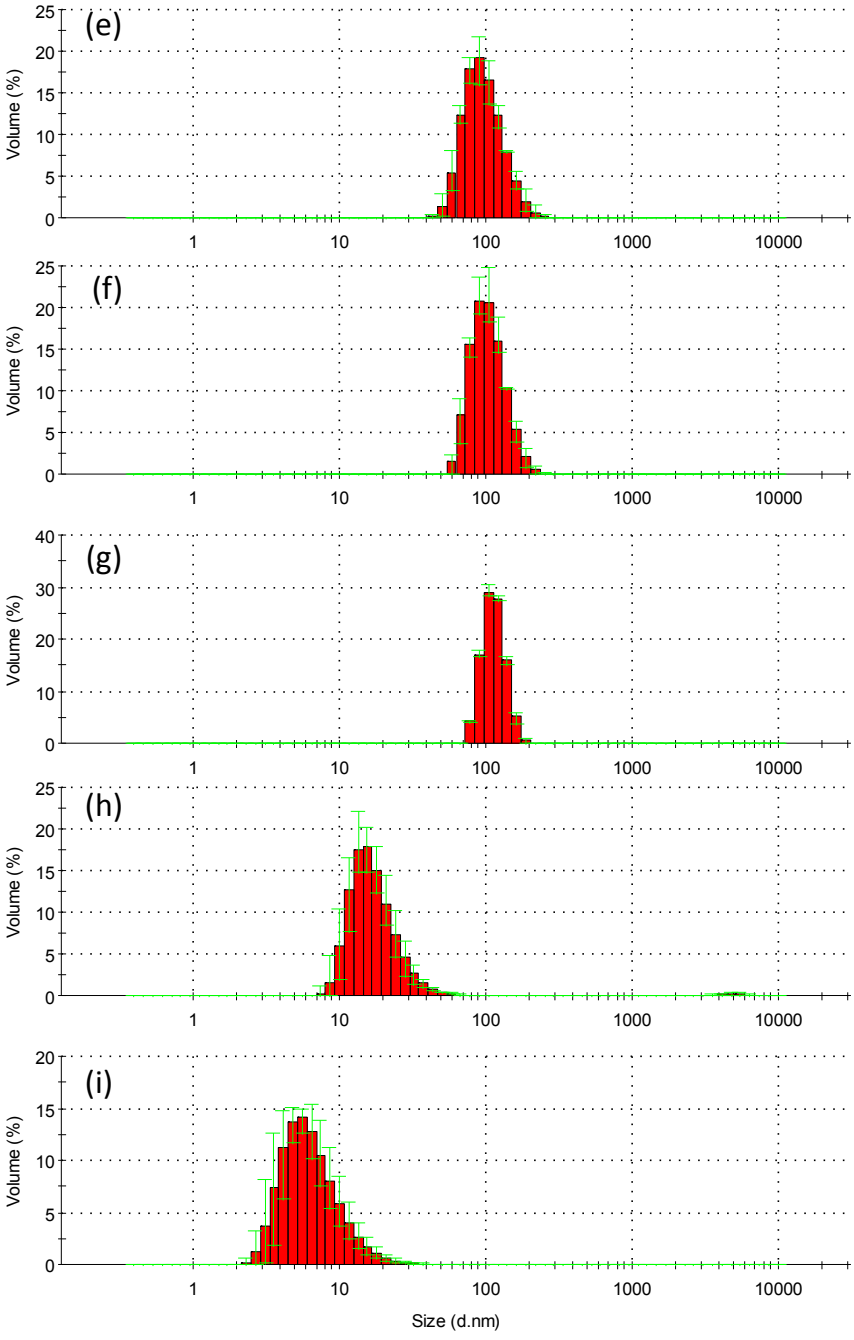

Figure 2.7 (continue) DLS particle size distribution by volume - statistics graph (a)HS30, (b)HS30-SIT, (c)HS30-Silane3, (d)M5-Silane3, (e)CBf, (f)CBg, (g)CBg-M2070, (h)Au-sulfonate, (i)PbSQDs/oleic acid (toluene)

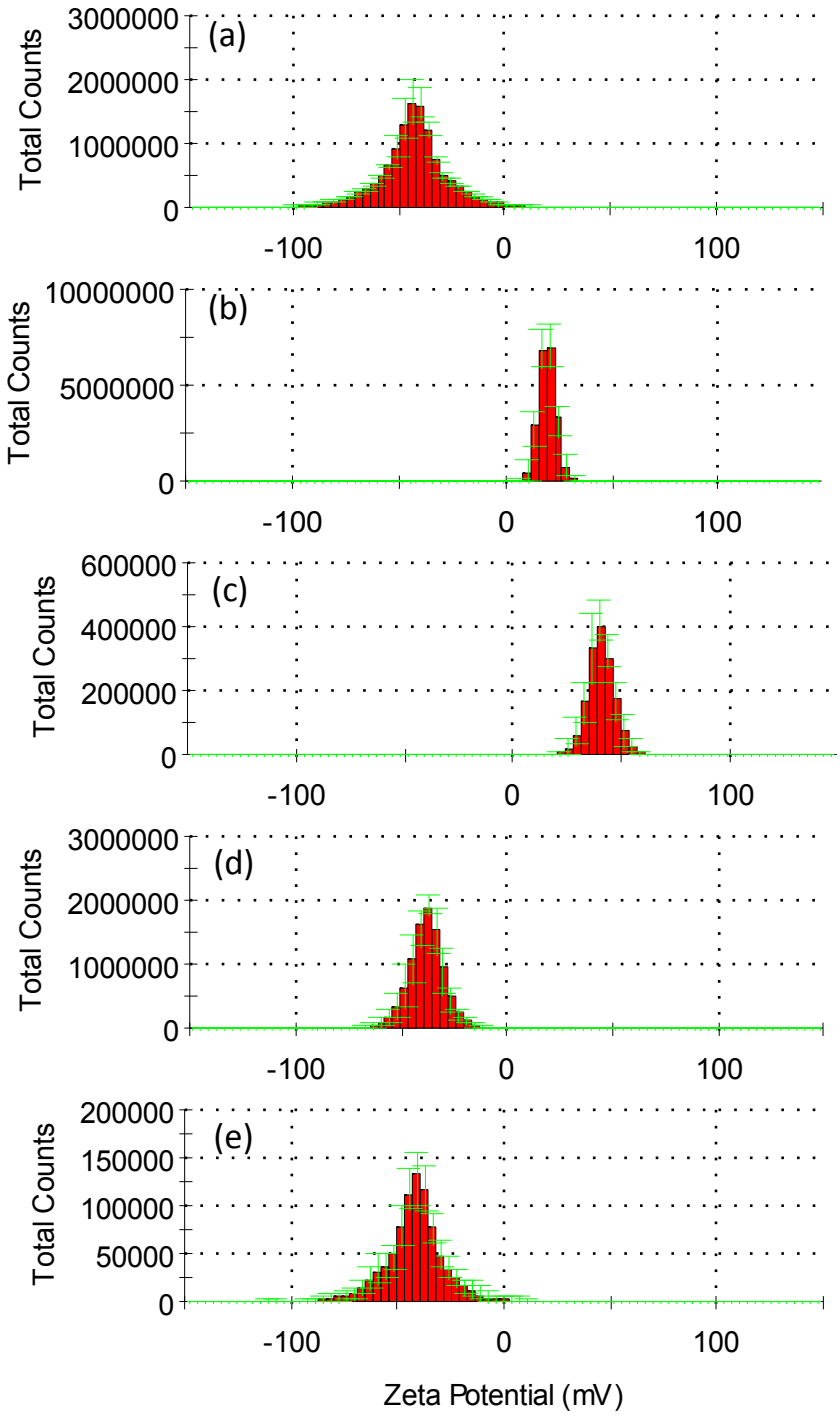

Figure 2.8 DLS particle zeta potential distribution - statistics graph (a)HS30-SIT, (b)HS30-Silane3, (c)M5-Silane3, (d)CBg, and (e)Au-sulfonate

2.5 DSC/TGA Characterization

2.5.1 Differential scanning calorimetry measurements

We used differential scanning calorimetry (DSC) as the standard technique for monitoring heat effects associated with phase transitions and chemical reactions of our nanomaterials.

DSC analysis of CBg-M2070 (Fig. 2.9) showed a second-order transition at -61^{o}C, corresponding to the glass transition (Tg), followed by a first-order endothermic transition at 7^{o}C, corresponding to the melting temperature (Tm), which supports the liquid behavior of the nanoparticles at room temperature. The canopy, Jeffamine M2070, exhibited similar second-order transition at -70^{o}C (Tg), and a first-order transition at 4^{o}C (Tm). The glass transition temperature of nanocomposite was higher than the pure polymer (canopy) (70 > 61^{o}C), and this shift is usually interpreted in terms of reduced mobility of the polymer chains because of their interaction with the core materials and an increase in the confinement [19].

The study of the polymer crystallinity by DSC has been broadly reviewed [20]. The melting temperature of the nanocomposite was slightly higher than that of the pure polymer (canopy) (7 > 4^{o}C). There is a change in the polymer crystallinity when the polymer chains graft onto the core and this enhances the possibility of physical cross-linking. On the other hand, when the number of excess or unbound polymers is higher than the number of confined polymers, the crystallinity in hybrids is the same as that of the pure polymer.

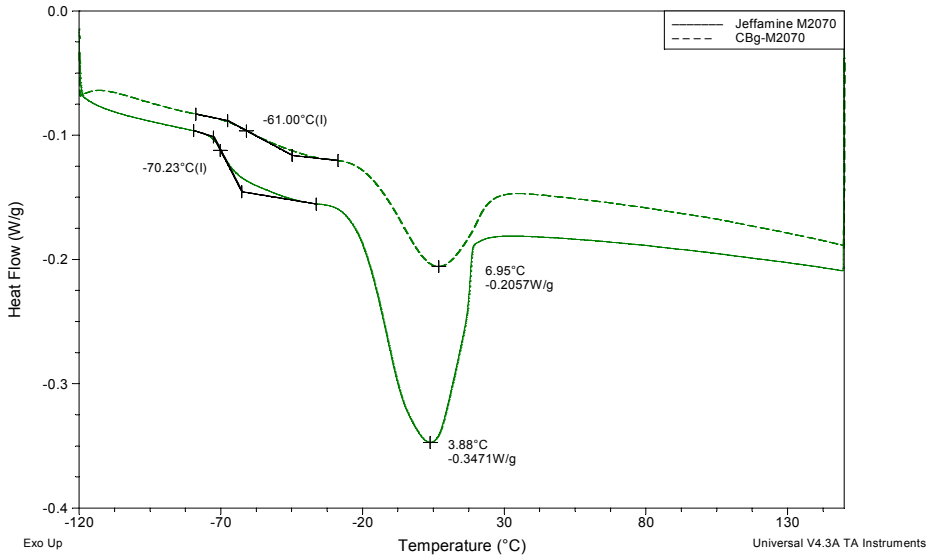

Figure 2.9 DSC measurements of Jeffamine M2070 and nanocomposite CBg-M2070

2.5.2 Thermal Gravimetric Analysis measurements

We used TGA to determine polymer degradation temperatures and the amount of volatiles in our systems. [21-23]

The TGA results showed that polyetheramine functionalized carbon black (CBg-M2070) is absolutely solvent-free (no significant weight loss before 150^{o}C) with a decomposition temperature >250^{o}C and a residue content of 53.3% w/w (Fig. 2.10a).

The initial weight loss of the CBg-M2070 occurred near 280^{o}C in nitrogen as a result of the decomposition of the canopy polymer. This temperature is much higher than most conventional solvent systems and shows a thermal stability that is promising for future applications.

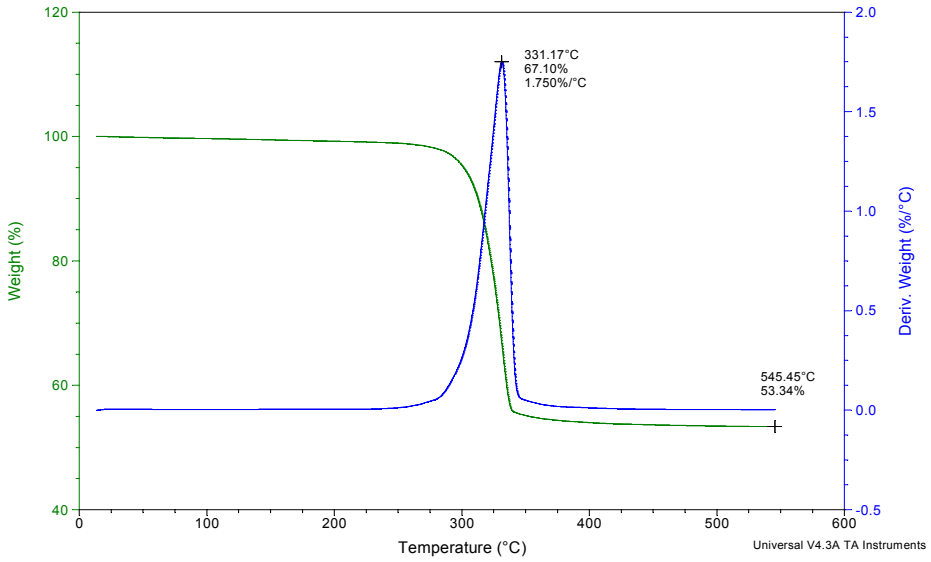

Figure 2.10(a) TGA measurement of carbon black-based ionic particles, CBg-M2070

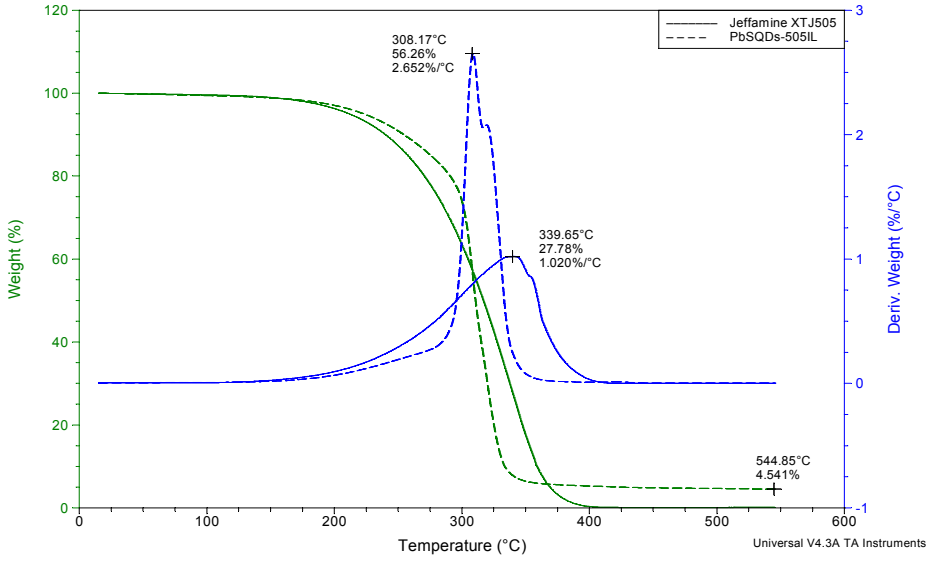

Figure 2.10(b) TGA measurements of Jeffamine and quantum dot-based ionic nanoparticles, PbSQDs-505IL.

Assuming uniform surface coverage, we can estimate an average of 4–5 functional ligands per square nanometer of carbon black surface. The weight loss above 300^{o}C is due to decomposition of the polymer (canopy). The polymer (canopy) and carbon black (core) content is 47 wt. % and 53 wt. %, respectively, corresponding to a composition that agrees well with the formula.

Another TGA result showed that polyetheramine-encapsulated lead sulfide quantum dots (PbSQDs-505IL) is also solvent-free (no significant weight loss before 150^{o}C) with a decomposition temperature >200^{o}C and a residue content of 4.5% w/w (Fig. 2.10b). The initial weight losses of the PbSQDs-505IL and XTJ505 were close to each other, and both occurred near 200^{o}C in nitrogen because of the degrading of the polymer. However, comparing the decomposition temperatures derived from the first derivative of weight loss with respect to temperature shows that the encapsulated nanocomposite has a higher temperature (340 > 308^{o}C) than pure free polymers. The increased interactions between the polymer and the core are the main reasons for improved thermal stability.

The PbSQDs-505IL has relatively lower residue content than previous functionalized materials. Because of the lack of strong covalent bonding between organic (polyetheramine) and inorganic (lead sulfide) components, the lead sulfide nanocrystal required a higher loading of the polyetheramine to protect, isolate, and saturate its surface in order to avoid self-aggregation [24].

REFERENCES

1. Bratskaya, S.; Schwarz, S.; Laube, J.; Liebert, T.; Kulicke, W. M.; *Macromol. Mater. Eng.*, ***2005***, 290, 778-785
2. Pefferkornl, E.; Widmaierl, J.; Graillat, C.; Varoqui, R.; *Progr Colloid Polyrn Sci*, ***1990***, 81, 169-173
3. Xie, H.; Tkachenko, A. G..; Glomm, W. R.; Franzen, S.; Feldheim, D. L.; *Anal. Chem.*, ***2003***, 75, 5797-5805
4. Moulai Mostefa, N.; Tir, M.; J. A.; *Desalination*, ***2004***, 161, 115-121
5. Niemeyer C. M.; *Angew. Chem. Int. Ed*., ***2001***, 40, 4128-4158
6. Bourlinos, A. B.; Giannelis, E. P.; Archer, L. A.; Fytas, G.; *Eur. Phys. J. E*., ***2006***, 20, 109-117
7. Bourlinos, A. B.; Stassinopoulos, A.; Giannelis, E. P.; *Small*, ***2006***, 2, 513-516
8. Bourlinos, A. B.; Chowdhury, S. R.; Archer, L. A.; Giannelis, E. P.; *Adv. Funct. Mater.*, ***2005***, 15, 1285-1290
9. Rodriguez, R.; Herrera, R.; Archer, L. A.; Giannelis, E. P.; *Adv. Mater.*, ***2008***, 20, 1-6
10. Jeon, B. J.; Hah, H. J.; Koo, S. M.; *Journal of Ceramic Processing Research*, ***2002***, 3, 216-221
11. Reddy, V. R.; Currao, A.; Calzaferri, G.; *Journal of Physics: Conference Series*, ***2007***, 61, 960-965
12. Beyer, D.; Knoll, W.; Ringsdorf, H.; Elender, G.; Sackmann, E.; *Thin Solid Films*, ***1996***, 284, 825-828
13. Leyden, D. E.; Shreedhara Murthy, R. S.; Blitz, J. P.; Rachetti, A.; *Mikrochim. Acta*, ***1988***, 2 53-56
14. Kuroda, K.; Shimojima, A.; *Mat. Res. Soc. Symp. Proc*., ***2002***, 707, V2.8.1-12

15. Pecora, R.; *Dynamic Light Scattering Applications of Photo Correlation Spectroscopy*
16. Enüstün, B. V.; Turkevich, J.; *J. Am. Chem. Soc.*, ***1963***, 85, 3317-3328
17. Ofir, E.; Oren, Y.; Adin, A.; *Desalination*, ***2007***, 204, 33-38
18. Malvern Instruments Ltd.; *Zetasizer Nano Series User Manual*
19. Chen, W. B.; Feng, H. Q.; He, D. Y.; Ye, C. H.; *Journal of Applied Polymer Science*, ***1998***, 67, 139-147
20. Kong, Y.; Hay, J. N.; *Polymer*, ***2002***, 43, 3873-3878
21. Casado, R. M.; Lovell, P. A.; Navabpour, P.; Stanford, J. L.; *Polymer*, ***2007***, 48, 2554-2563
22. Kim, M. K.; Kim, C. A.; Suh, K. S.; *Synthetic Metals*, ***2004***, 146, 197-199
23. Tiarks, F.; Landfester, K.; Antonietti, M.; *Macromol. Chem. Phys.*, ***2001***, 202, 51-60
24. Callan, J. F.; Mulrooney, R. C.; Kamila, S.; *J Fluoresc*, ***2008***, 18, 1157-1161

CHAPTER 3

SURFACE PROPERTIES OF IONIC NANOPARTICLES AND POLYMER COMPOSITES

3.1 Surface Characterization

3.1.1 Bulk and Thin-film Properties

A series of surface characterizations was undertaken to study the surface properties of the nanoparticle fluids. The first method was to spread the fluid on solid surfaces and study their wetting behavior. Wetting is influenced by physical chemistry (wettability), statistical physics (wetting transition), long-range forces (van der Waals), and fluid dynamics [1-4].

A significant amount of effort has been devoted to the dewetting behavior of thin films in two-dimensional systems [5]. Meyer and Braun [6] generated ordered polymer drops on chemically modified surfaces by microcontact printing and reported that the holes are formed exclusively on the hydrophilic areas because of poor wettability with the polymer film. Kargupta and Sharma [7] subsequently developed a theoretical explanation for the controlled dewetting process on a chemically heterogeneous pattern, finding that the film breakup is due to some potentially destabilizing nonwettable sites when the pattern spacing is below a certain critical length.

To evaluate the wetting or dewetting ability of NIMs, we spin-coated the liquid NPs onto different substrates using different NP concentrations, core/corona/canopy volume fractions, and chemistry. The samples where then exposed to air prior to any measurement. Using the Ethomeen 18/25 system as an example, when the volume fraction of canopy was increased, dewetting of the thin-film became more severe; X-

ray diffraction showed a clear variation in reflected intensity when the volume fraction of the core changed from 35 wt.% to 10 wt.% (Fig. 3.2). We used Interferometric Profiler to provide surface topology and roughness information. The 10 wt. %-core sample had higher surface roughness and it was less homogeneous than the 35wt.%-core sample (Fig. 3.1) before and after dewetting. We believe that the canopy played an important role during the dewetting transition. Polyethylene glycol-containing copolymers are hydrophilic and thus susceptible to moisture which can trigger the dewetting process.

Figure 3.3 shows the contact angle for one NP fluid on a Si wafer (left) and Teflon (right) respectively. All nanoparticle fluids have consistently low static contact angles (<10 degree) on clean silicon wafers. Water usually has a contact angle of around 60 degrees on the same substrate. On the PTFE (Teflon)-based substrates, nanoparticle fluids still have lower contact angles (43-74 degrees) than deionized water (106 degrees), so ionic nanoparticles can wet well both on polar (Si wafer) or apolar (Teflon) substrates, and could be classified as amphiphilic materials. The physical properties of ionic nanoparticles come mainly from their unique chemical composition, which successfully integrates the ionic interaction and hydrophobic/hydrophilic segments.

In general, high polarity comes with high surface tension. Using pendent-drop experiments, NIMs showed extremely low surface tension (<37 dyne/cm) (Fig. 3.4) at room temperature. The surface tension of the NIMs was strongly related with the selected canopy materials.

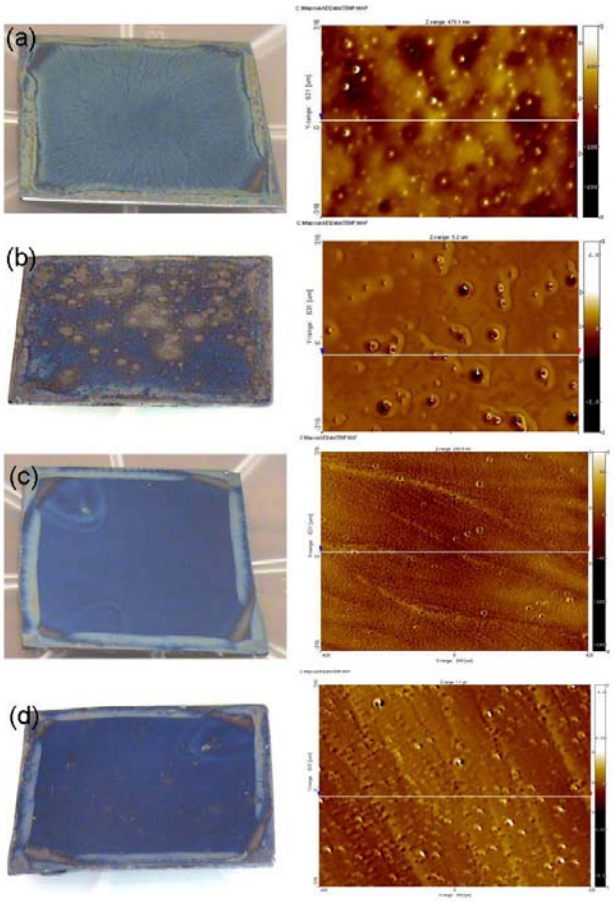

Figure 3.1 Comparison of the de-wetting situation with different core/shell fraction NIMs, real-time images (left), profilometer images (right). (a)(b) 10 wt.% core before and after de-wetting; (c)(d) 35 wt. % core before and after de-wetting. *Surface roughness (a)100nm, (b)1.2µm, (c)20nm, (d)140nm.

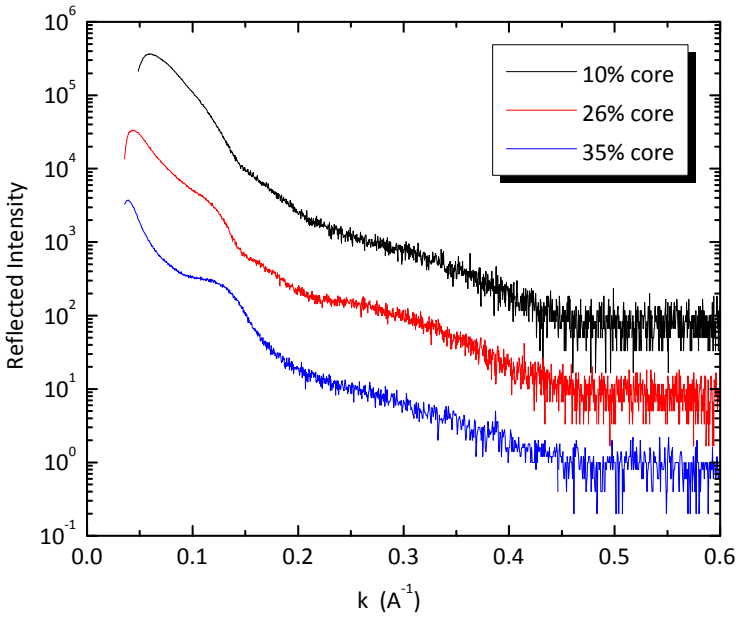

Figure 3.2 Thin-film state reflected intensity varied with different core/canopy fraction NIMs

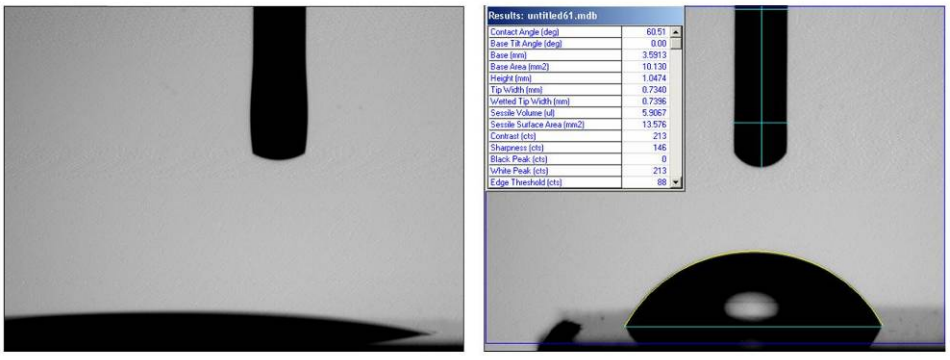

Figure 3.3 Static contact angle measurement; NIMs wetted on Si wafer (left) and PTFE (right) substrates at room temperature.

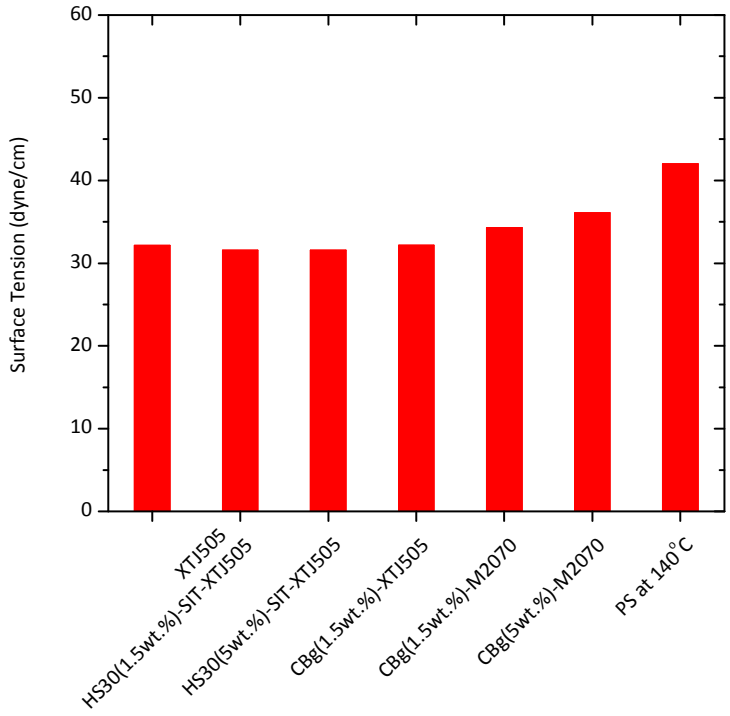

Figure 3.4 Surface tension measurements nanoparticle fluids (at room temperature)

3.1.2 Surfactant-like Behavior

Most surfactants are amphiphilic molecules in which part of the molecule is hydrophilic and another part is hydrophobic. In aqueous solutions, surfactants tend to aggregate and form stable sub-structures called micelles, where the hydrophobic segments of the molecules are protected away from water. Depending on the particular molecular architecture of the surfactant molecule [8], a variety of microstructures can form. Possible aggregate structures are spherical micelles, worm-like micelles [9], spherical vesicles, lamellar sheets, and other topologies.

In all the generations of nanoparticle-based ionic materials, the amphiphilic copolymers /oligomers (ex: Jeffamine) were broadly used as canopy components because of their versatile functionalities. Jeffamine M2070 consists of poly(ethylene

oxide) (PEO) and poly(propylene oxide) (PPO) blocks. The presence of PEO segments allows the copolymers to have versatile properties such as hydrophilicity [10], crystallinity [11], and surfactancy [12].

Interfacial phenomena play an important role in surfactant applications. The stability of emulsions, thin-film dynamics, the action of antifoams and demulsifiers, and refining processes occur at fluid interfaces which are in a constant state of flux [13]. The interfacial behavior is strongly controlled by surface active agents.

Static interfacial tension measurements (Wilhelmy plate and the du Noüy ring methods) cannot provide sufficient information about the interface. The measured values may not correspond to equilibrium interfacial tension values. However, dynamic methods (drop volume and drop shape techniques) are able to help us observe adsorption kinetics [14-16] over a substantial period of time.

Interfacial tension measurement by drop shape analysis [17] is based on the principle that the shape of a drop formed at the tip of a needle depends on the interfacial tension. Based on Young-Laplace equation [18] and Misak simulation [19], the interfacial tension is obtained via a nonlinear curve fitting of theoretically calculated drop profiles with measured drop profiles.

We first used a commercial nonionic surfactant (Brij78) [20] to measure the interfacial tension of liquid-liquid (hexadecane/water) [21] mixture under controlled conditions. Figure 3.5 shows the experimental relaxation data at one surfactant concentration that was below the critical micelle concentration (CMC). The interfacial tension decreases slowly until it reaches a plateau value. The typical initial slow and then rapid relaxation process, followed by another slower process toward the equilibrium interfacial tension did not appear in this experiment. The diffusion/absorption-controlled kinetics were complicated and depended heavily on the experimental design [22]. The failure to observe the transition (interfacial tension

versus time) usually happened at relatively low (slow diffusion) and high (quick diffusion) concentrations. In our system, the high diffusion coefficients or quick absorption of the surfactant could be possible reasons that the drop relaxed too quickly to show the transition. However, we were still able to determine the relative minimum surface tension before the drop left the needle, which is close to the equilibrium state.

Instead of equilibrium interfacial tension, the dynamic minimum interfacial tension isotherm for the aqueous drop immersed into the oil is shown in Figure 3.6. The shape of the isotherm is typical for such nonionic isotherms. The CMC (2.3E-5~1.5E-5 M) was close to that reported in the literature [20].

Figure 3.7 compare the pure canopy (M2070) [23] with the hybrid ionic nanoparticles (HS30-SIT-M2070). Both nanoparticles show a rapid decrease in dynamic interfacial tension at similar low concentrations. These results suggest that the NP liquids appear similar surfactant behavior to the neat canopy.

Surface tension was derived from the drop shape by the equation:

$$\gamma = \frac{\Delta\rho g S_E^{\,2}}{H}$$

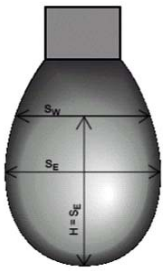

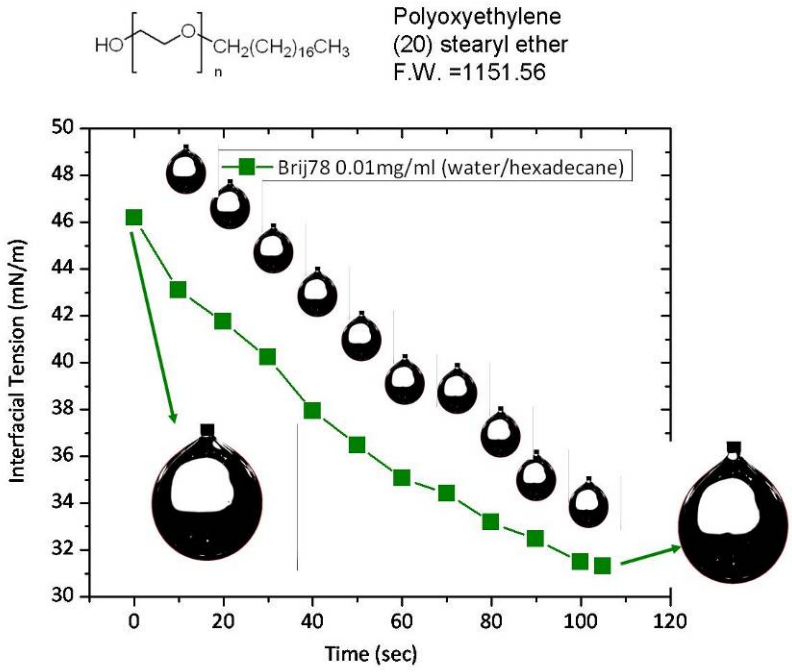

Figure 3.5 Dynamic interfacial tension of a relaxing hexadecane/aqueous Brij 78 interface as a function of time.

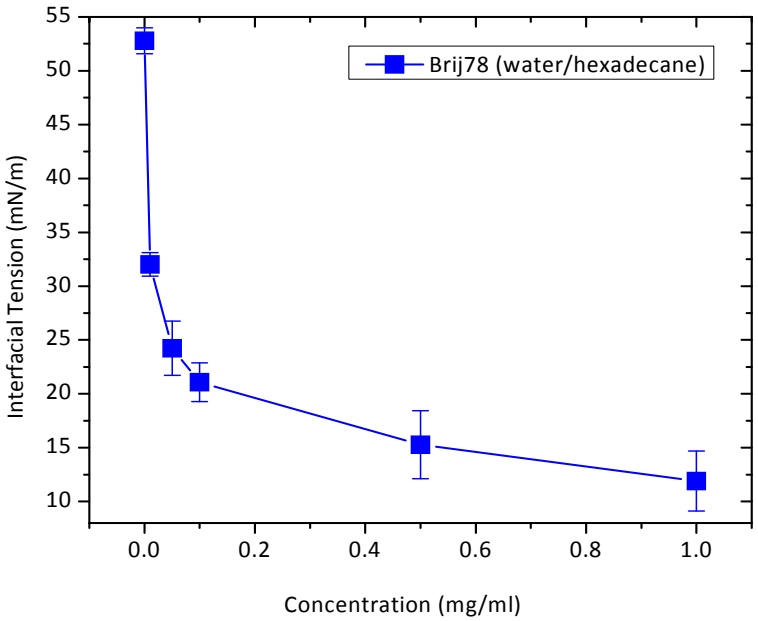

Figure 3.6 Dynamic interfacial tension of hexadecane/aqueous Brij 78 solution system as a function of concentration.

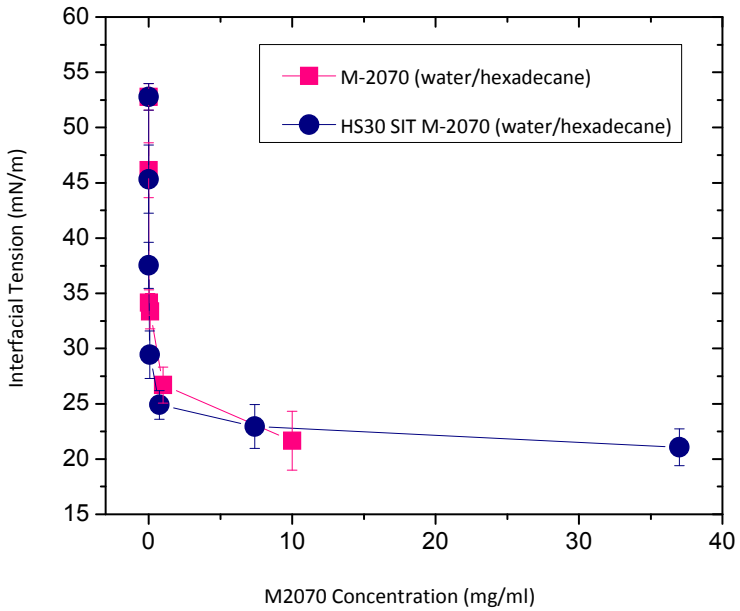

Figure 3.7 Dynamic interfacial tension of hexadecane/aqueous M2070 and HS30-SIT-M2070 solution systems as a function of M2070 concentration.

3.1.3 Thin Film Deposition

When an unmodified substrate is used, the stability of the deposited NP films is relatively low. NIMs were easily washed out from the substrates by different solvents, including water (Fig. 3.8), diiodomethane, and polydimethylsiloxane (PDMS). To further increase the adhesion to the substrate we used an electrostatic attraction, a technique similar to the layer-by-layer deposition of oppositely charged species [24] that has emerged as one of the standard preparations of composite thin films and multilayers (Fig. 3.10). The first step was to obtain a self-assembled monolayer (SAM) [25-29] by using hydrolytic deposition of functional silanes (positive charge carriers). In that process, four sub-steps take place simultaneously: hydrolysis, condensation, hydrogen bonding, and bond formation. The second step, relies on the electrostatic interaction between the negative charged sulfonate groups at the surface of the NIMs, and the positively charged substrate. A combination of scanning probe microscopy, ellipsometry, XPS, and X-ray reflectivity was used to elucidate the surface morphology and properties. Dynamic contact angle measurements were mainly used to probe the thin film stability, roughness, chemical heterogeneity, and molecular mobility [30-37].

The research could be extended to control the deposition of successive layers that can include solutions containing polyelectrolytes, the electrodeposition of metal nanoparticles [42], the deposition of nanoparticle monolayers via the Langmuir-Blodgett technique [43], sol-gel chemistry-based deposition of nanoparticles [44], and in situ synthesis of nanoparticles using polymeric thin films as templates [45].

Iler [46] was the first to disclose a novel method for creating multilayers of inorganic colloidal particles. He reported that multilayers of oppositely charged nanoparticles can be assembled by the sequential adsorption of oppositely charged nanoparticles onto substrates from aqueous suspensions. Cohen [38-41] was inspired

by Iler's theory in utilizing self-assembled nanoparticles to form conformal and uniform thin films with precise control over chemical and physical properties. We reexamined all-nanoparticle thin-film coatings by integrating the methods described by Iler and Cohen (oppositely charged nanoparticles) and the techniques demonstrated by Decher [47] (aqueous-based layer-by-layer).

Figure 3.9 shows the water dynamic contact angles obtained for stabilized coatings prepared under these conditions on a silicon wafer. The water advancing contact angle of a clean silicon wafer was 60 degrees, which was lower than that of silane-based SAM (wafer +silane20, 95 degree). The long hydrocarbon and silane functional groups of the SAM were expected to prevent water absorption and enhance the hydrophobic performance of the sample. Generally, the surface properties are influenced by the local arrangement of chemical moieties, when they are exposed to solvent (water). No large segmental motion or migration of macromolecules is required for the change of surface configuration, which can be achieved by a relatively small segmental motion, such as rotating hydrophilic segments to the surface or rotating hydrophobic segments away from the surface to reach an energy stable state. The last sample was made by attaching negatively charged nanoparticles to the positively charged substrate. The SAM layer provides a sufficient electrostatic attraction toward the ionic nanoparticles. The advancing contact angle (77 degree) is right between those of the untreated Si wafer and that modified by SAM. Furthermore, the angle stays constant after multiple cycles suggesting that the thin film is stable and adheres well to the substrate.

In our model system, the SAM intermediate layer was necessary to provide sufficient electrostatic attraction for the deposition of the ionic nanoparticles. We optimized the film condition by varying the reaction parameters, including concentration of the silane, reaction temperature, and time (Fig. 3.11). Low

concentration and short reaction time led to a rougher surface. In aqueous solutions, an insufficient concentration of the silane exaggerated the self-polymerization of the silane and created more aggregation domains on the substrate. A short duration time led to incomplete silanization, and the products made by side reactions dominated the surface distribution. Finally, a smooth (0.66 nm) silane-based surface was achieved by using a 6 wt. % solution of silane and 20 hours of reaction time.

Negatively charged silica (Fig. 3.12) and gold (Fig. 3.13) nanoparticles were tested as the primary layer of all-nanoparticle multilayer coatings. A positively charged SiO_2 nanoparticle was prepared for counter ion deposition. To characterize the primary layer comprised of either SiO_2 or Au nanoparticles, we developed a characterization technique based on AFM that allowed us to determine the surface morphology and topology of these all-nanoparticle thin films. Deposition time and the ionic strength of the solution had a great impact on the layer formation and degree of aggregation.

As Iler mentioned, all-nanoparticle multilayer coatings are porous in nature because of the presence of interstitial void volume. These nanopores may offer self-cleaning, antireflection and antifogging properties. The concept of aqueous-based LbL assembly of oppositely charged nanoparticles offers a simple approach to obtain all-nanoparticle multilayer thin-film coatings on various substrates. It also represents a general way to create multifunctional coatings by incorporating different types of nanoparticles that exhibit catalytic, magnetic, optical, and metallic properties.

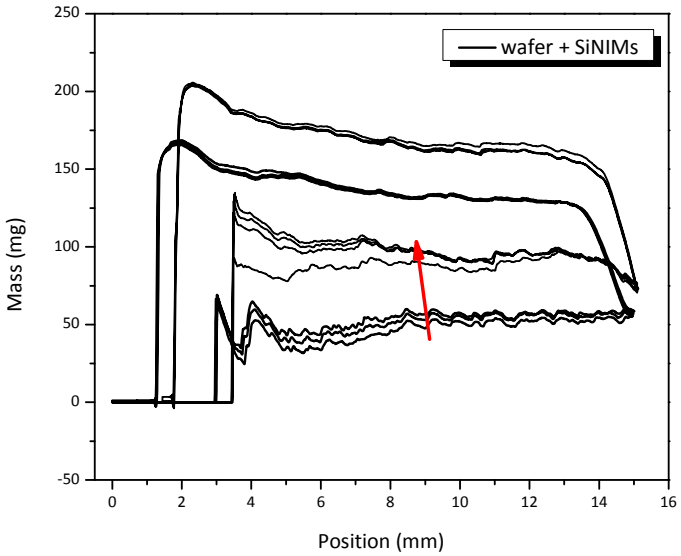

Figure 3.8 Dynamic contact angle circles of spin-coating SiNIMs/wafer in water.

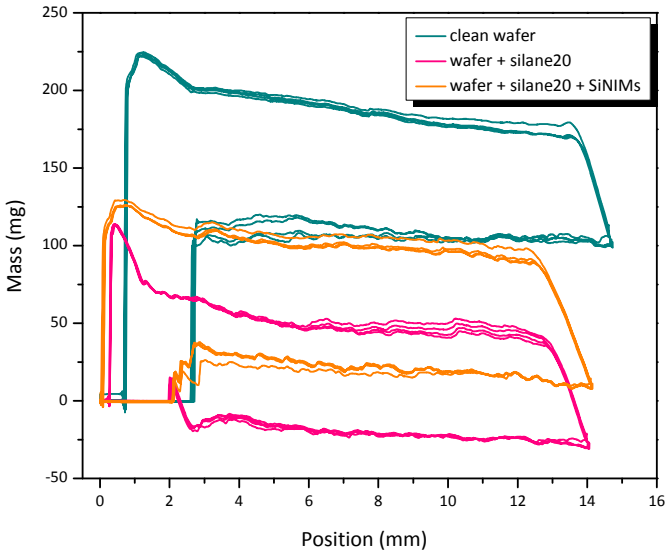

Figure 3.9 Dynamic contact angle cycles of clean wafer; silane + wafer; SiNIMs silane + wafer in water.

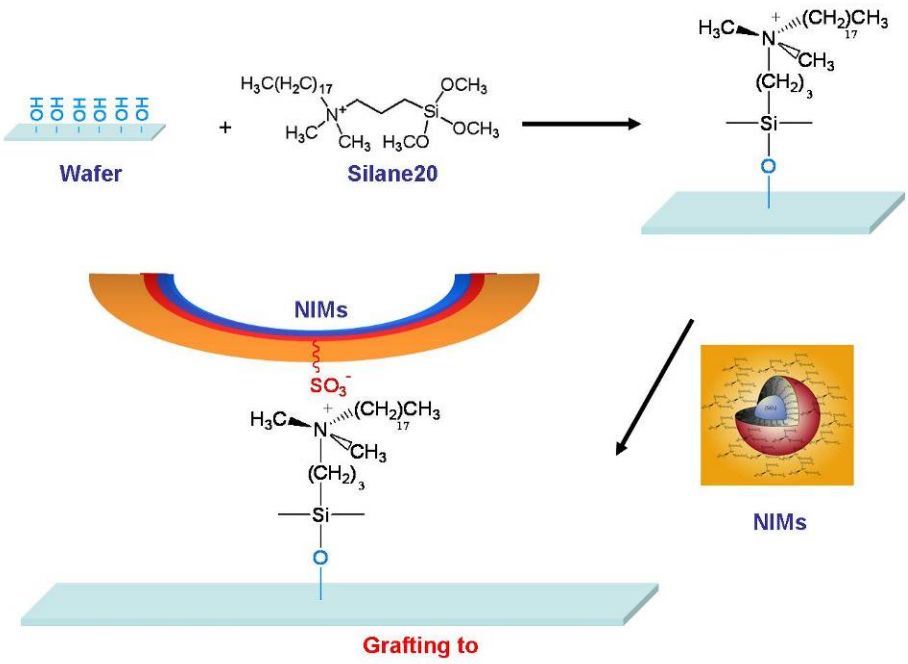

Figure 3.10 Preparation of SiNIMs / silane-based SAM / wafer

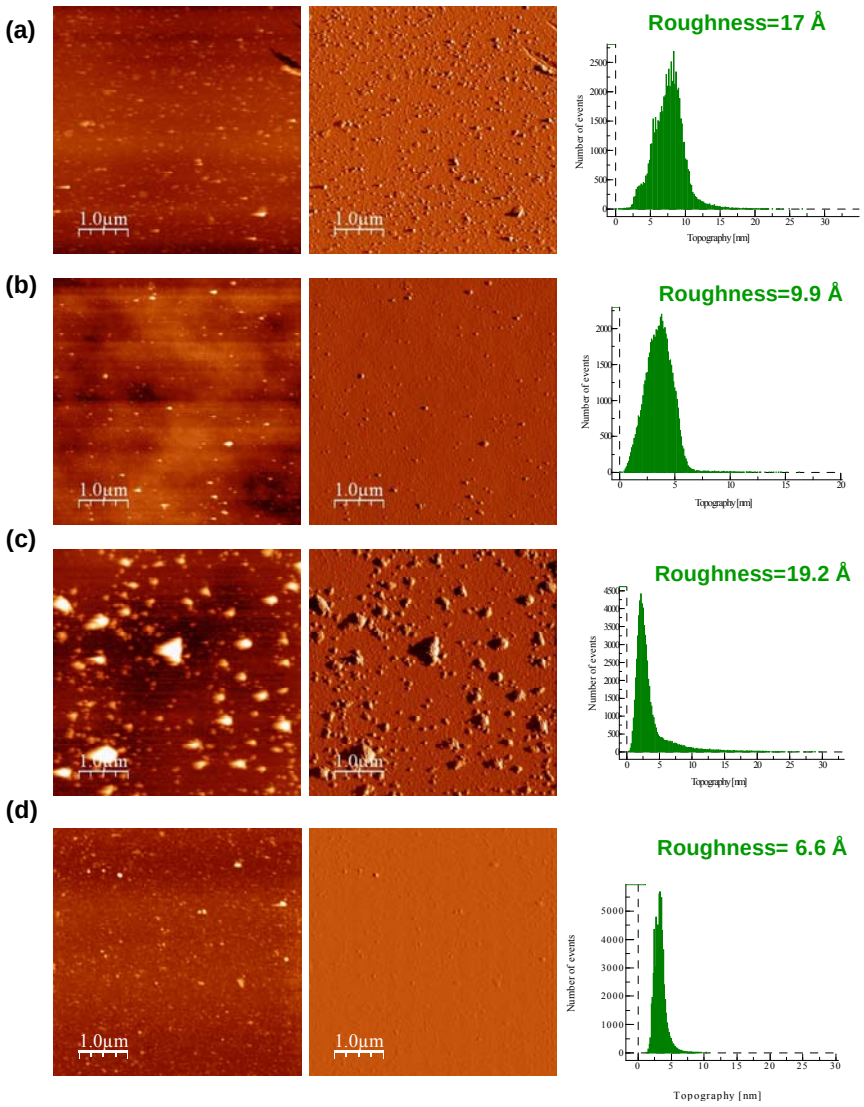

Figure 3.11 AFM images of silane-based SAM under different concentration and duration times: (a) 2%, 20hr; (b) 5.8%, 20hr; (c) 5.8%, 30min; (d) 6%, 20hr. (left: height, right: amplitude)

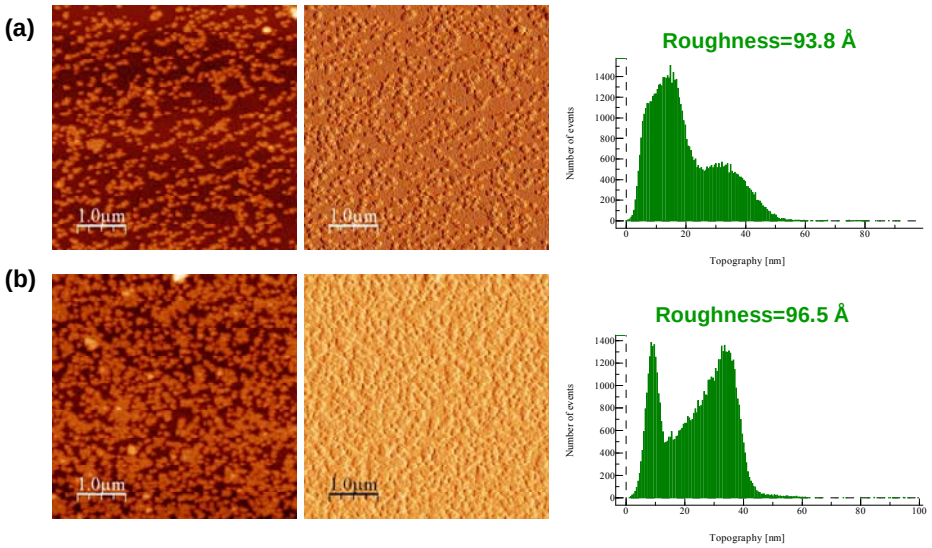

Figure 3.12 AFM images of Silica-based primary layer under different concentration of sodium chloride salt: (a) 5mMSiO_2+0.1MNaCl, (b) 5mMSiO_2+0.5MNaCl. (left: height, right: amplitude)

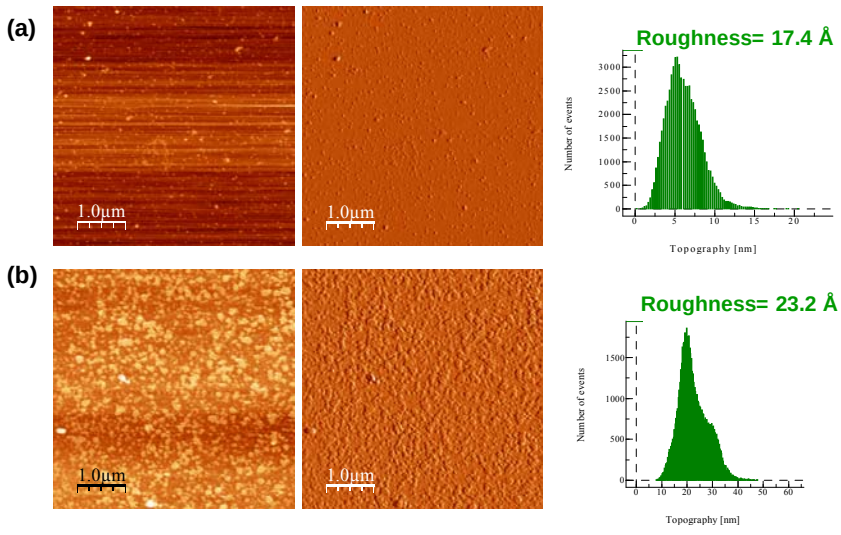

Figure 3.13 AFM images of gold-based primary layer under different deposition time: (a) 2hr, (b) 20hr. (left: height, right: amplitude)

3.2 Nanoparticle fluids as additives in Polymer Matrices

3.2.1 Sample Preparation

Carbon Black-based Ionic Nanoparticles (CBf-M2070, CBg-M2070)

Materials. Surface-functionalized liquid-like nanoparticles: Carbon black-based nanoparticles. Carbon black was obtained from Cabot and used as received. Two types of carbon black particles, carboxyl-terminated (CBf) and sulfonate-terminated (CBg) (diameter = 50-100 nm), were selected as precursors on the basis of their dispersion, polarity, reactivity, and surface charge density. Reaction of the acidic groups of carbon black nanoparticles with a basic polyetheramine ($(CH_3(CH_2CH2O)_x$-$(CH_2CHCH_3O)_yNH_2$, X/Y=31/10, Mw=2000, Jeffamine M2070, Huntsman) gave rise to black molten salts whose fluidity can be adjusted by controlling the volume fraction of the cores.

Silica-based Ionic Nanoparticles(HS30-SIT-M2070)

Ludox HS-30 (diameter ~ 7nm, Sigma Aldrich) colloidal silica was used as a seed particle. Surface functionalized nanoparticles were prepared as described previously (ch.2).

Blending Ionic Nanoparticles with Polymers

Surface-functionalized nanoparticles were used as a diluted suspension in toluene. To study the interface between liquid-like nanoparticles and solid polymer matrices with various molecular weights, we either spin-coated or solvent-cast films of nanocomposites onto silicon wafers that had been cleaned with piranha solution to remove organic impurities.

3.2.2 Contact Angle Measurements

As shown in figure 3.3, the relatively low contact angles on (polar) silicon wafer (< 15 degrees) and (apolar) Teflon substrates (60 degrees) indicate good wettability of NP fluids in both materials. This behavior points to the amphiphilic nature of the liquid-like nanoparticles. Figure 3.14 refers to the system of liquid-like nanoparticles (silica-based, weight percentage from 2 to 10) in polystyrene (MW = 400K g/mol) that is typically incompatible with the canopy.

After the solvent was dried and before annealing, the surface hydrophilicity already showed a clear relationship to the loading of nanoparticles. With sufficient loading, it would be easier for these hydrophilic nanoparticles to saturate the material surface, rearrange the surface composition, and yield a lower water contact angle.

During annealing, the surface hydrophilicity appeared to be inversely proportional to the annealing time because the nanoparticles tended to migrate from the surface to the bulk, forming stable aggregates within the polymer matrix in order to reach a favorable energy state. Gradually, the nanocomposites lost their hydrophilic characteristics.

The most important discovery was that any desired hydrophilicity of the material could be achieved by simply controlling the annealing condition. We could freeze the transition at any stage as required and preserve the specific particle size, geometry and dispersion inside the polymer matrix. These new materials also came with promising stability. Even after rinsing with clean water several times, the surface hydrophilicity still remained constant. These results confirm that the nanoparticles are strongly incorporated into the polymer matrix related to possible dissociation from the ionic structure of nanoparticles (core-canopy separation) and the chance of losing unbound nanoparticles.

At long annealing times (130°C, up to 23 hr), the nanoparticles underwent major spatial reorganization within the polymer matrix. The underlying mechanism involved contributions from polarity differences and surface tension discrepancies.

At the same time, carbon black-based nanoparticles with the same surface chemistry as the silica nanoparticles showed fundamentally different behavior (Fig. 3.15), as the nanoparticle tended to migrate toward the surface, without significant self-aggregation. Therefore, the advancing contact angles were found to increase along with annealing time. It is likely that the carbon black-based nanoparticles have a bigger particle size than those in the silica-based system, and a lower surface active area, so that the polarity and surface tension discrepancy with the polymer matrix were not major driving forces that would force them to form stable aggregations.

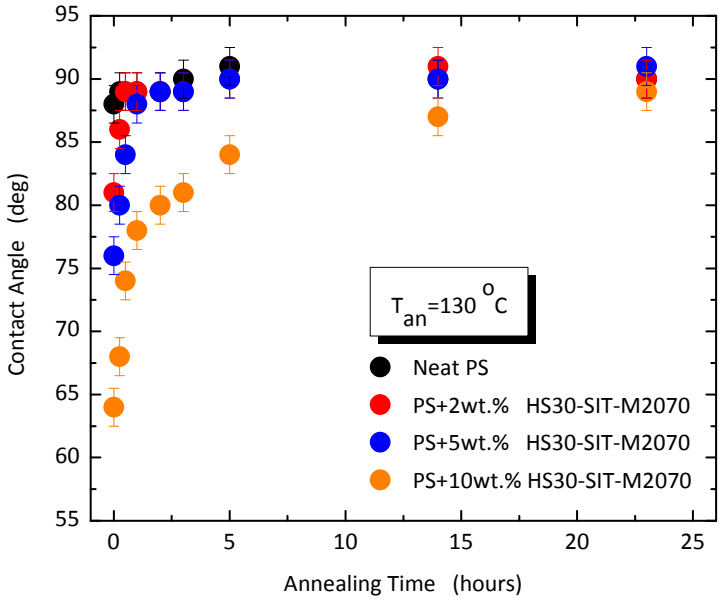

Figure 3.14 Water contact angle of (HS30-SIT-M2070)-PS composites (neat, 2wt.%, 5wt.% and 10wt.%) versus annealing time

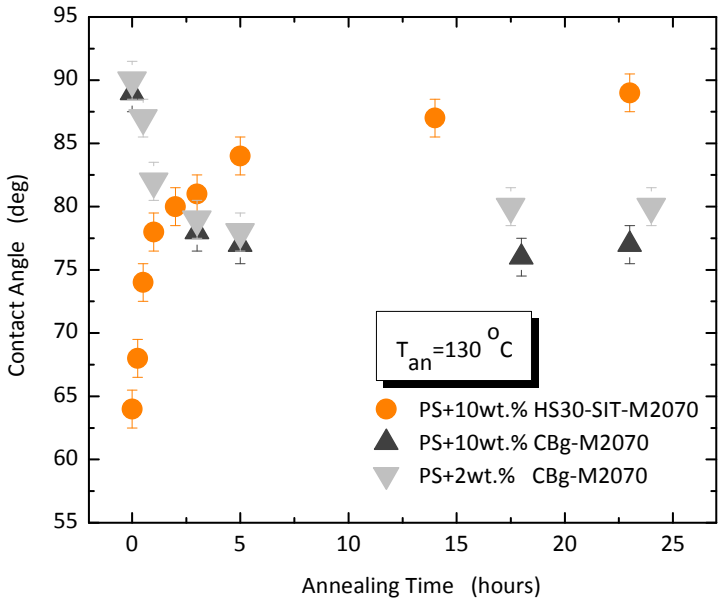

Figure 3.15 Water contact angle of (CBg-M2070)-PS composites (2wt.% and 10wt.%) versus annealing time

3.2.3 SEM Measurements

SEM measurements provided useful insights about the dynamic motions inside the polymer melt. The surface of polystyrene composites (10 wt. % (HS30-SIT-M2070)-PS, before annealing) (Fig. 3.17) appeared to be covered by large spherical assemblies with a uniform diameter of 200 nm, which was not observed in neat PS (Fig. 3.16). It is likely that those assemblies result from a micelle-like self-organization mechanism. We also confirmed this critical assembling transition by using the dynamic light scattering (DLS), which showed that the formation of the assembly was reversible and could be controlled by concentration.

In the bulk state of the (HS30-SIT-M2070)-PS (underneath the surface) (Fig. 3.18), the dispersion of the aggregation was more random than it appeared on the free surface. We could still identify the similar micelle-like assemblies inside holes in the polymer, which were made from evaporation of the solvent initially trapped by

amphiphlic nanoparticles and therefore, more difficult to remove from the composite. The particle-filled holes play a critical role in manipulating the size and geometry of further micro-sized aggregations because they act as a template that provide a perfect place for soft nanoparticles to reorganize, aggregate and form a strong interface.

The modified nanoparticles have an interesting behavior in the polymer matrix; their morphology evolves from spherical organization (200nm, before annealing) to disk-like aggregation (micro-scale, after annealing, Fig. 3.19). Since the properties depend on the morphology, emphasis was given to controlling the morphology, that is, the state of dispersion of the nanoparticles inside the composite films. The soft particles, easily saturated the holes within the polymer matrix, which yielded various levels of aggregation and created a whole new morphology.

The interfacial particle-particle and particle-polymer interactions were affected by the molecular weight of the polymer matrix. The wetting behavior of nanoparticles can be controlled by surface functionality or grafting density, or by varying the MWs of the polymer matrix with which they are placed in contact. Thus, it is likely that the higher MWs polymer matrix enhances the difference in polarity and surface tension among the particles and polymer matrix. This is a major driving force in determining the dewetting transition, strength of interface, and curvature of aggregation. The rate of the solvent evaporation also plays an important role in the initial drying mechanism. The shape of the aggregation can be controlled from spherical to elliptical to disk-like (Fig. 3.20). We also found that the shape of these micro-aggregates changed with the depth of the sample, which means that the driving force used to compress the soft particle was coming primarily from the z-direction, rather than the x-y direction (Fig. 3.21). Besides the force of gravity, the rate of the solvent evaporation was the main contributor to this anisotropic force.

Several studies have focused on the thermal-mechanical properties of thin-film polymer composites [48-50]. Some studies have showed that the addition of impurities (nanofillers) to polymer films has an impact on the film wetting properties [51, 52]. Heterogeneities on the film substrate have also been related with affecting film dewetting. The evidence available suggests that the particles could segregate/aggregate and modify the polymer-surface interaction.

In the images in figure 3.22, the surface of 2wt. % (CBf-M2070)-PS composites, the carbon black-based nanoparticles showed a completely different morphology than that of silica-base composites. This finding is consistent with carbon black-based nanoparticles migrating to the surface and maintaining individual dimensions in polystyrene matrices. The 10wt. % loading of the nanofillers (Fig. 3.23) easily saturated the composite and showed a higher population of non-aggregated nanoparticles.

The last image (Fig. 3.24) provided information about nanoparticle dispersion and preferred orientation. After adding 10wt. % of silica-based ionic nanoparticles into PDMS-urea copolymer, the subsequent reconstruction in the regions with nanoparticles increased the surface roughness and changed the topography. We also observed a transformation in the morphology caused by the nanoparticles. These ionic nanoparticles were originally around 20 nm in size but, after blending with PDMS, the nanoparticles aggregate into a bigger size (~100nm) and reach a more stable state. The polymer matrix is dominated by PDMS-rich domains of apolar/hydrophobic regions, so only a small portion of the urea rich domains will attract the nanoparticles. The major driving force of the nanoparticle selectivity comes from interactions among the particles themselves, an effect that should be proportionate to the loading of the nanoparticles. We also found a special orientation from the cross-section image: during solvent evaporation, an amount of the particles diffuses to the free surface,

where they are fixed in a certain polymer layer because of their lost mobility. This is why there are many band distributions near the top layer of the polymer matrix.

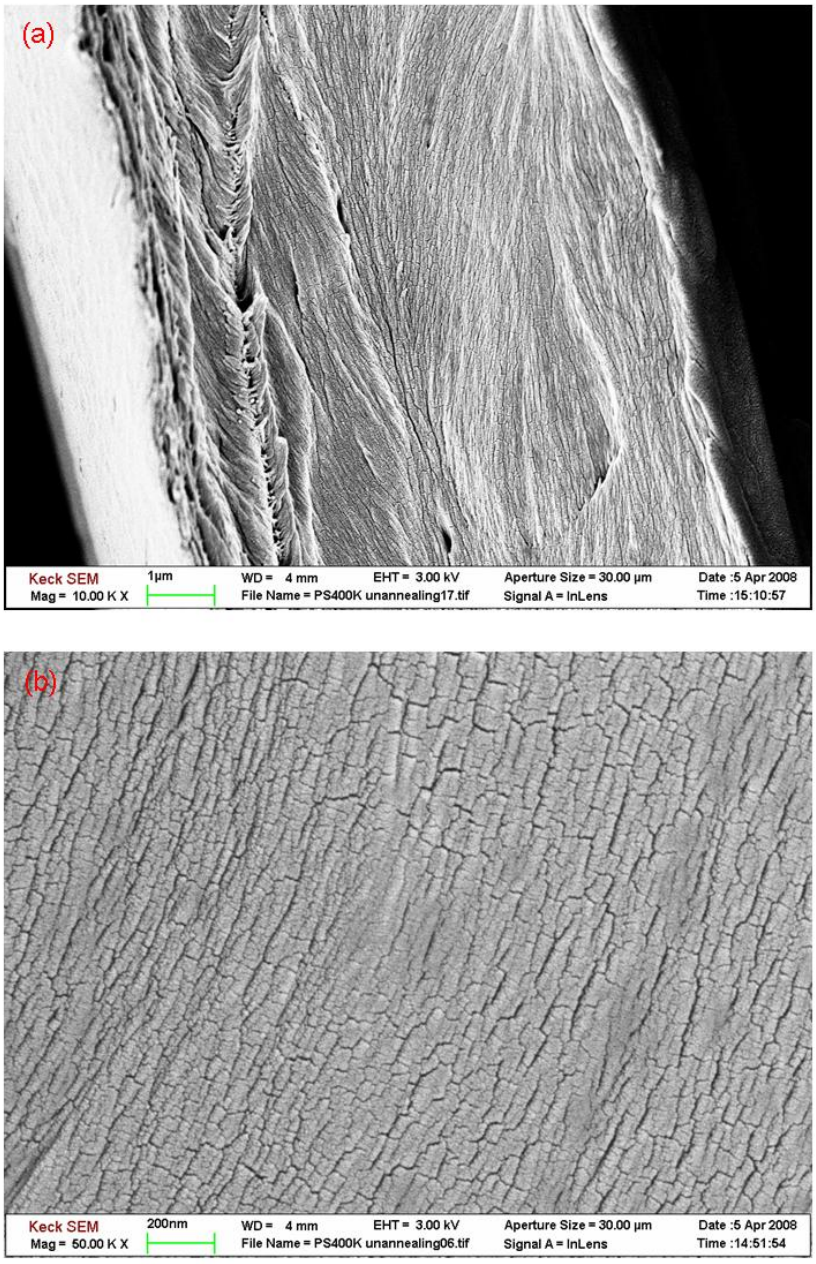

Figure 3.16 SEM images of pure polystyrene (MW = 400k)

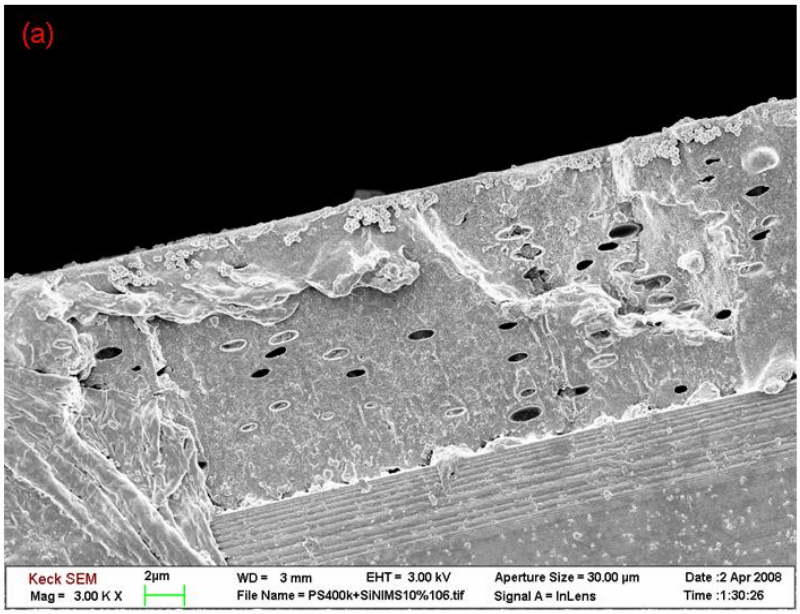

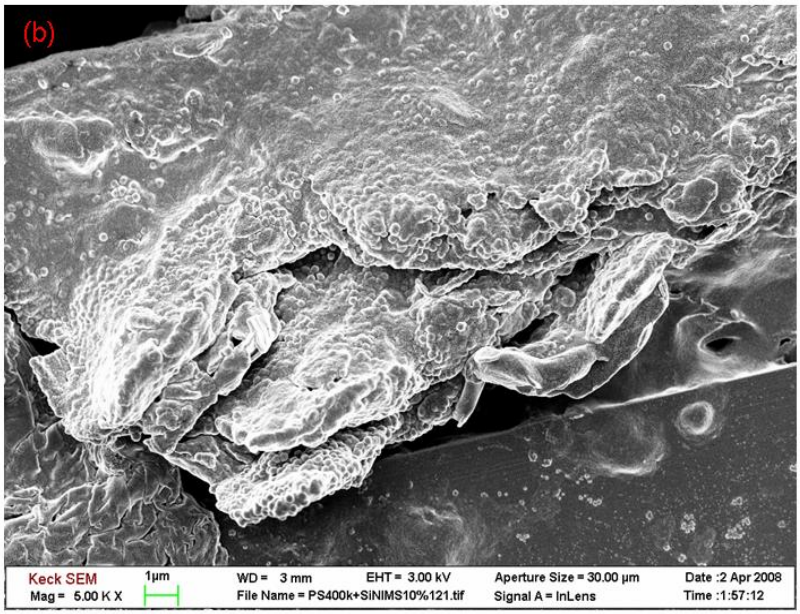

Figure 3.17(a)(b) SEM images of PS400k+10 wt. % (HS30-SIT-M2070) before annealing

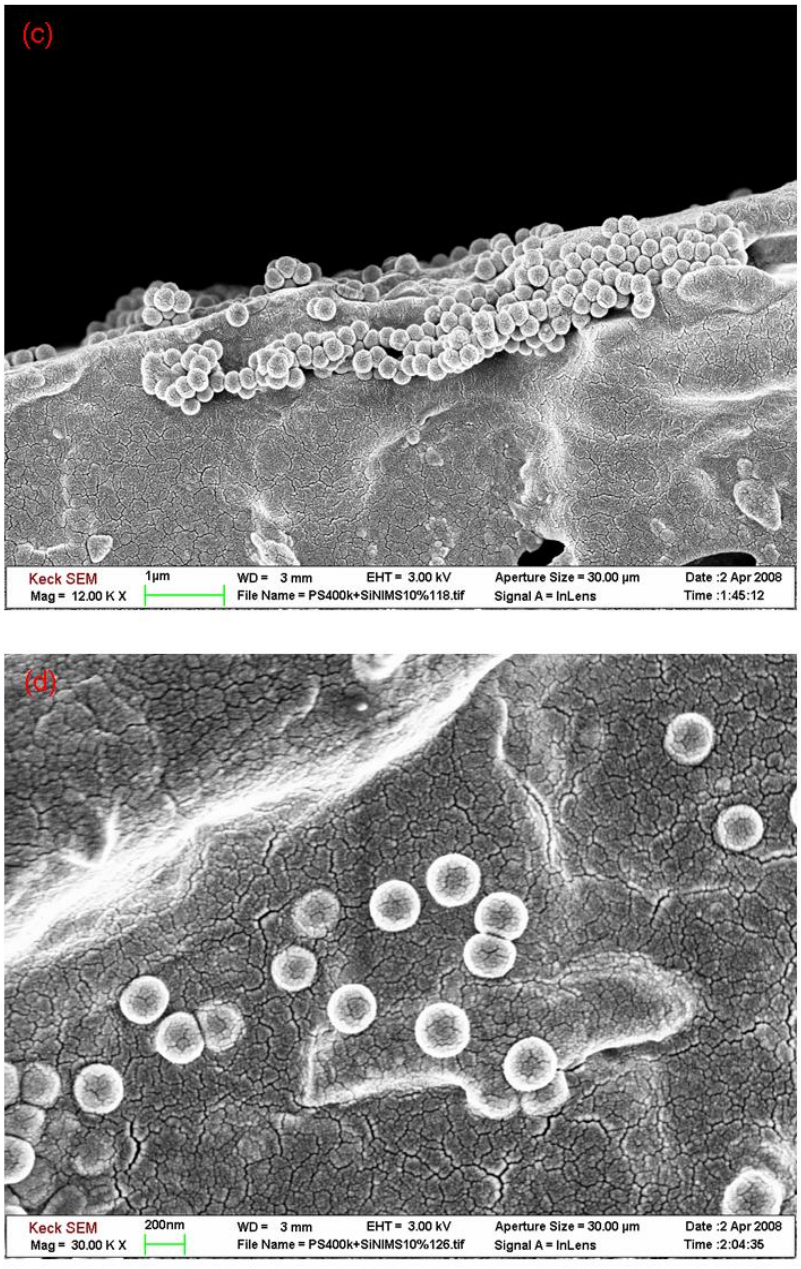

Figure 3.17(c)(d) SEM images of PS400k+10 wt. % (HS30-SIT-M2070) before annealing

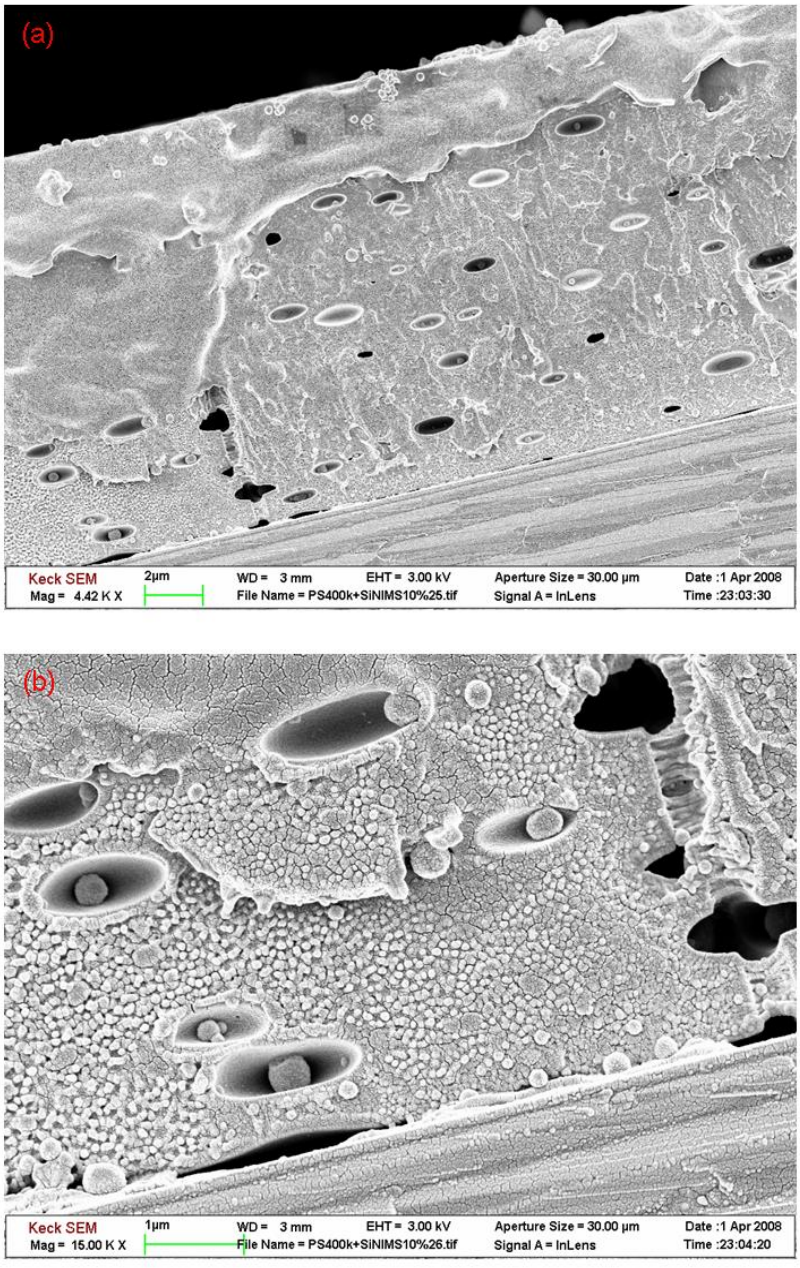

Figure 3.18(a)(b) SEM images of PS400k+10 wt. % (HS30-SIT-M2070), before annealing (cross-section)

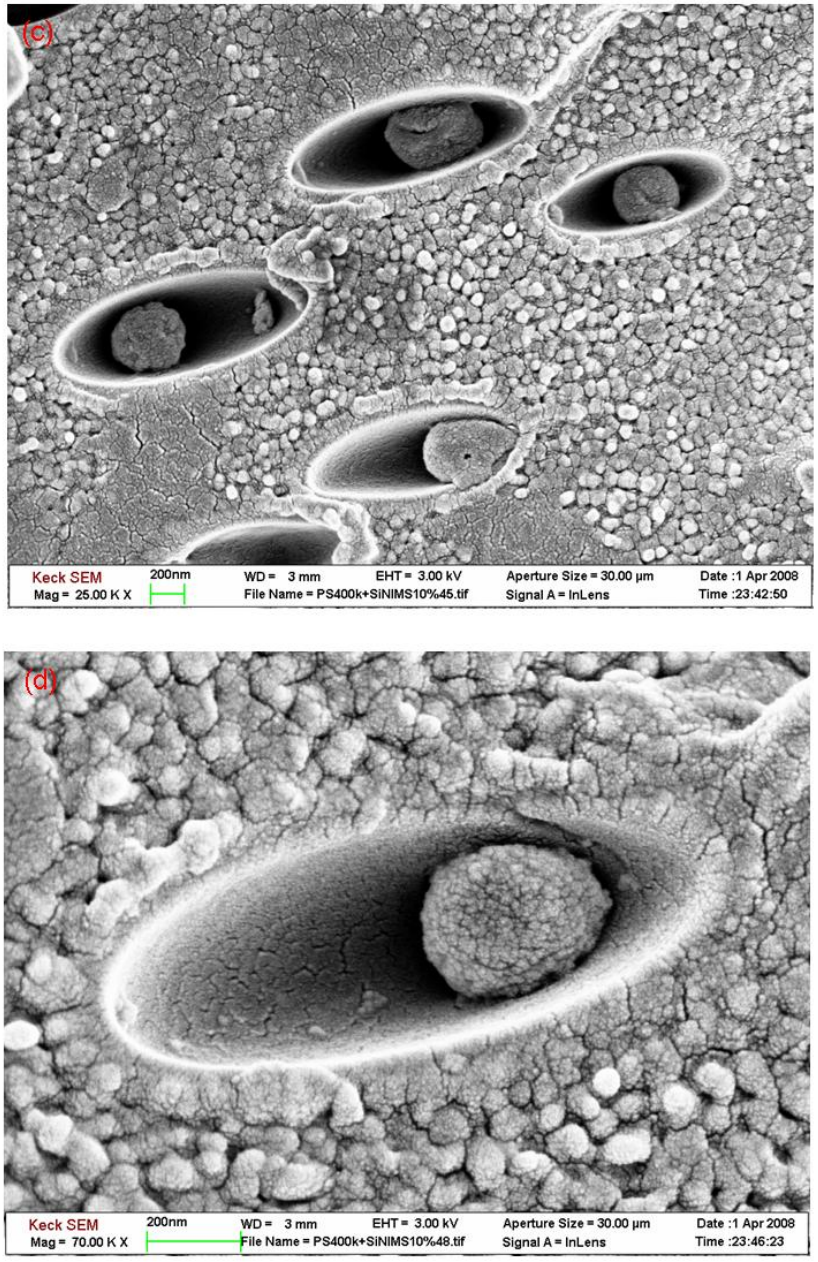

Figure 3.18(c)(d) SEM images of PS400k+10 wt. % (HS30-SIT-M2070), before annealing (cross-section)

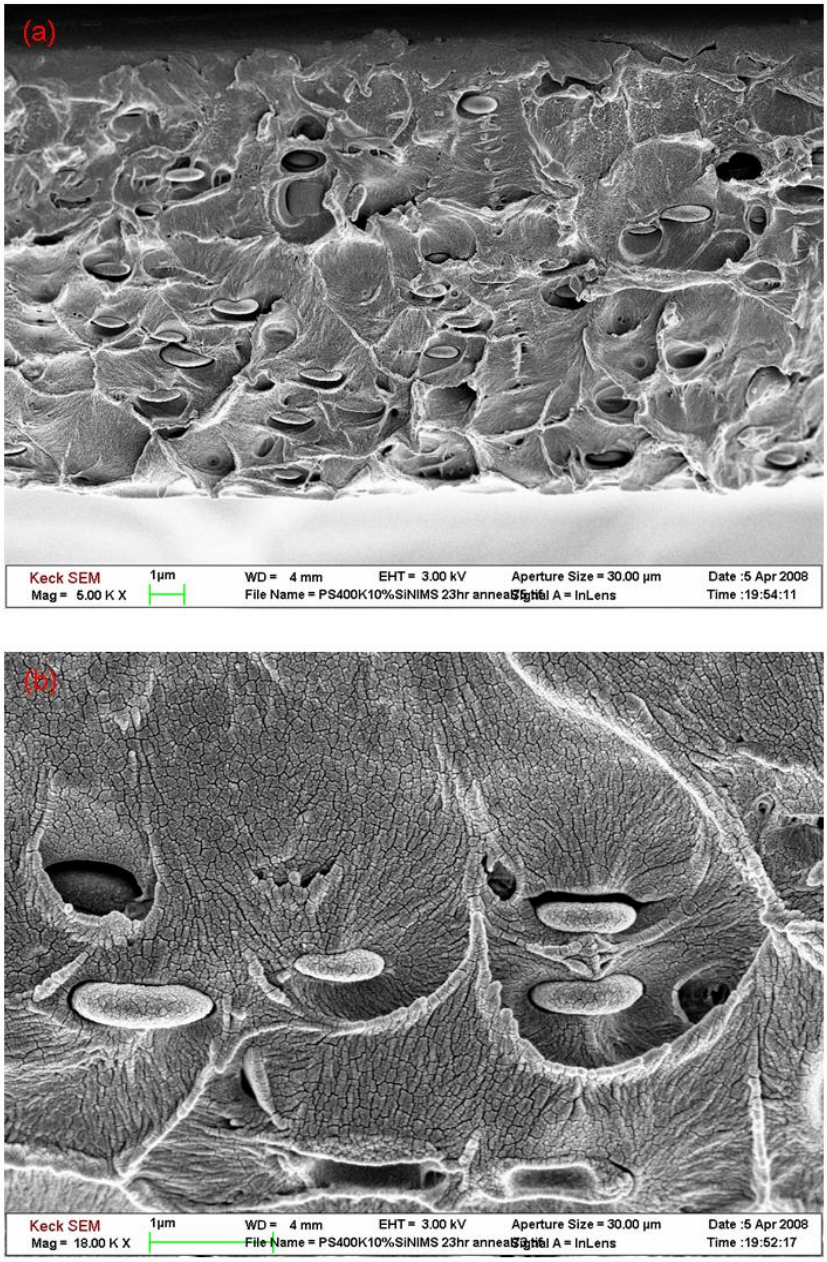

Figure 3.19(a)(b) SEM images of PS400k+10 wt. % (HS30-SIT-M2070), after 23hr annealing (cross-section)

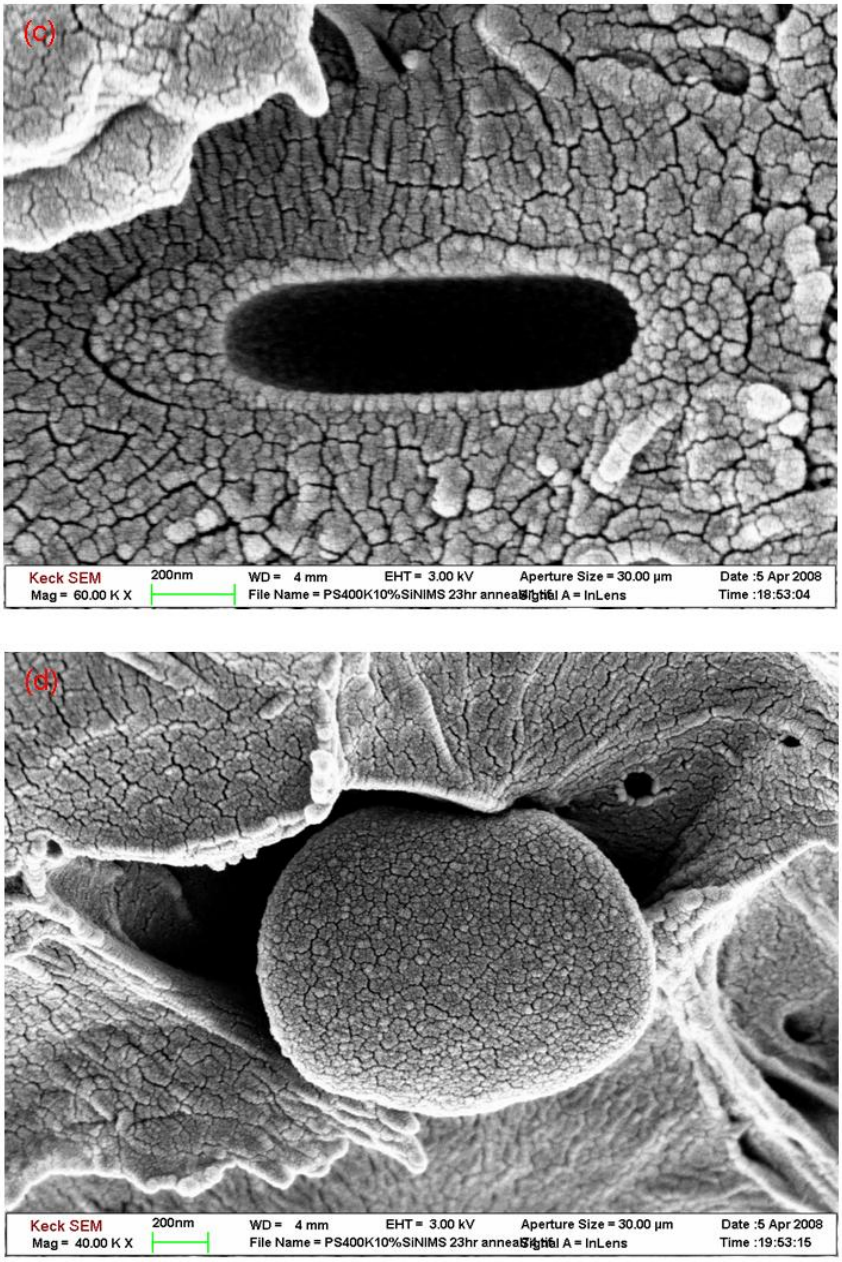

Figure 3.19(c)(d) SEM images of PS400k+10 wt. % (HS30-SIT-M2070), after 23hr annealing (cross-section)

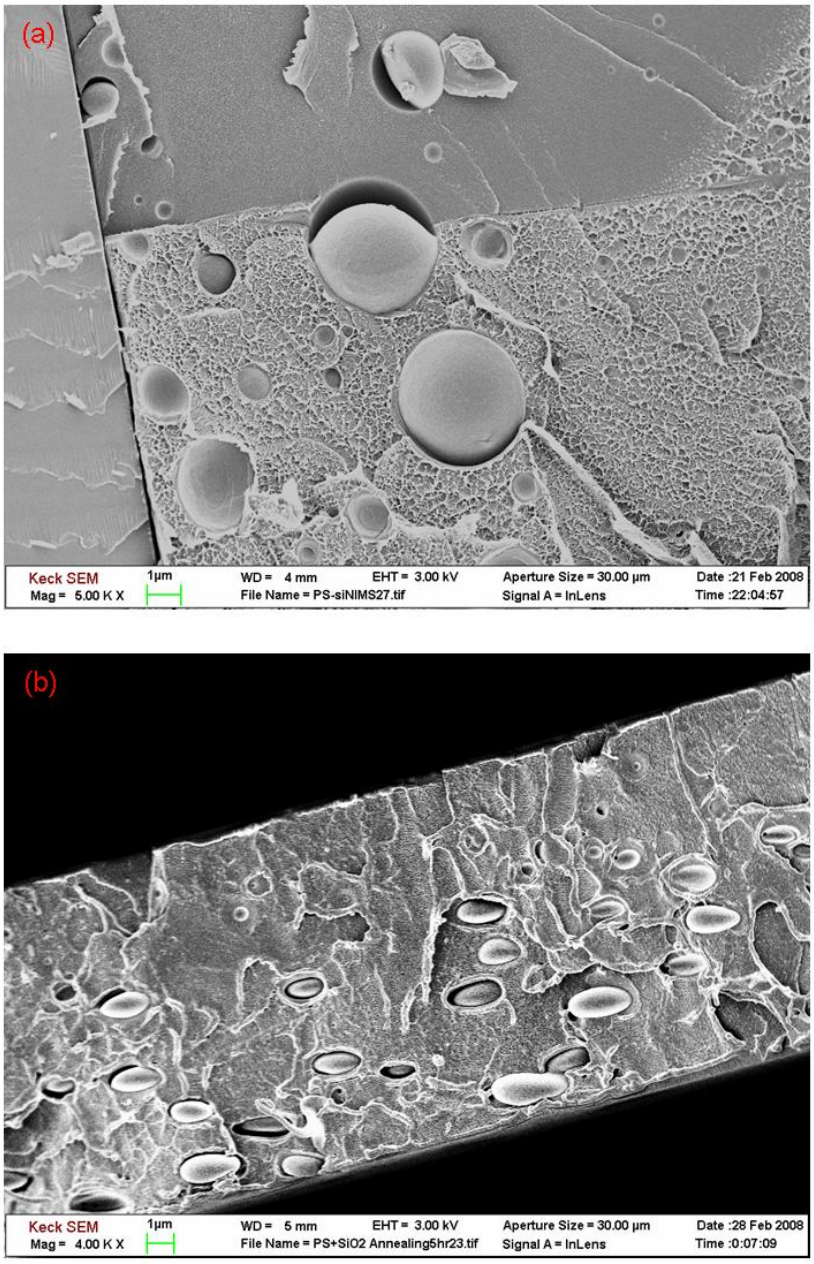

Figure 3.20 SEM images of PS+(HS30-SIT-M2070) composites, based on different molecular weights (a) MW = 65k, (b) MW = 123k

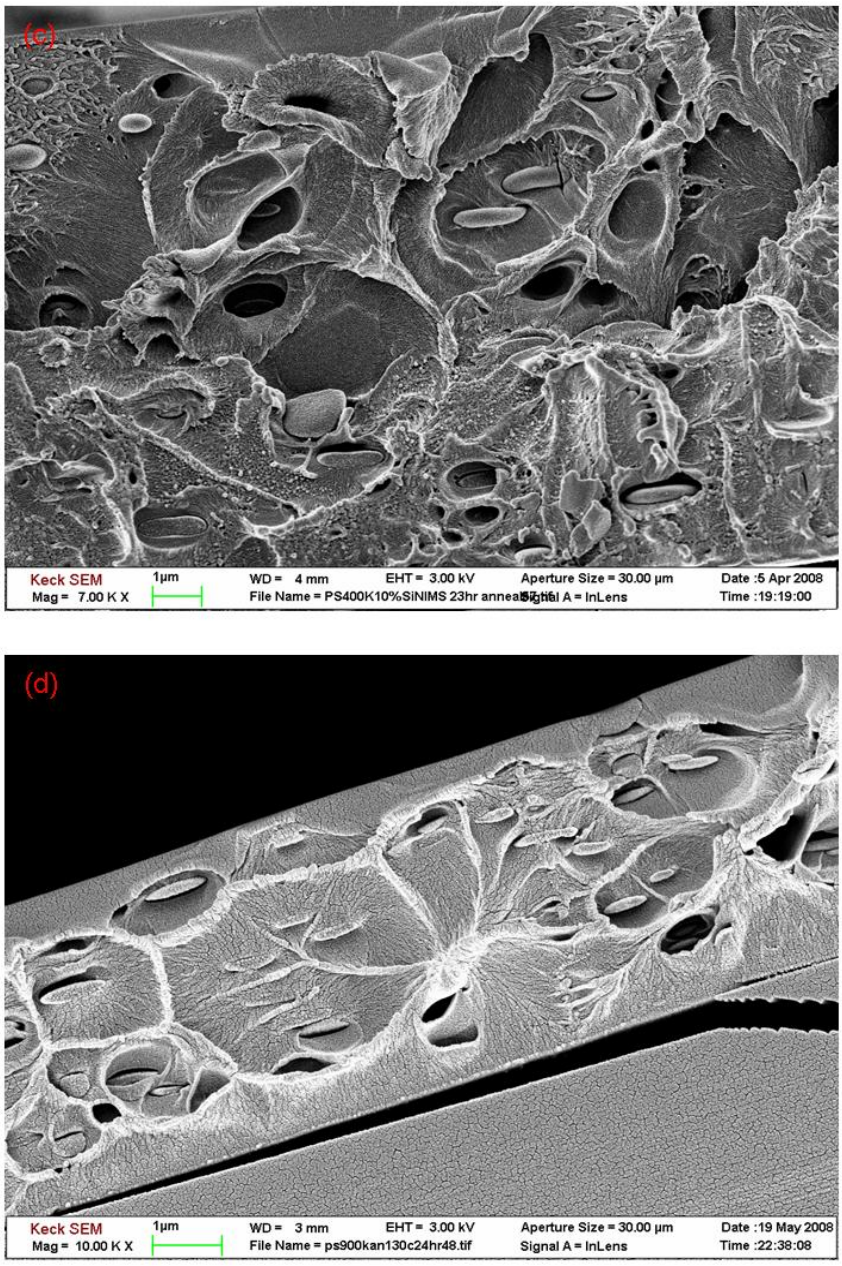

Figure 3.20 SEM images of PS+(HS30-SIT-M2070) composites, based on different molecular weights (c) MW = 400k, (d) MW = 900k.

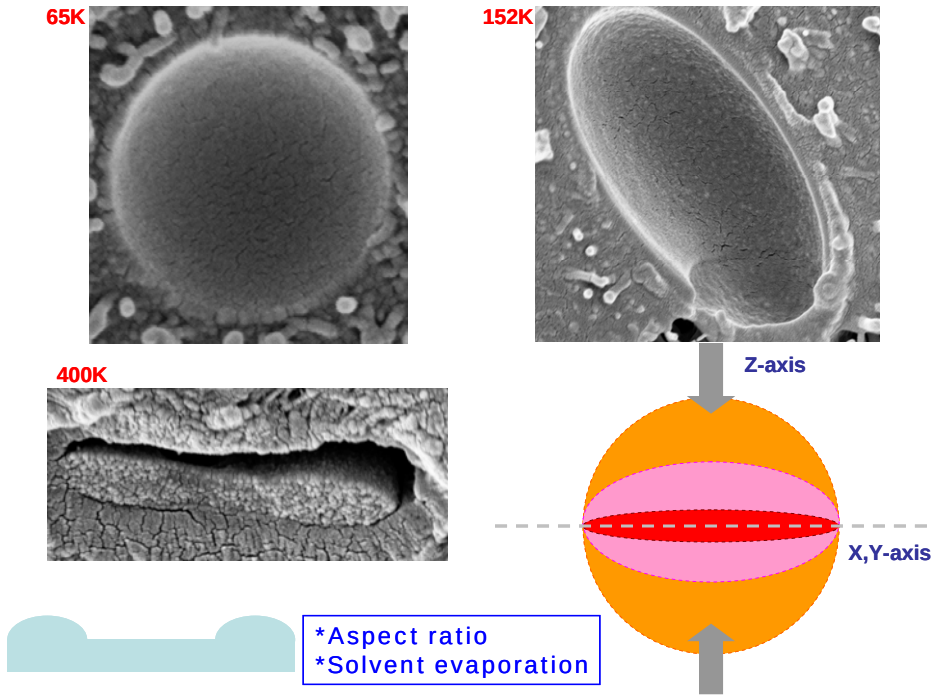

Figure 3.21 SEM images of PS+(HS30-SIT-M2070) composites, based on different molecular weights (a) MW = 65k, (b) MW = 152k, (c) MW = 400k

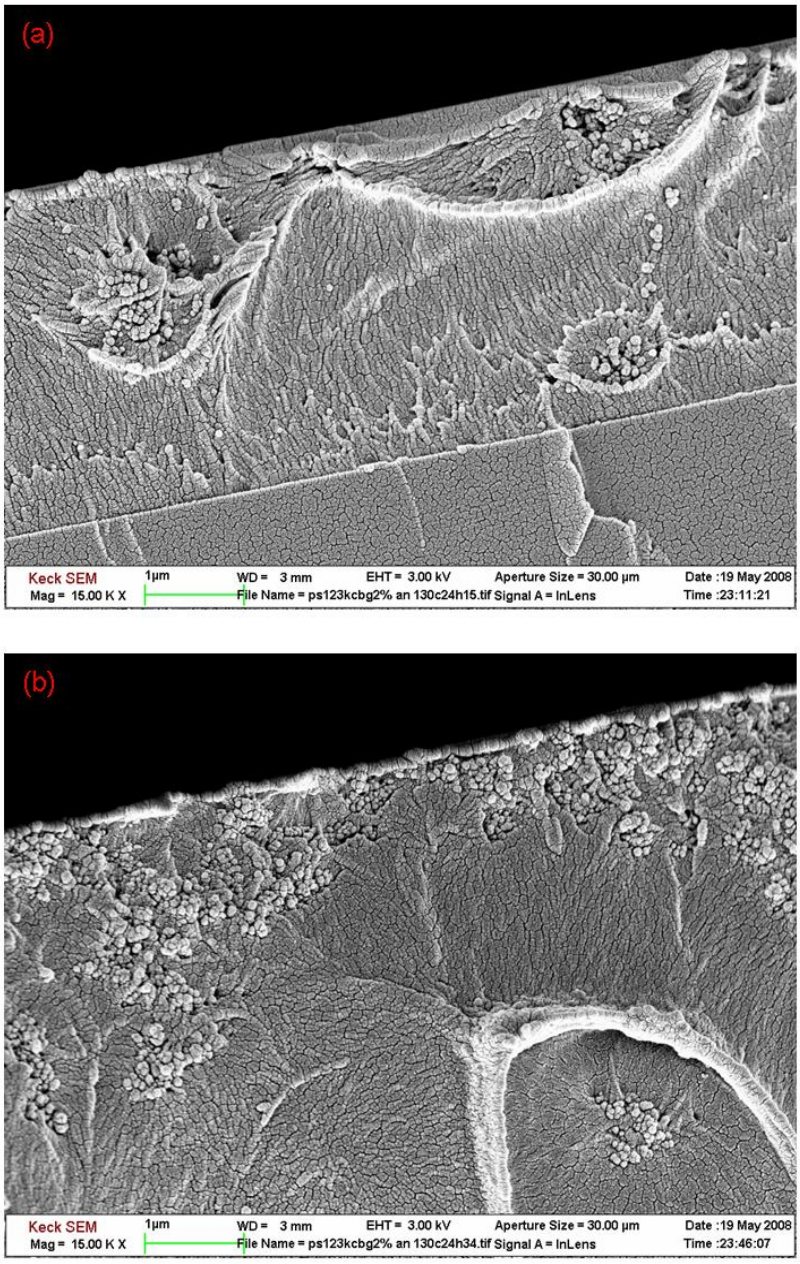

Figure 3.22(a)(b) SEM images of PS123k+2 wt. % CBg-M2070 after annealing

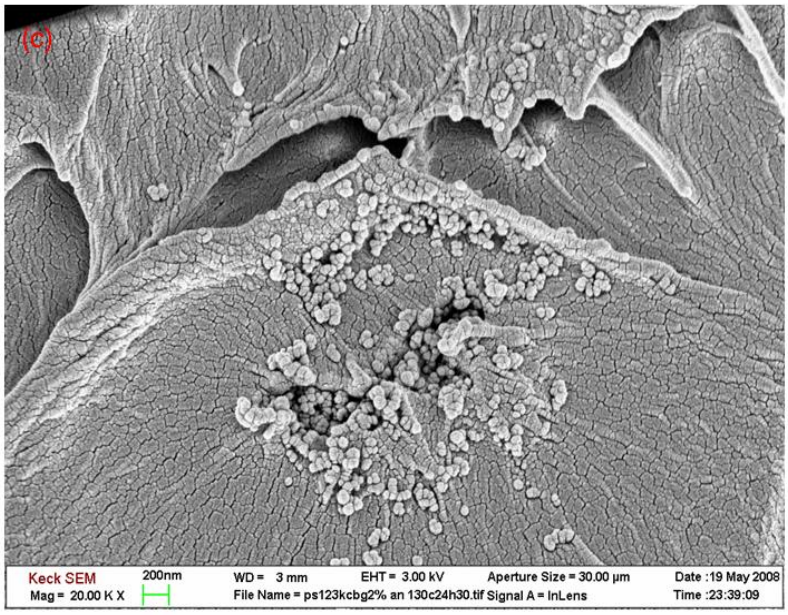

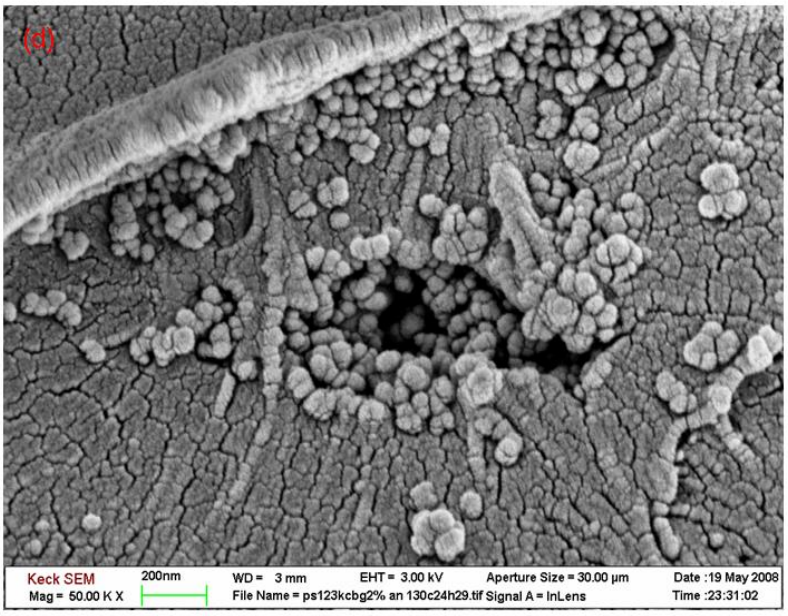

Figure 3.22(c)(d) SEM images of PS123k+2 wt. % CBg-M2070 after annealing

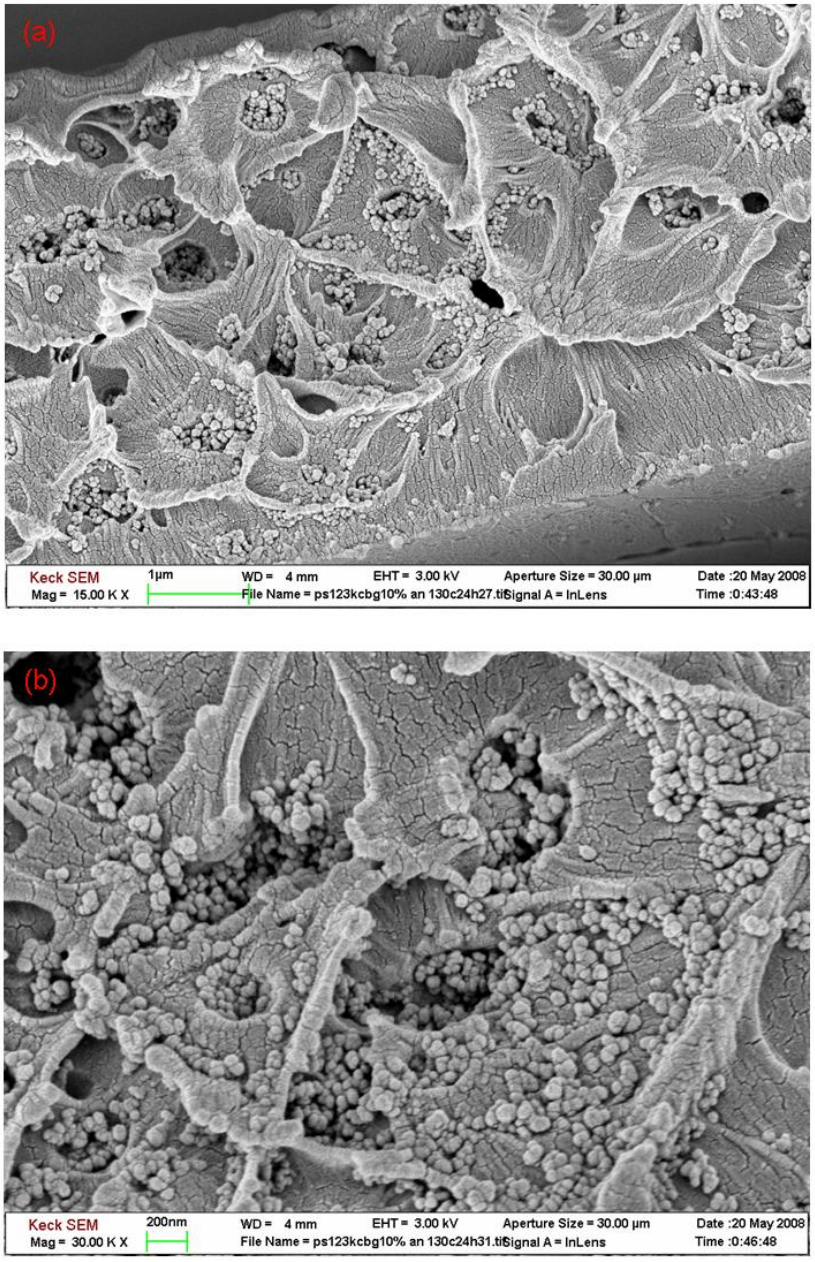

Figure 3.23(a)(b) SEM images of PS123k+2 wt. % CBg-M2070 after annealing

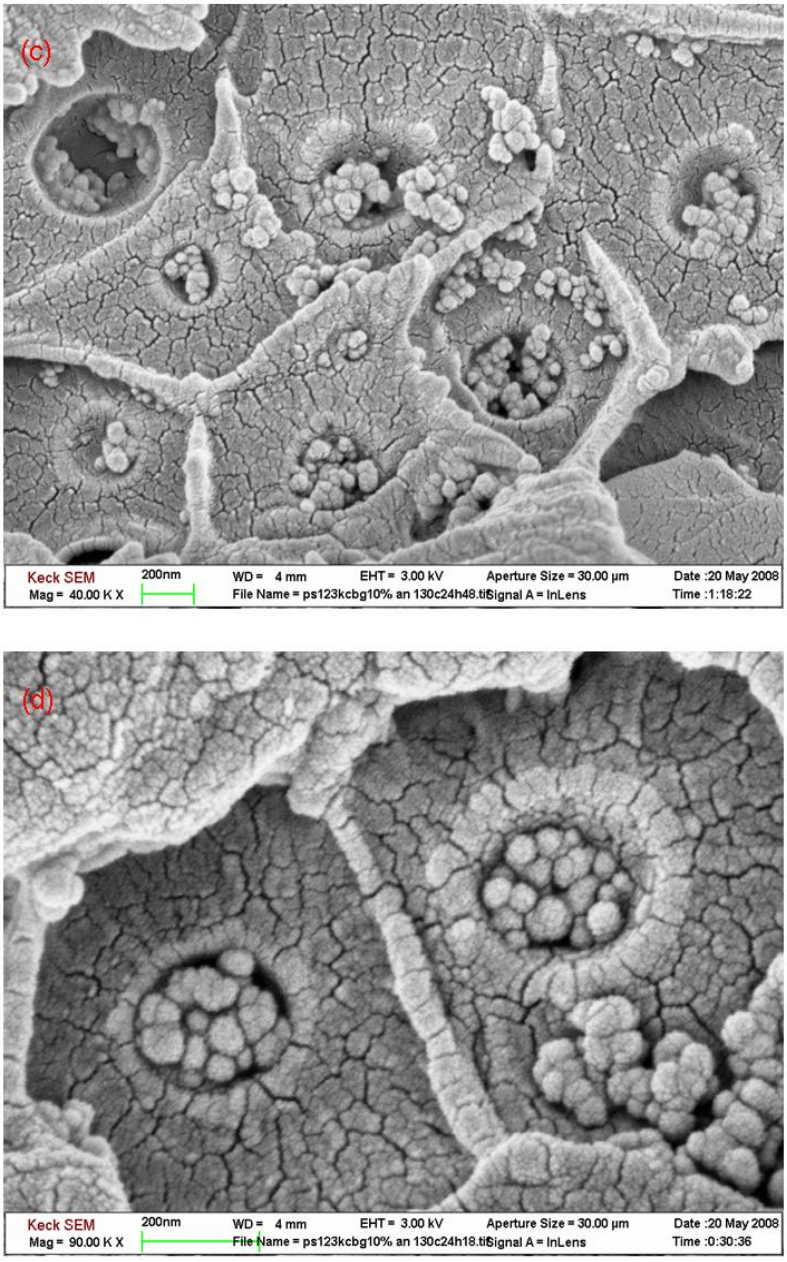

Figure 3.23(c)(d) SEM images of PS123k+2 wt. % CBg-M2070 after annealing

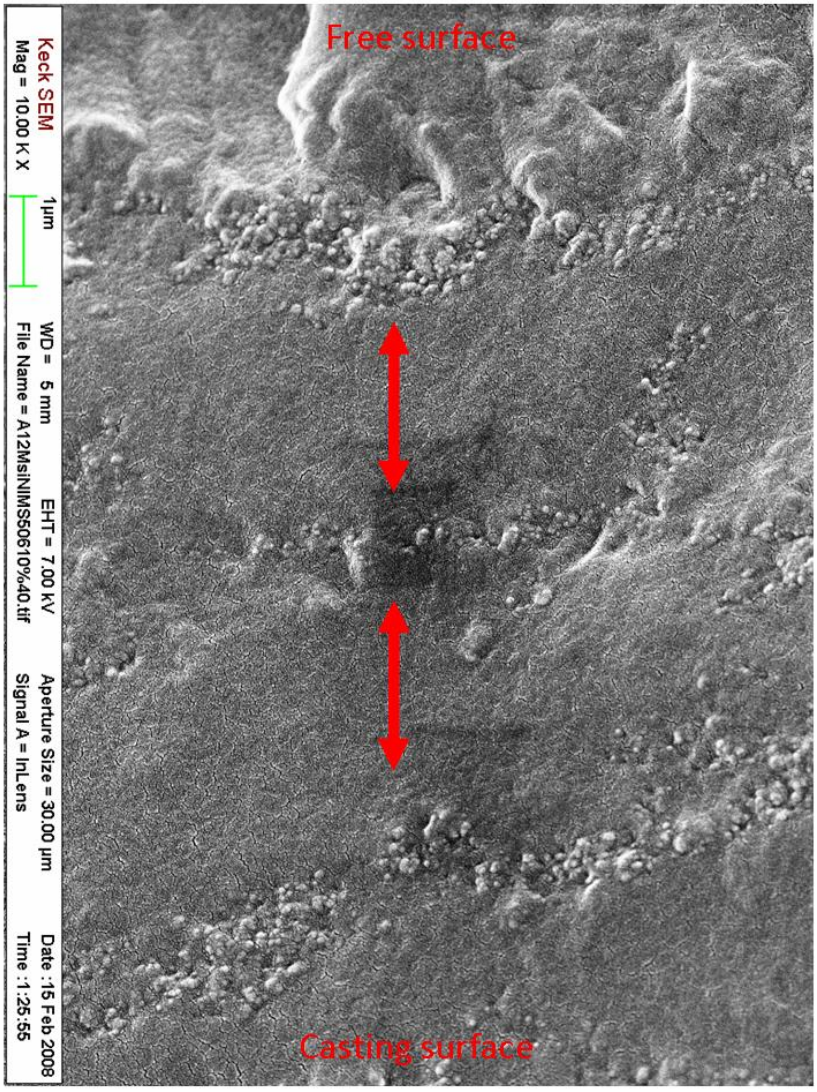

Figure 3.24 SEM image of PDMS + 10wt. % (HS30-SIT-M2070) after annealing

3.2.4 AFM Measurements

AFM images of (HS30-SIT-M2070)-PS composites (Fig. 3.26) and (HS30-SIT-M2070) nanoparticles (Fig. 3.25) demonstrated that, during annealing, the nanoparticles tend to migrate away from the surface to the bulk matrix. Eventually, the composites show no evidence for nanoparticles and their hydrophilic characteristics at the surface. The features from AFM were slightly different from the SEM measurement because the samples used for AFM were made from spin-coating, and the samples used for SEM were made from solvent-casting. Based on the two different processes, film thickness differed sharply (50 and 2000 nm for the spin-coated and solvent casted samples respectively).

In spin-coating, all sub-micro aggregates were surrounded by smaller aggregates. This result implies a possible mechanism: initially, individual small particles assemble into bigger particles at the surface and then diffuse into the bulk. Therefore, even at the same concentration, 200nm micelle-like spheres could not be clearly distinguished with the polymer matrix. We also analyzed the geometry of these polydispersed aggregates and determined that the disk-like geometry corresponded to high MWs of the polymer matrix.

The images in figure 3.27 showed that the nanoparticles in the low molecular weight (HS30-SIT-M2070)-PS composite still tend to diffuse away from the surface after sufficient annealing. Before annealing, these non-equilibrium assemblies had a clear spherical geometry with the polymer matrix, which differed from the high MW system (Fig. 26). The molecular weight of the polymer matrices was one of the important factors for formation of the aggregation.

In addition to PS, we used polyethylene glycol (PEG) as an additional polymer system. PEG was expected to be more compatible with polyetheramine-modified nanoparticles than the polystyrene matrix. Of particular importance is PEG's low glass

transition temperature. Because of PEG's lower Tg (PEG20k, Tg = -34.6^{o}C), the particle mobility would be very differenet compared to PS (Tg~100 ^{o}C).

The images in figure 3.28 are spin-coated surfaces of neat polyethylene glycol. There are several ways to manipulate the PEG film morphology, which include the concentration of the PEG solution, the temperature of PEO film formation, as well as the process of deposition onto the substrate. The crystalline features of PEG (a semi-crystalline polymer) have been already studied [11-13].

The images of (HS30-SIT-M2070)-PEO composites in figures 3.29 and 3.30 demonstrate different behavior compared with that of (HS30-SIT-M2070)-PS composites. During annealing, the nanoparticles tend to migrate from the bulk to the surface without forming significant aggregates within the polymer matrix. In the composite with a higher concentration of nanofillers (10wt. %), it was difficult to distinguish the particle migration because of the saturated surface. The original crystalline-like morphology of PEO was disturbed because of the presence of nanoparticles. When the composites had lower concentration of nanofillers (2wt. %), the crystalline-like morphology could be preserved to a certain degree at this concentration of nanoparticles.

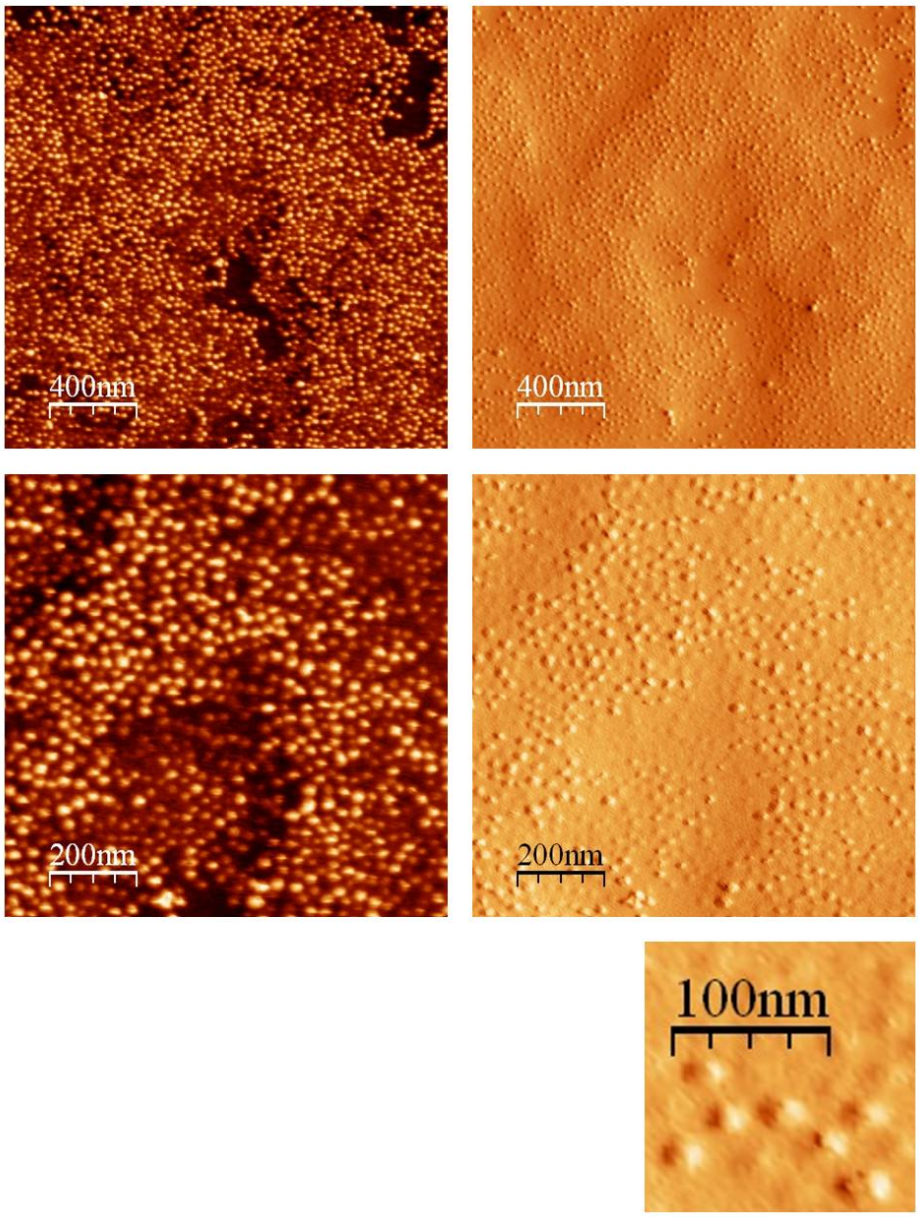

Figure 3.25 AFM images of neat (HS30-SIT-M2070) deposited on Si wafer

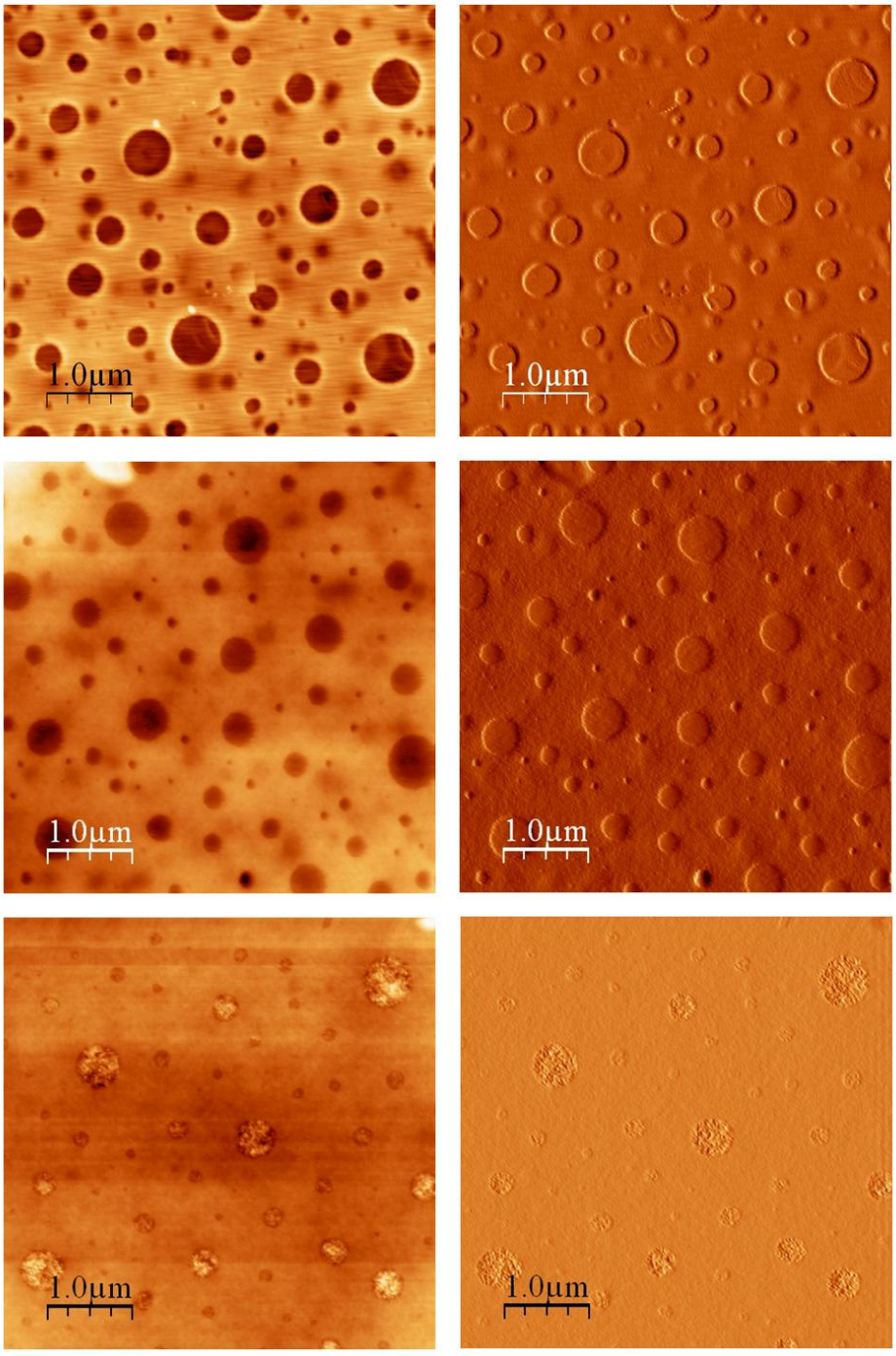

Figure 3.26 AFM images of PS400k + 10 wt. % (HS30-SIT-M2070), during annealing; Height (left) and Amplitude (right); Before, at 30min and at 23 hr (from top to bottom).

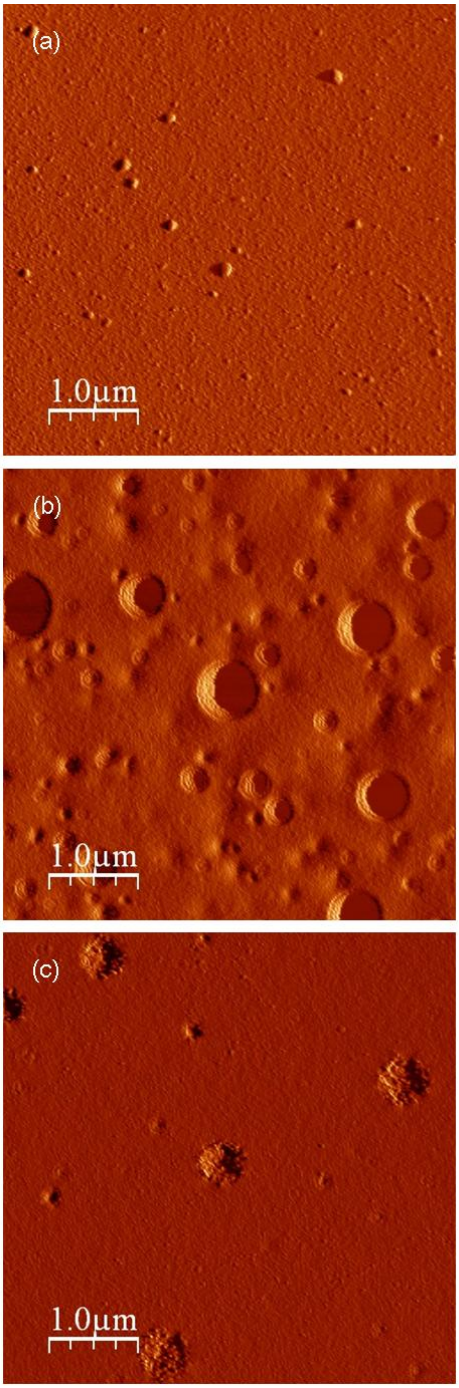

Figure 3.27 AFM images of neat PS (65k) (top); PS65k + 10 wt. % (HS30-SIT-M2070) before (middle) and 23 hr annealing (bottom).

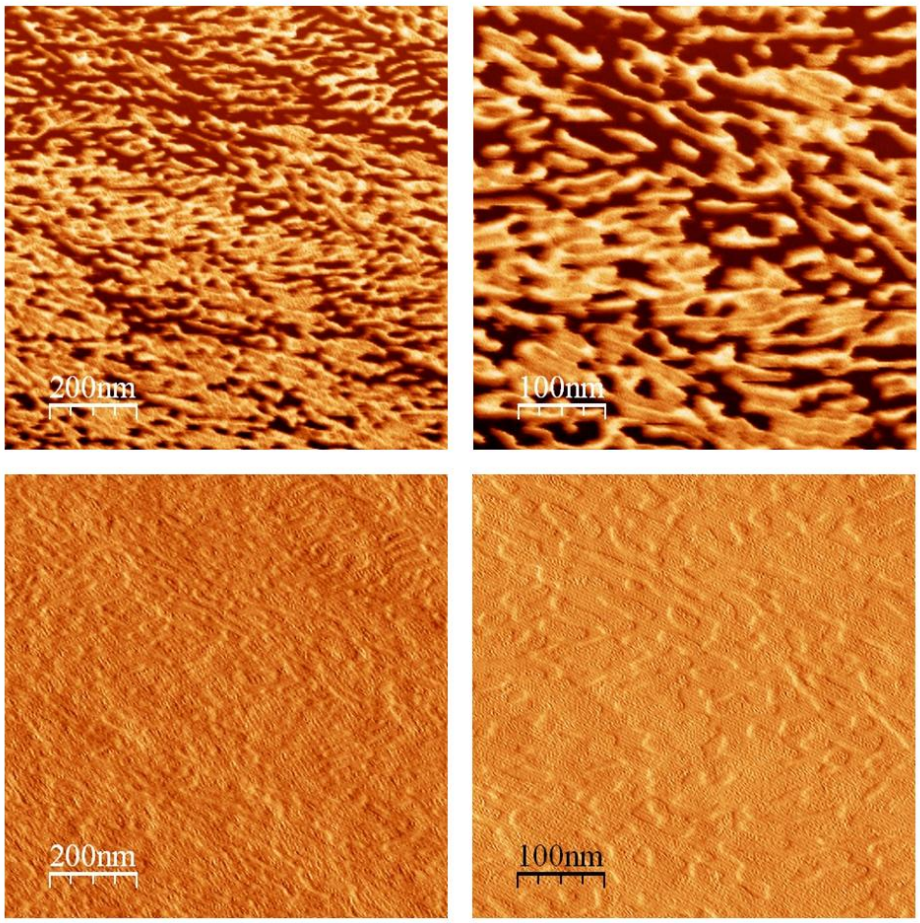

Figure 3.28 AFM images of neat PEG (20k) deposited on Si wafer.

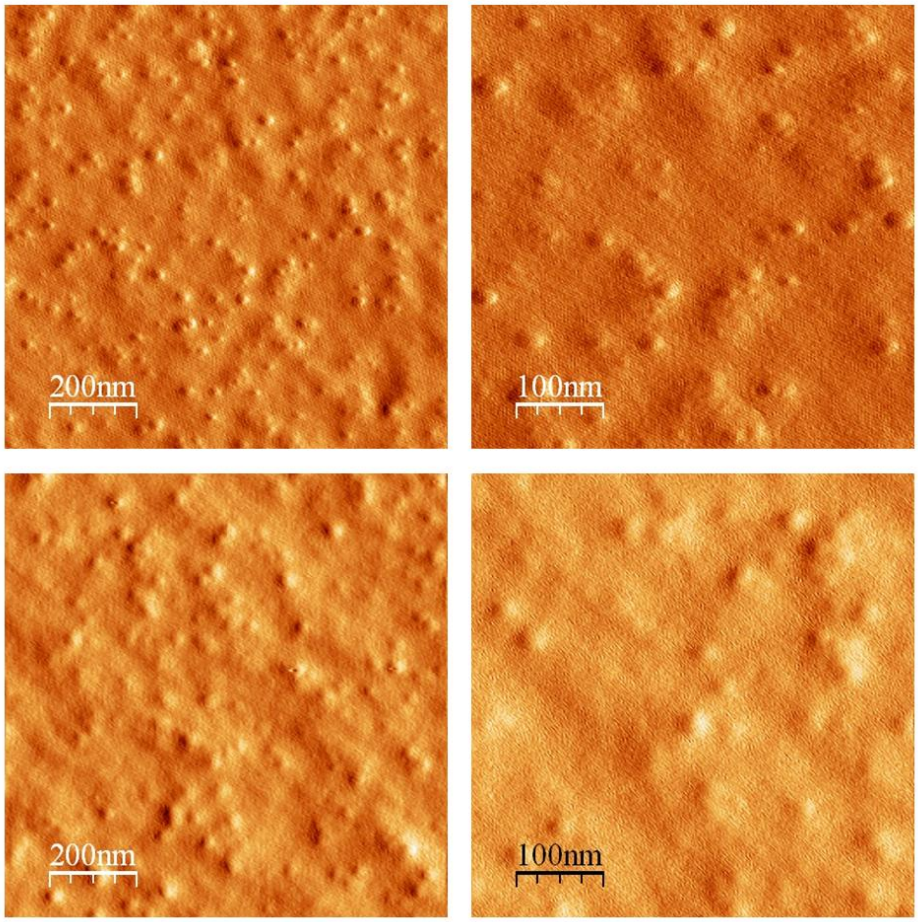

Figure 3.29 AFM images of PEG20k + 10 wt. % (HS30-SIT-M2070); before (top), after annealing (bottom)

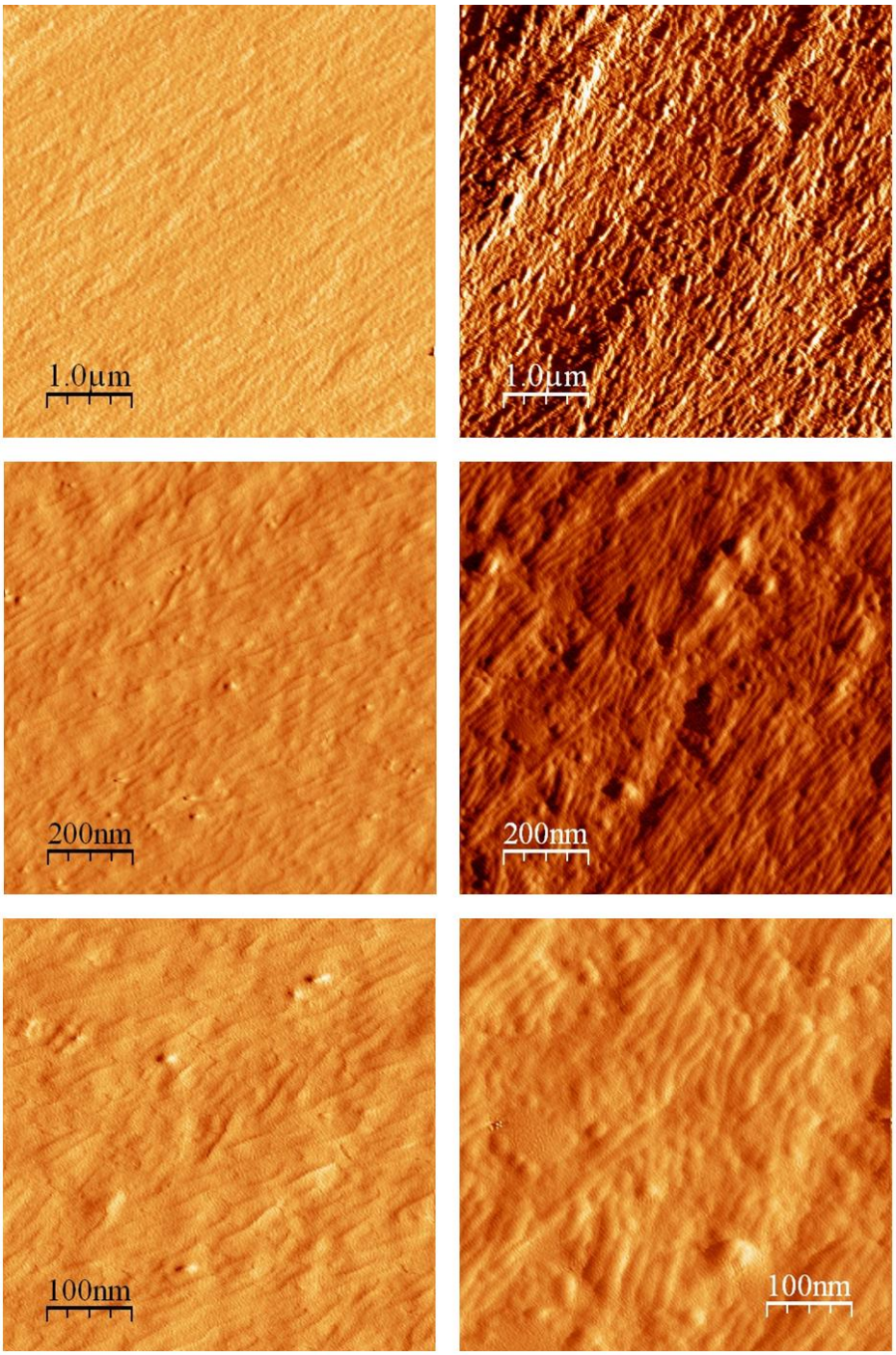

Figure 3.30 AFM images of PEG20k + 2 wt. % (HS30-SIT-M2070); before (left), after annealing (right)

3.2.5 XPS Measurements

X-ray photoelectron spectroscopy (XPS) was used to investigate the tendency of nanoparticles to reach the surface without self-aggregation in (HS30-SIT-M2070)-PEG systems. Before annealing, no silicon was present on the surface in the sample containing 2 wt.% nanoparticles (Fig. 3.31). When the loading was increased to 5 wt. %, the surface concentration of Si is 5 at. % (Fig. 3.32). At both concentrations, the amount of Si increases after annealing consistent with the migration of these hybrid nanoparticles. They prefer diffusing to interfacing with a higher free surface energy.

At long annealing times (50°C, up to 24 hr), the intensity of silicon declined because of the dewetting on the wafer substrate.

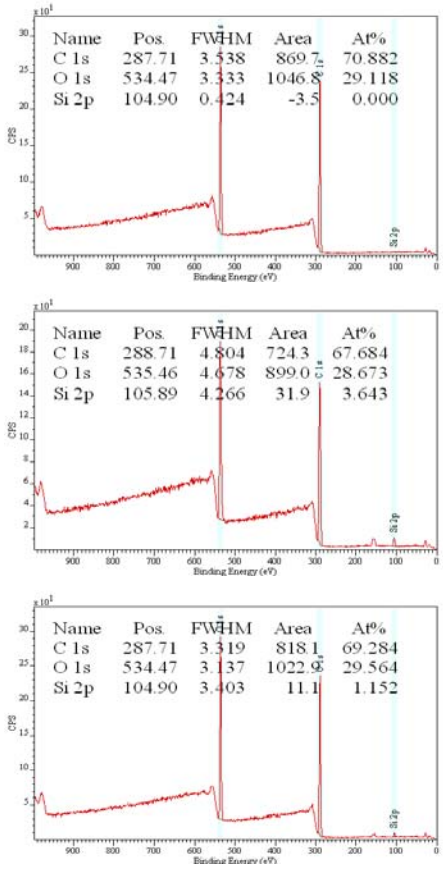

Figure 3.31 XPS measurements of 2 wt. % (HS30-SIT-M2070)-PEO, 50°C annealing; before (top), 4hr (middle), and 24hr (bottom).

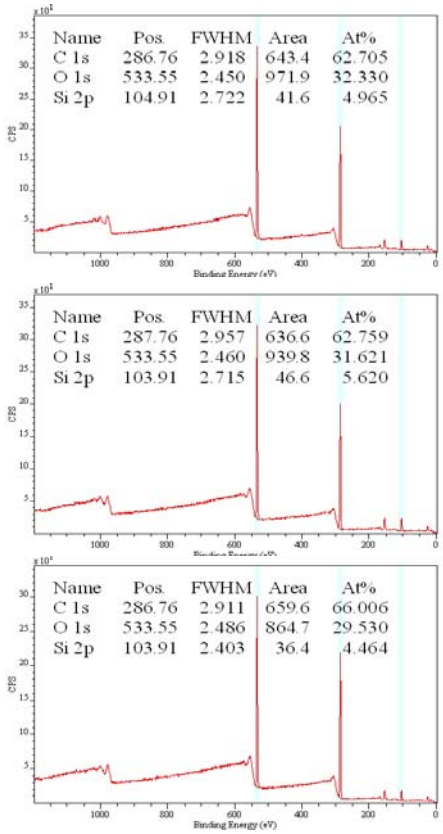

Figure 3.32 XPS measurements of 5 wt. % (HS30-SIT-M2070)-PEO, 50°C annealing; before (top), 4hr (middle), and 24hr (bottom).

3.3 Summary

We developed a new series of liquid-like nanoparticles and corresponding nanocomposites and explored possible polymer-particle interaction mechanisms by considering a variety of core materials (silica-based and carbon black-based) and a range of polymer matrices (polystyrene, polyethylene glycol, and PDMS-polyurea copolymer). By tailoring the polarity and surface tension between particle-particle and particle-polymer, it is possible to control the geometry, size, and dispersion state of the nanoparticles.

REFERENCES

1. Ashley, K. M.; Meredith, J. C.; Amis, E.; Karim, A.; *Polymer*, ***2003***, 44, 769-772
2. Bonaccurso, E.; Butt, H. J.; Spiess, H. W.; *Langmuir*, ***2002***, 18, 8056-8061
3. Elender, G.; Sackmann, E.; *J. Phys. France*, ***1994***, 4, 455-479
4. Choi, S. H.; Zhang, B. M.; *Langmuir*, ***2003***, 19, 1419-1428
5. Suh, K. Y.; Park, J. H.; Lee, H. H.; *Journal of Chemical Physcis*, ***2002***, 116, 7714-7718
6. Meyer, E.; Braun, H. G.; *Macromol. Mater. Eng*., ***2000***, 276, 44–50
7. Kargupta, K.; Sharma, A.; *Physical Review Letters*, ***2001***, 86, 4536-4539
8. Shiloach, A.; Blankschtein, D.; *Langmuir*, ***1998***, 14, 7166-7182
9. Lin, Z.; *Langmuir*, ***1996***, 12, 1729-1737
10. Lin, J. J.; Young, M. Y.; Shau, S. M.; Cheng, I. J.; *Polymer*, ***2000***, 41, 2405-2417
11. Lin, J. J.; Cheng, I. J.; Kwan, C. C.; *Ind. Eng. Chem. Res*., ***2000***, 39, 65-71
12. Yang, C.; Rathman, J. F.; *Polymer*, ***1996***, 37, 4621-4627
13. Wasan, D. T.; Ginn, M. E.; Shah, D. O.; *Surfactants in Chemicalflrocess Engineering*, 1998, 1
14. Nagarajan, R.; Koczo, K.; Wasan, D. T.; *AIChE Journal*, ***1995***, 41, 915-923
15. Campanelli, J. R.; Wang, X.; *Journal of Colloid and Interface Science*, ***1999***, 213, 340–351
16. Hunsel, J. V.; Joos, P.; *Colloid Polym Sci*, ***1989***, 267, 1026-1035
17. Freud, B. B.; Harkins, W. D.; *J. Phys. Chem*., ***1929***, 33, 1217-1234
18. Wrolstad, R. E.; Acree, T. E.; *Current Protocols in Food Analytical Chemistry, Static and Dynamic Interfacial Tension Analysis*, D3.6
19. Misak, M. D.; *Journal of Colloid and Interface Science*, ***1968***, 27, 141-142
20. Patist, A.; Shah, D. O.; *Journal of Surfactants and Detergents*, ***2000***, 3, 53-58

21. Chakarov, V.; *Colloid & Polymer Sci*., ***1983***, 261,452-457

22. Yeung, A.; Dabros, T.; Masliyah, J.; Journal of Colloid and Interface science, 1998, 208, 241-247

23. Jan, J. Z.; Huang, B. H.; Lin, J. J.; *Polymer*, ***2003***, 44, 1003-1011

24. Lee, W. B.; Oh, Y.; Lee, H.; *Synthetic Metals*, ***2001***, 117, 305-306

25. Delorme, N. ; Bardeau, J. F. ; Poncin-Epaillard, F. ; *Thin Solid Films*, ***2006***, 496, 612 – 618

26. Kim, J. Y.; Park, Y. H.; Kim, J. S.; Jeong, Y. T.; *J. Ind. Eng. Chem*., ***2007***, 13, 1023-1028

27. Gu, D.; Sistiabudi, R.; Dey, S. K.; *Jounral of Applied Physics*, ***2005***, 97, 123710-123715

28. Luzinov, I.; Julthongpiput, D.; Tsukruk, V. V.; *Langmuir*, ***2000***, 16, 504-516

29. Fadeev, A. Y.; McCarthy, T. J.; *Langmuir*, ***2000***, 16, 7268-7274

30. Lee, Y. H.; *Langmuir*, ***1999***, 15, 1796-1801

31. Weikart, C. M.; Miyama, M.; Yasuda, H. K.; *Langmuir*, ***2000***, 16, 5169-5177

32. Miyama, M.; Yang, Y.; Yasuda, H. K.; *Langmuir*, ***1997***, 13, 5494-5503

33. Yaminsky, V. V.; Thuresson, K.; Ninham, B. W.; *Langmuir*, ***1999***, 15, 3683-3688

34. Uilk, J. M.; Mera, A. E.; Wynne, K. J.; *Macromolecules*, ***2003***, 36, 3689-3694

35. Meijer, M.; Haemers, S.; Militz, H.; *Langmuir*, ***2000***, 16, 9352-9359

36. Miyama, M.; Yasuda, H. K.; *Langmuir*, ***1998***, 14, 960-964

37. Pellerite, M. J.; Wood, E. J.; Jones, V. W.; *J. Phys. Chem. B*, ***2002***, 106, 4746-4754

38. Lee, D.; Rubner, M. F.; Cohen, R. E.; *Nano Lett*., ***2006***, 6, 2305-2312

39. Lee, D.; Gemici, Z.; Cohen, R. E.; *Langmuir*, ***2007***, 23, 8833-8837

40. Gemici, Z.; Shimomura, H.; Cohen, R. E.; Rubner, M. F.; *Langmuir*, ***2008***, 24, 2168-2177

41. Lee, D.; Omolade, D.; Cohen, R. E.; Rubner, M. F.; *Chem. Mater*., ***2007***, 19, 1427-1433

42. Zhao, L. Y.; Eldridge, K. R.; Leung, K. T.; Applied Physics Letters, 2006, 88, 033111-4

43. Paul, S.; Pearson, C.; Tsoukalas, D.; Petty, M. C.; *Nano Letters*, ***2003***, 3, 533-536

44. Fan, H.; Wright, A.; Jiang, Y. B.; *Adv. Funct. Mater*., ***2006***, 16, 891–895

45. Boontongkong, Y.; Cohen, R. E.; *Macromolecules*, ***2002***, 35, 3647-3652

46. Iler, R. K.; *Journal of Colloid and Interface Science*, ***1966***, 21, 569-594

47. Decher, G.; *Science*, ***1997***, 277, 1232-1237

48. Bansal, A.; Yang, H.; Li, C.; Benicewicz, B. C.; Kumar, S. K.; Schadler, L. S.; *Journal of Polymer Science: Part B: Polymer Physics*, ***2006***, 44, 2944–2950

49. Bansal, A.; Yang, H.; Li, C.; Benicewicz, B. C.; *Nature Materials*, ***2005***, 4, 693-698

50. Jo, H.; Blum, F. D.; *Chem. Mater*., ***1999***, 11, 2548-2553

51. Stange, T. G.; Evans, D. F.; Hendrickson, W. A.; *Langmuir*, ***1997***, 13, 4459-4465

52. Barnes, K. A.; Karim, A.; Gruell, H.; Amis, E. J.; *Macromolecules*, ***2000***, 33, 4177-4185

CHAPTER 4

ADVANCED APPLICATIONS

4.1 Lead-salt quantum-dot ionic liquids

4.1.1 Introduction

Due to their size-tunable absorption spectra and possible multiple-exciton-generation (MEG) mechanism, lead-salt (PbS, PbSe, and PbTe) quantum dots (QDs) are a good candidate material for photovoltaic devices [1]. They are also efficient infrared (IR) emitters, and have been used for biomedical imaging [2] and fabrication of electroluminescent devices [3]. They could also serve as a good candidate for saturable absorbing materials in IR fiber optics [4,5]. Despite their promise, the stability (e.g., photo-stability) and compatibility of the QDs have prevented them from realizing their full potential. Surface passivation and functionalization are the typical solutions. Among the different functionalization methods, the use of ionic liquids to passivate QD surface is attracting increasing attention in the research community [6-11]. Using certain ionic liquid ligands, solid materials (semiconductor or metal) can be transferred to a new state that exhibits liquid-like behavior at room temperature [12,13]. In this report, we demonstrate a simple route to synthesize ionic liquids consisting of lead-salt QDs. We demonstrate the method using PbS as a model system.

4.1.2 Experiment Section

Colloidal PbS QDs were synthesized using organometallic precursors [14,15]. Ionic liquid ligands were synthesized by protonating sodium 3-mercapto-1-propanesulfonate followed by neutralization with polyetheramine as described in chapter two.

The resulting QD ionic liquid is a viscous, brown fluid, as shown in Figure 4.1b. The fluidity of the material is affected by both the electrostatic force and the van der Waals force among the ions (shown in Figure 4.1a). By carefully tuning the size of the ions, the fluidity can be varied at fixed temperature. [14] In other words, the glass transition temperature Tg of the material can be changed by tuning the size of the ions. A transmission electron microscopy (TEM) image of a PbS QD ionic liquid is shown in Figure 81c. The dark parts distinguished from the light color background are the PbS QD ionic liquid. The small clusters (~ 50 nm) observed in the TEM image actually include several QDs. As shown in the inset of Figure 4.1c, the QD cores (black) are wrapped by ionic-liquid ligands (grey) and form a cluster.

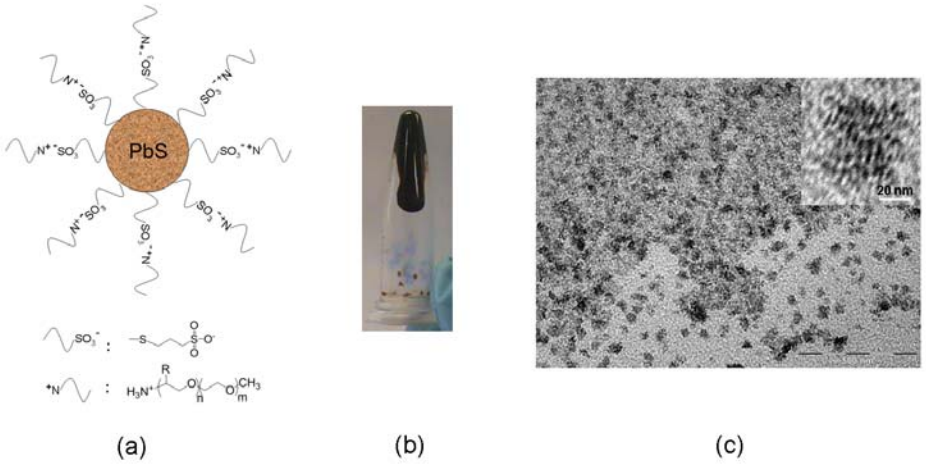

Figure 4.1 (a) Schematic of an ionically modified QD. (b) A photograph of a PbS QD ionic liquid. (c) TEM image of a PbS QD ionic liquid. Inset, a cluster of QD ionic liquid.

4.1.3 Results and Discussion

The amphiphilic nature of the PbS QD ionic liquid was demonstrated using contact angle measurements. As shown in Figure 4.2a, the contact angle of PbS QD

ionic liquid on a silicon wafer is about 12^0, which is much less than the contact angle (58^0) of water on the same substrate. The low contact angle indicates that the PbS QD ionic liquid wets easily a hydrophilic substrate. On a Teflon film, the PbS QD ionic liquid shows a contact angle of 40^0, while the contact angle of water on the same substrate is about 106^0. Thus the PbS QD ionic liquid wets reasonably well both a hydrophilic and a hydrophobic substrate suggesting that it is indeed amphiphilic.

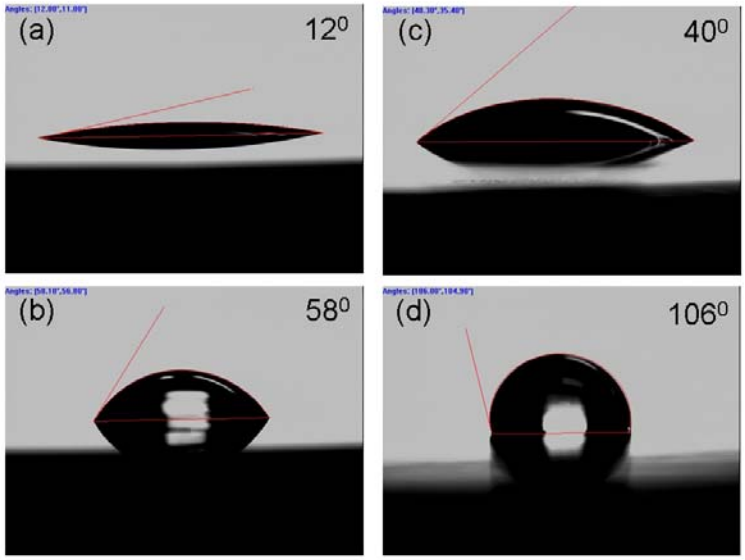

Figure 4.2 Contact angle of PbS QD ionic liquid on a silicon wafer (a) and on a Teflon film (c); contact angle of water on a silicon wafer (b) and on a Teflon film (d).

Both the ionic liquid used for surface functionalization and the QD ionic liquid are conductive, though their conductivity is low. The time and frequency dependent conductivity for each material was measured. At temperatures below Tg – glass transition temperature (measured by differential scanning calorimetry (DSC), the dependence of the conductivity on frequency (insets of Fig. 4.3a and b) follows power law $\sigma(\omega) \propto \omega n$ ($n \sim 1$ in our experiment). This kind of dependence has been observed

among a wide range of solids [15], and is explained in terms of many-body interaction [15,16]. Above Tg, the higher fluidity of the materials contributes to the conductivity [17]. At low frequencies, the conductivity is flat (DC conductivity). The dispersion of the conductivity takes place at certain frequencies which depend on the temperature. This dependence has also been observed in other ionic materials [17,18], and was recently modeled by Funke et al. using linear response theory [18]. In contrast to the frequency independent conductivity at low frequencies of the pure ionic liquid, the conductivity of QD ionic liquid has more features (Fig. 4.3b) and its overall conductivity is about an order of magnitude lower. The lower conductivity is probably because the heavy QD cores reduce the fluidity of the fluid as well as reduce the mobility of the ligands, since they are bonded to the QDs. The decrease of the conductivity of the QD ionic liquid can also be clearly seen in the plot of temperature dependent conductivity, as shown in Figure 4.3c. Unlike the pure ionic liquid whose conductivity-temperature relation follows the Vogel-Tammann-Fulcher (VTF) model [19], the QD ionic liquid exhibits more features at temperatures above the Tg. Further studies are underway to elucidate the conductivity of these systems in more detail.

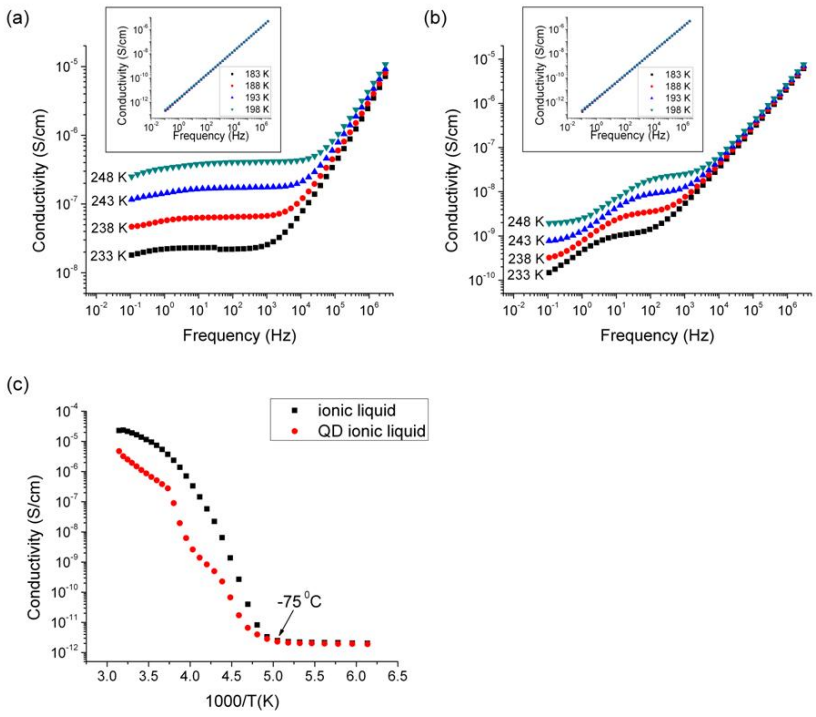

Figure 4.3 Freqeuncy-dependent conductivity of ionic liquid (a) and QD ionic liquid (b) at different temperatures above Tg and below Tg (insets). (c) Temperature-dependent conductivity of ionic liquid (solid square) and QD ionic liquid (dot), measured at frequency of 1 Hz.

To investigate the optical properties of PbS QDs ionic liquid, optical absorption and photoluminescence (PL) were measured and compared with those of the original QDs in toluene. As shown in Figure 4.4a, both the lowest energy absorption peak and PL emission peak were red-shifted relative to those from the original QDs, as observed previously with different thiol ligands [20, 21].

The relative PL efficiency (PL intensity normalized to absorption) of ionic QDs was measured by sandwiching a thin layer (~ 10 μm) of the liquid in between two cover glass slides. As comparison, the PL efficiency of the original QD in toluene and

a thin PbS QD film were measured in the same way. As shown in Figure 4.4b, the PL efficiency of QD ionic liquid is between that of the original QDs in toluene and the QD film. A small peak at around 1300 nm appears in the spectrum of the QD ionic liquid, which might be caused by small clusters of QDs formed in the QD ionic liquid, as observed in the TEM image. Since formation of small clusters reduces the PL efficiency, there is the potential that the efficiency of PL form QD ionic liquids could be improved, if cluster formation could be prevented during synthesis.

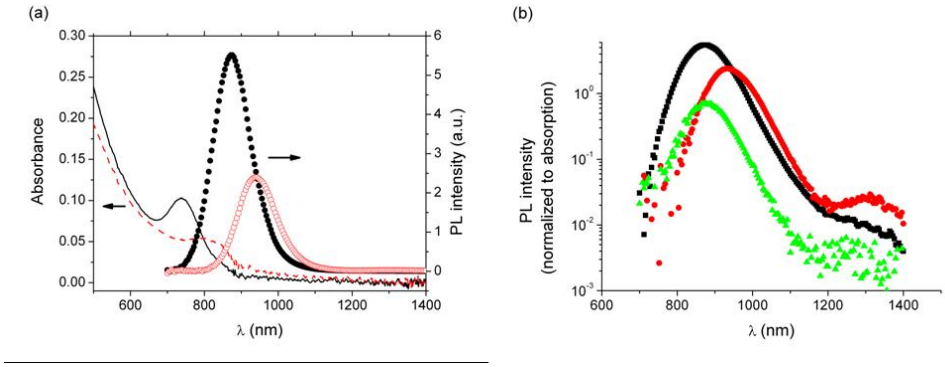

Figure 4.4 (a) PL and absorption spectra of PbS QDs in toluene (solid dots and line) and PbS ionic liquid (open circles and dash line). (b) PL intensity of PbS QDs in toluene (solid squares), PbS QD ionic liquid (solid circles) and PbS QD film (solid triangles).

The photo-stability of the PbS QD ionic liquid was measured by shining a red laser (4 mW, 632 nm) onto the sample, while the PbS QDs in toluene were used as the control. The PL from the PbS QDs in toluene decreased fast in the first few seconds, and then slowly decreased in the following 20 minutes (Fig. 4.5a). The fast decrease is thought to be caused by the photo-excited charge trapping in the QDs [22], while the slow decrease is attributed to the photo-oxidation of the QDs [22]. The photo-oxidation causes a blue-shift in the PL spectra, which was also observed in our

experiment as shown in Figure 4.5b. In contrast, there is virtually no change in the PL intensity of the PbS QD ionic liquid (Fig. 4.5a). The PL spectra of PbS QD ionic liquid before and after laser exposure were almost identical, indicating no photo-oxidation. An even longer time-dependent PL was measured for PbS QD ionic liquid, which shows less than 10% degradation after about an hour laser shining. The stability of PL from the QD ionic liquid demonstrates good passivation of PbS QD surface which reduces charge trapping. The ionic nature of the system may reduce oxygen exposure, protecting the QDs from photo-oxidizing. The photo-stability of QD ionic liquids is an advantage of the material in applications of IR fiber optics and optoelectronic devices.

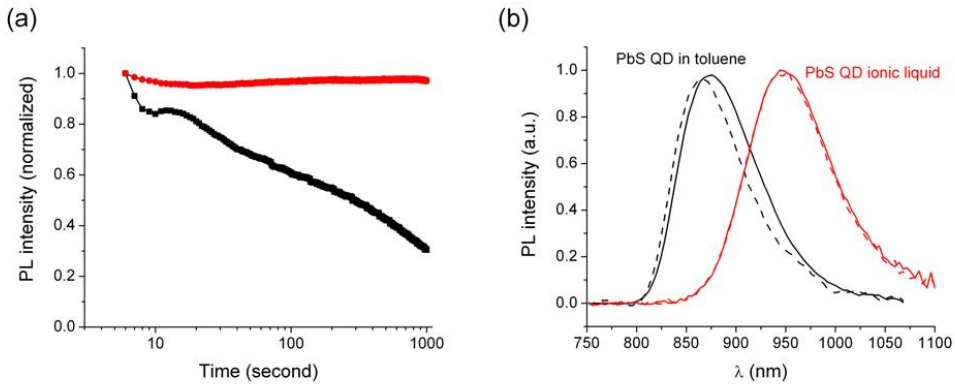

Figure 4.5 (a) Time dependent PL from PbS QDs in toluene (solid square) and PbS QD ionic liquid (dot). (b) PL spectra of PbS QDs in toluene and PbS QD ionic liquid before (solid line) and after (dash line) 1000 seconds of laser (power density ~ 1 mW/mm2) exposure.

4.1.4 Summary

In summary, we developed a simple yet general route to synthesize lead-salt-QD ionic liquids with excellent optical properties. The QD ionic liquids are solvent-free and thus environmentally friendly. Since a thiol capped ionic liquid is used for surface modification, the synthesis method can be easily applied to other semiconductor QDs (e.g. CdS, CdSe and CdTe).

4.2 Superhydrophilic and water resistant coatings from silica nanospheres by a one-step deposition procedure

4.2.1 Introduction

Recent advances in nanoengineering underline the potential of nanoparticles to confer performance characteristics to tailor made materials in a multifunctional and even a selective manner. This is complementary to current approaches that consider nanoparticles rather as additives that at most are able to enhance certain properties of the matrix, in the context of additivity rules or percolation threshold theories. Perhaps, the most direct paradigm to assess the potential of nanoparticles to induce novel properties (rather than simply alter preexisting characteristics) is their deposition to a planar solid surface. Under such circumstances the surface response of the hybrid material arises from the deposited nanoparticles, without necessarily interfering with the bulk properties of the substrate.

Layer by layer assembly (LbL) has been evolved as a flexible, versatile and low cost method to produce ultrathin, hierarchically structured films. Comprehensive reports offer an overview of the relevant methodologies available and also cover the rich diversity of the applicable material systems and the various types of physicochemical interactions involved [23-26]. In principle, the architecture of multilayers relies on alternate absorption of opposite charged species. Polyelectrolytes

are commonly employed for sequential deposition and when nanoparticles are used they bind and stabilize the nanoparticles. However, the presence of polyelectrolytes can have adverse effects on the stability and durability of the (multi)layers (particularly when exposed to aggressive environments) so that post-calcination is often required to remove the organic phase.

In this section, we present a one-step deposition of nanoparticles on a polyolefin substrate without the need of any polyelectrolyte. Instead, the adhesive forces are generated by the charged groups covalently attached to the deposited nanoparticles. The absence of a polyelectrolyte not only eliminates the need for post-calcination, a step that is not practical for polymeric substrates, but also provides great stability to the coating. Judicious selection of the surface groups grafted to the nanoparticles imparts remarkable hydrophilic characteristics to the surface. While, we focus here on a very specific system, the general principles are applicable to a wide range of substrate-particle combinations.

4.2.2 Experimental Section

Cationically modified Silica nanoparticles. Colloidal silica Ludox HS-30 with a mean diameter of 18 nm was purchased from Sigma Aldrich. 3 gram of colloidal silica was diluted with deionized water (30 mL) and sonicated for 30 min. A concentrated solution of HCl (1N) was added to the dispersion followed by the addition of 3.2 g of N-Trimethoxysilylpropyl-N,N,N-trimethylammonium chloride (50 wt %, Gelest). The mixture was stirred at 60 ^{o}C for 10 min. NaOH (0.1 M) was added to adjust the pH to ~5 and the mixture was stirred continuously at 60 ^{o}C for 24 h to complete the reaction. Subsequently, the suspension was dialyzed in deionized water using SnakeSkin tubing (3.5k MWCO, Pierce) for 48 h. The zetapotential of the resulting nanoparticles was +21.5mV.

Plasma treated Polypropylene fabric. Industrial spun-bounded polypropylene nonwoven fabric (0.9 g/cm^3, 240 ± 20 μm thick) with a melt flow index (36.0/600 g/s), supplied by Kimberly-Clark Company, was used as substrate. The substrate was treated with Ar/O_2 (50/50) mixed gas plasma under 234 watt for 2 min. Based on X-ray photoelectron spectroscopy the oxygen/carbon ratio at the surface was estimated to be 0.13.

Surface Contact Angle: Static and dynamic advancing contact angle measurements were carried out by means of a VCA Optima XE apparatus. The water droplets (deionized water from Millipore purification system, specific conductance 0.05 μS/cm, pH 5.5, droplet volume 0.5μL) were monitored by a CCD camera and analyzed by standard drop-shape analysis methods.

4.2.3 Results and Discussion

Plasma treated polypropylene was selected as a model substrate because of the presence of surface charge and various active groups [27,28] while retaining its bulk properties such as light weight, long-term durability and thermomechanical stability. Additionally, both the surface chemistry and the charge density of silica nanoparticles can be precisely tuned, enabling accurate control to their electrostatic behavior [29,30].

Cationically modified silica nanoparticles can be readily deposited onto plasma treated PP giving rise to a dense and uniform thin coating. The TEM picture shown in Figure 4.6a shows complete surface coverage after a single coating cycle (immersion to the aqueous nanoparticle suspension, solvent evaporation followed by repeated rinsing in water). In contrast, there is very little adhesion of silica nanoparticles (regardless of their surface charges) to untreated polypropylene (Figure 4.7).

We note that in our approach the films contain no polyelectrolytes and thus have 100 wt% nanoparticle content [31-33]. Cross-sectional TEM imaging (Figure 4.6b) indicates the presence of 3-4 layers of silica nanoparticles after the one-step process, although typically the formation of a monolayer is observed after a single step in layer by layer methodologies. The moderate magnitude of the zeta potential (ζ=21.5mV) of the nanoparticles is critical for the simultaneous formation of a multi layer (rather than a monolayer) and the good coating quality, since low charge density results in week adhesion, while high ζ values induce strong particle-particle repulsive forces, ultimately inhibiting efficient coating.

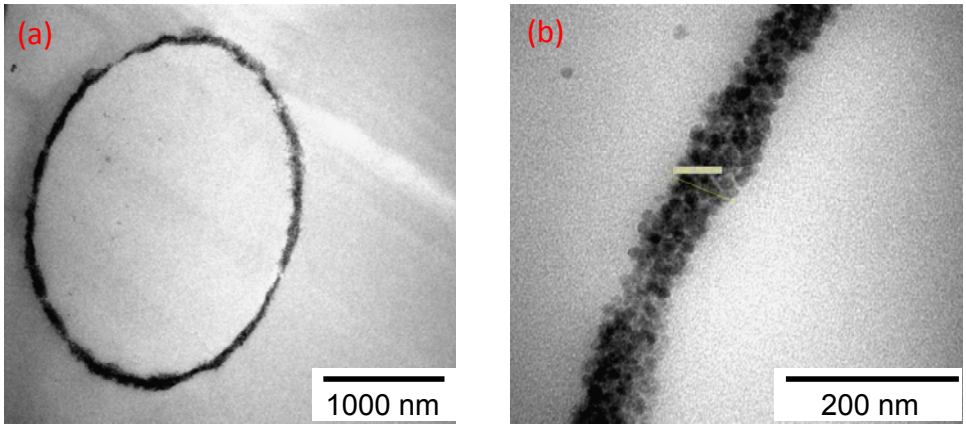

Figure 4.6 TEM images of the plasma treated polypropylene surface coated with cationically modified silica nanoparticles after a one-step deposition

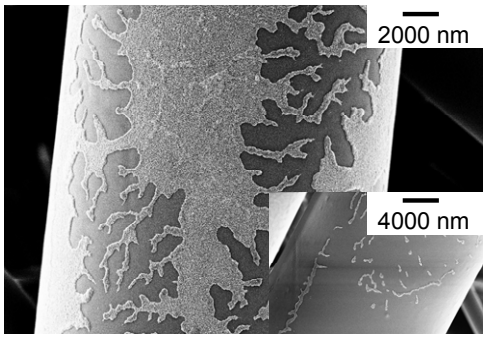

Figure 4.7 SEM image of the untreated polypropylene surface covered with cationically modified silica nanoparticles before water rinsing. The inset shows the morphology of the surface after water rinsing.

In an attempt to evaluate their stability and durability, the coatings were subjected to ultrasonic field while being suspended in four different solvents (water, acetone, ethanol and THF). As shown in Figure 4.8 even after 1 hour of sonication while immersed in the solvents, the coating resists detachment and show excellent water-resistance (Figure 4.8a).

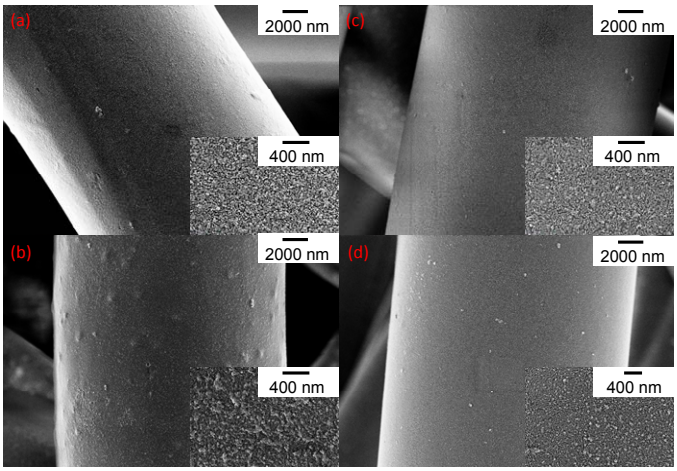

Figure 4.8 SEM images of the plasma treated polypropylene surface coated with cationically modified silica nanoparticles. Images taken after 1 hour of sonication in the presence of various solvents; (a) water, (b) acetone, (c)ethanol, (d) THF.

In addition to its remarkable stability towards water, the coating exhibits superhydrophilic characteristics showing virtually 0^o advancing water contact angle in less than 0.07s ; the series of images shown in Figure 4.9a depict the dynamic evolution of the morphology of an impinging water droplet onto the superhydrophilic surface. In contrast, the corresponding contact angle for the plasma treated polypropylene is 120^o (Figure 4.9b). Wetting of a textured surface from a given solvent critically depends upon the surface-solvent chemical affinity as well as certain topological characteristics of the surface such as roughness and porosity [34,35]. Films exhibiting high levels of hydrophilicity have been previously prepared using layer by layer assembly [36-39] and it has been demonstrated that a minimum thickness of deposited film is a precondition for superhydrophilicity [40]. To fulfill this requirement strategies developed so far are based on the concept of charge reversal of successive monolayers. In contrast, we disclose here an effective method that goes beyond that concept and allows the buildup of a multilayer assembly comprising of a single-type nanoparticles. The approach presented here relies on the appropriate functionalization of nanoparticles to allow the simultaneous deposition of a definite number of layers and also to impart the necessary chemical and topological features for superhydrophilicity. The methodologies developed so far require a multi-step deposition procedure, as opposed to the one-step approach presented here.

In order to explore the wetting mechanism of our system we followed an identical deposition protocol using an acidified colloidal dispersion (pH=4) of the unmodified silica nanoparticles. Due to the rather incomplete surface coverage and the formation of a monolayer (Fig. 4.10), the protonated silica nanoparticles deposited after a single coating cycle do not improve hydrophilicity (Fig. 4.9c). This result underlines the key role of the functional groups to the coating quality in determining the charge density, the layer thickness and topology and altering the intrinsic wetting

characteristics of the deposited film. Note that the water contact angle of unmodified planar silica surface is 20^{o} [31], e.g. substantially higher than the values corresponding to superhydrophilicity.

We note that the cationically modified silica nanoparticles can effectively support sequential deposition of opposite charged nanoparticles. To demonstrate this possibility, carbon black particles were deposited on top of the first level silica coating as shown in Figure 4.11. Given that successive deposition is beyond the scope of this report, current work is focusing on multilayer deposition of opposite charged nanoparticles to create highly tuned surfaces.

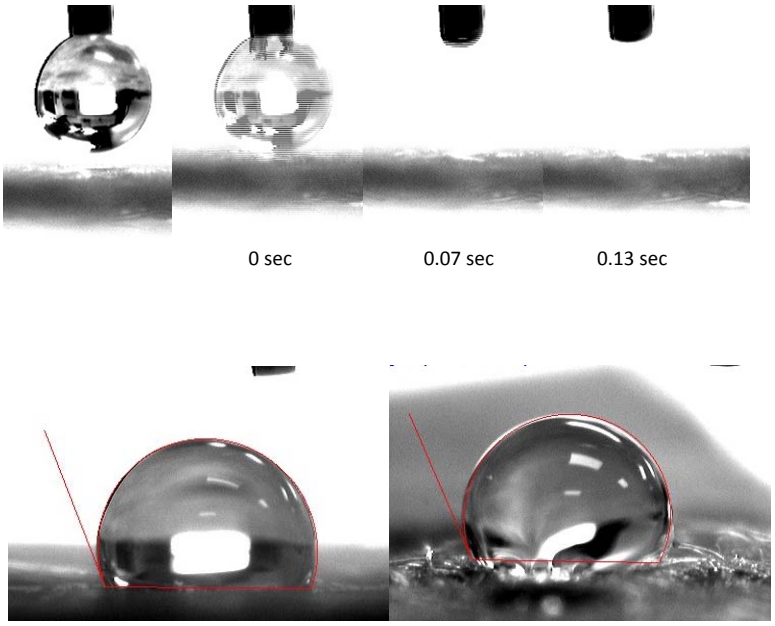

Figure 4.9 Advancing water contact angle of plasma treated polypropylene substrate; (a) Time dependence of the morphological evolution of the impinging water droplet onto plasma treated polypropylene substrate coated with cationically modified silica nanoparticles, (b) uncoated (c) coated with protonated silica nanospheres.

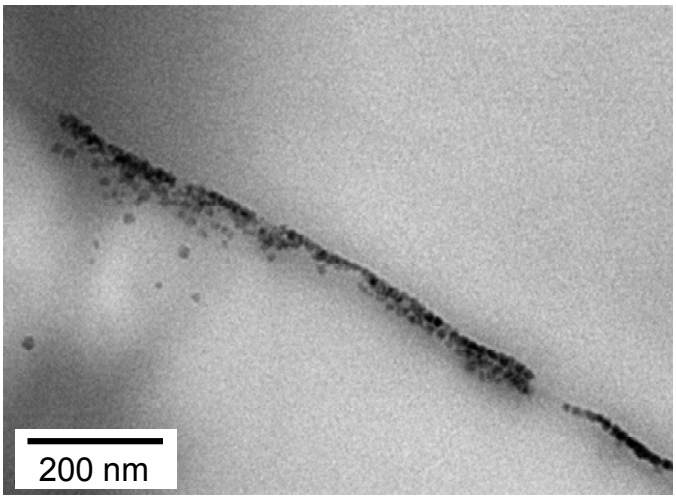

Figure 4.10 TEM image of the plasma treated polypropylene surface after a full coating circle from aqueous colloidal solution of unmodified silica nanoparticles pH=4.

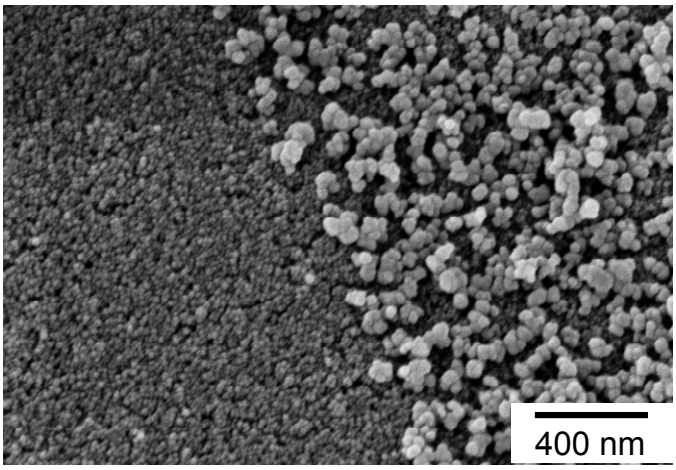

Figure 4.11 SEM image of the plasma treated polypropylene after the first layer deposition of cationically modified SiO2 nanoparticles (left side of Figure 4.11), followed by sequential deposition of negatively charged carbon black nanoparticles (right side of Figure 4.11).

4.2.4 Summary

In summary, we report on a simple, one-step deposition of cationically modified silica nanoparticles to plasma treated polyolefin surface without the need of any polyelectrolyte. The resulting superhydrophilic coating exhibits excellent stability in water and other solvents even under sonication. Superhydrophilicity arises from the simultaneous deposition of 3-4 layers of nanoparticles that can impart desired chemical and topological characteristics to the polymer substrate.

REFERENCES

1. McDonald, S. A.; Konstantatos, G.; Sargent, E. H.; *Nature Materials*, ***2005***, 4, 138
2. Sargent, E. H.; *Adv. Mater*., ***2005***, 17, 515
3. Steckel, J. S.; Coe-Sullivan, S.; Bawendi, M. G.; *Adv. Mater*., ***2003***, 15, 1862
4. Guerreiro, P. T.; Ten, S.; Peyghambarian, N.; *Appl. Phys. Lett*., ***1997***, 71, 1595
5. Wundke, K.; Pötting, S.; Auxier, J.; Peyghambarian, N.; Borrelli, N. F.; *Appl. Phys. Lett*., ***2000***, 76, 10
6. Rodriguez, R.; Herrera, R.; Archer, L. A.; Giannelis, E. P.; *Adv. Mater*., ***2008***, 20, 1
7. Bourlinos, A. B.; Chowdhury, S. R.; D. D. Jiang, Archer, L. A.; Giannelis, E. P.; *Small*, ***2005***, 1, 80
8. Bourlinos, B. A.; Stassinopoulos, A.; Giannelis, E, P.; *Small*, ***2006***, 2, 513
9. Bourlinos, A. B.; Herrera, R.; Chalkias, N.; Giannelis, E. P.; *Adv. Mater*. ***2005***, 17, 234
10. Warren, S. C.; Banholzer, M. J.; Slaughter, L. S.; Wiesner, U. B.; *J. Am. Chem. Soc*., ***2006***, 128, 12074
11. Green, M.; Rahmana, P.; Smyth-Boyle, D.; *Chem. Commun*., ***2007***, 574
12. Murray, C. B.; Kagan, C. R.; Bawendi, M. G.; *Annu. Rev. Mater. Sci*., ***2000***, 30, 545
13. Hines, M. A.; Scholes, G. D.; *Adv. Mater*., ***2003***, 15, 1844.
14. Ohno, H.; *Electrochemical Aspects of Ionic Liquids*, John Wiley & Sons, New Jersey ***2005***, p. 19.
15. Jonscher, A. K.; *Nauture*, ***1977***, 267, 673
16. Pollak, M.; Pike, G. E.; *Phys. Rev. Lett*., ***1972***, 28, 1449

17. Šantić, A.; Wrobel, W.; Funke, K.; *Phys. chem. Chem. Phys*., ***2009***, web publishing.

18. Funke, K.; Banhatti, R. D.; Martiny, C.; Ross, I.; *Phys. chem. Chem. Phys*., ***2002***, 4, 3155

19. Tammann, V. G.; Hesse, W. Z.; *Anorg. Allg. Chem*., ***1926***, 156, 245

20. Sun, L.; Bao L.; Hyun, B.-R.; Bartnik, A. C.; Malliaras, G. G.; Wise, F. W.; *Nano Lett*., ***2009***, 9, 789.

21. Hyun, B.-R.; Chen, H.; Rey, D. A.; Wise, F. W.; Batt, C. A.; *J. Phys. Chem. B*, ***2007***, 111, 5726.

22. Peterson, J. J.; Krauss, T. D.; *Phys. Chem. Chem. Phys*., ***2006***, 8, 3851

23. Jiang, C. Y.; Tsukruk, V. V.; *Adv. Mater*., ***2006***, 18, 829-840.

24. Wang, Y.; Angelatos, A. S.; Caruso, F.; *Chem. Mater*., ***2008***, 20, 848-858.

25. Ariga, K.; Hill, J. P.; Ji, Q. M.; *Phys.Chem.Chem.Phys*., ***2007***, 9, 2319-2340.

26. Hammond, P.T.; *Adv. Mater*., ***2004***, 15, 1271-1293.

27. Liston, E. M.; Martinu, L.; Wertheimer, M. R.; *J. Adhension Sci. Technol*., ***1993***, 7, 1091-1127.

28. Strobel, M.; Walzak, M. J.; Hill, J. M.; Lin, A.; Karbashewski, E.; Lyons, C. S.; *J. Adhension Sci. Technol*., ***1995***, 9, 365-383.

29. Vansant, E. F.; van der Voort, P.; Vrancken, K. C.; "*Characterization and Chemical Modification of the Silica Surface*" Elsevier, Amsterdam, ***1995***.

30. "*Colloidal Silica: Fundamentals and applications*" edited by Bergna, H. E.; Roberts, W.O. Taylor and Francis Group, U.S.A., ***2006***.

31. Lee, D.; Rubner, M. F.; Cohen, R. E.; *Nano Lett*., ***2006***, 6, 2305-2312.

32. Lee, D.; Omolade, D.; Cohen, R. E.; Rubner, M. F.; *Chem. Mater*., ***2007***, 19, 1427-1433.

33. Lee, S. W.; Kim, B. S.; Chen, S.; Shao-Horn, Y.; Hammond, P. T.; *JACS*, ***2009***,

131, 671-679.

34. Bico, J.; Thiele, U.; Quere D.; *Colloids and Surfaces A: Physicochem. Eng. Aspects*, ***2002***, 206, 41–46.
35. McHale, G.; Shirtcliffe, N. J.; Aqil, S.; Perry, C. C.; Newton, M. I.; *Phys. Rev. Lett*., ***2004***, 93, 036102-4.
36. Liu, X.; He, J. J.; *Colloid Interface Sci*., ***2007***, 314, 341-345.
37. Zhang, X. T.; Sato, O.; Taguchi, M.; Einaga, Y.; Murakami, T.; Fujishima, A.; *Chem. Mater*., ***2005***, 17, 696-700.
38. Liu, X.; Du, X.; He, J.; *Chem. Phys. Chem*., ***2008***, 9, 305-309.
39. Wang, F.; Peters, S.; Cuzda, J.; Blunk, R. H.; Angelopoulos, A. P.; *Langmuir*, ***2009***, 25, 4384-4392.
40. Cebeci, F. C.; Wu, Z.; Zhai, L.; Cohen, R. E.; Rubner, M. F. ; *Langmuir*, ***2006***, 22, 2856-2862.

CHAPTER 5

FOULING RELEASE COATINGS BASED ON PDMS-POLYUREA SEGMENTED COPOLYMERS AND NANOCOMPOSITES

5.1 Introduction

The colonization of immersed surfaces by a community of organisms, termed fouling, is considered a major operating problem for the shipping and aquaculture industries [1]. Biofilm formation on marine vessels leads to reduced speed and carrying capacity, resulting in increased propulsive power and fuel consumption, and at the same time accelerating corrosion [2,3]. Suffice to say that a substantial amount of time and money is needed to combat fouling, given that remedial strategies require high maintenance cost.

The recruitments and growth of fouling species strongly depends on several external parameters such as temperature, hydrostatic pressure, water salinity and the availability of nutrients. The great diversity of organisms means that antifouling agents with multilevel functionalities are required. For a while, self-polishing coatings which release toxic tributyltin (TBT) appeared to be an ideal solution, but due to its persistence its use is now globally prohibited [4]. Some antifouling paints containing copper and a range of organic biocides also have detrimental environmental impacts and their use in the future may also be restricted. Thus, the need for development of non-toxic, environmentally friendly antifouling coatings is imperative.

To this end, two main approaches have been utilized; antifouling i.e. technologies that inhibit the settlement of fouling organisms and fouling release coatings that 'release' accumulated fouling hydrodynamically. The ideal coating system involves a tough, non-toxic, polymer that combines the appropriate surface

characteristics necessary to retard settlement and/or the adhesion of fouling organisms such as low surface energy, low surface roughness, low porosity and high molecular mobility In addition, chemical and physical stability in seawater, appropriate film-forming characteristics, and good adhesion to a variety of hull materials are desirable properties. Such a material would act in two ways: By inhibiting settlement i.e. attachment of the colonizing stages (antifouling, AF), and/or by weakening their adhesion strength (fouling release, FR). In the latter case, organisms that do stick can be easily removed hydrodynamically, ideally by simply bringing the ship to speed.

One of the typical approaches to generate antifouling coatings relies on the introduction of a broad-spectrum of organic biocides into the polymer. However, this method has been met with skepticism because of its adverse effect on the underwater ecosystem. The inclusion of isocyano groups or hydrophobic residues [5,6] and the use of peptomimetic macromolecules [7] have also been explored. In addition to artificial materials, some studies have led to the development of responsive antifouling compounds based on natural marine sources [8,9]. On the other hand, fouling release coatings [10-17] typically consist of hydrophobic, low surface energy materials. Polydimethylsiloxane (PDMS) based coatings fulfill such requirements and are the workhorse of the industry.

Silicones based on PDMS represent the only class of polymers currently used in commercial fouling release coatings. The properties which make them suited for this purpose are their inherently low surface energy, glass transition temperature, and modulus, combined with good chemical stability and ease of application. Using pseudobarnacle adhesion tests Brady found that the adhesion strength of hard fouling organisms is generally proportional to both the surface energy and modulus of the coating [18,19]. More recently, these correlations have been extended to living barnacles. Silicones are thus an obvious choice, since they possess both low modulus

and low surface energy [20-26]. However, pure silicones are weak, and are therefore typically reinforced with large quantities of inorganic particles (20-40 wt% or more). Such high particle loadings have detrimental affects on toughness, processability, and polymer mobility, which, in turn, adversely affect fouling release behavior. Stein [27] has found that, although the physical and mechanical properties of PDMS are enhanced by the addition of filler particles, an inverse relationship typically exists between fouling release and filler loading. Thus, the best fouling release coatings exhibit the lowest durability in most cases.

Currently a number of alternative approaches are being considered. Fluoropolymers [28-30] with their low surface energy and promising mechanical properties are serious contenders. Polyethylene glycol (PEG) [31] and its derivatives have been explored in fouling-resistant coatings due to good biocompatibility and resistance to protein adsorption as a result of the formation of a protection layer with water molecules through hydrogen bonding. Webster [32] developed a combinatorial approach based on siloxane-containing crosslinked polymer coatings. Amphiphilic coatings incorporating PEGylated functionalities have also shown promising results [33,34]. Another approach uses deliberate surface patterning with microtopographies to create AF/FR coatings similar to marine species (ex: sharkskin coatings).

In this study we investigated a series of segmented copolymer and nanocomposite coatings as alternatives to conventionally reinforced silicones. Our objective was to develop and evaluate a new generation of practical, non-toxic coatings that combine AF/FR characteristics with good mechanical properties, ease of application and low cost. Specifically we have focused on the following questions:

• Can nanostructuring strengthen PDMS coatings without sacrificing fouling release?

• If so, what are the critical materials parameters (surface and bulk) in such nanostructured systems that combine AF/FR performance with mechanical strength?

In this paper we present our recent efforts to design and synthesize a series of nanostructured coatings based on PDMS-polyurea copolymers as alternatives to conventionally reinforced silicones. We present their bulk and surface properties and correlate to their AF/FR performance. We note that the use of polyurea-based coatings for substrate protection has been previously reported [35-37] but no studies exist on AF/FR behavior.

5.2 Experiment Section

PDMS-polyurea copolymers. PDMS-polyurea copolymers (Table 5.1, 5.2, Scheme 5.1) were synthesized from MDI (4, 4- methylenebis (phenyl isocyanate)) and PDMS-diamine. PDMS diamines of different molecular weight were used to control the ratio of hard (MDI) to soft (PDMS) segments. By adjusting this ratio a series of materials spanning a range of properties can be synthesized. Briefly a 150ml round-bottom flask with magnetic spin bar was vented and filled with nitrogen. One gram of MDI (OEKANAL) was first dissolved into 38 ml THF (Aldrich) and then poured into the flask. Another solution was prepared separately by dissolving the appropriate amount of the PDMS diamine in 62ml THF and added slowly to the flask (ca. 1 hr). The polymerization reaction was continued for another 6 hrs. After polymerization, the liquid solution was poured into a Teflon mold and allowed to air-dry overnight. After drying the material was post-cured overnight at 80 ^{o}C under vacuum.

Table 5.1. PDMS-polyurea copolymer composition

Copolymer	PDMS MW	Weight Ratio PDMS / MDI
A12M	1000	80 / 20
A15M	3000	92 / 8
A32M	30000	99 / 1

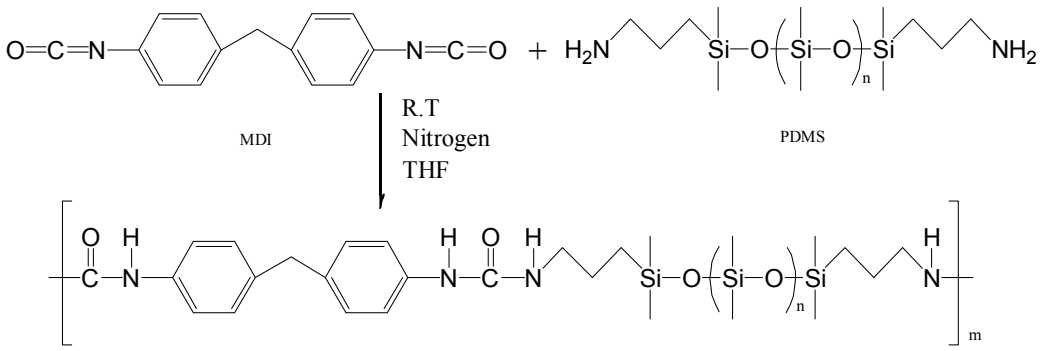

Scheme 5.1. PDMS-polyurea copolymer

A12MF8 three-component random copolymer. Three component copolymers were prepared similarly to the two component system except a portion of the PDMS was substituted by the appropriate amine terminated molecule (Scheme 5.2). A 150ml three-neck round-bottom flask equipped with magnetic bar was vented and filled with nitrogen. 25 ml THF was added to the flask followed by the slow addition (ca. 1 hr) of three solutions containing 1.23 gram of MDI (OEKANAL), 2.5 g A12 and 0.8g of F8 ((4,4'-Diaminooctafluorobiphenyl, Aldrich)) all in 25 ml of THF. The polymerization reaction was continued for another 20 hrs. After polymerization, the liquid solution was poured into a Teflon mold and allowed to air-dry overnight. After drying the material was post-cured overnight at 80 ^{o}C under vacuum.

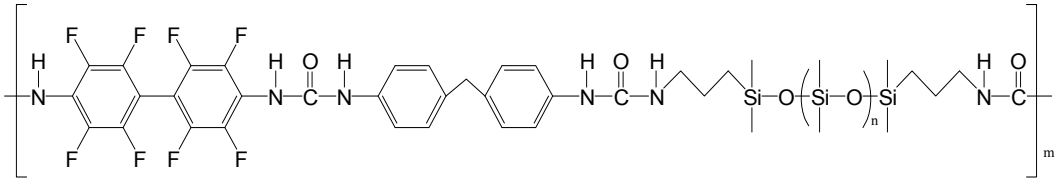

Scheme 5.2. Fluorinated PDMS-polyurea three-component random copolymer

A12MXTJ502/A12MXTJ506/A12MT403 three-component copolymer. In this case portion of PDMS is substituted with amine terminated polyethylene /polypropylene glycol.(JEFFAMINE®, Huntsman) (Scheme 5.3). The following amine terminated PEG/PPG were used. XTJ502: bisamino-terminated, MW=2000; XTJ506: bisamino-terminated, MW=1000; T403: triamino-terminated, MW=440; A12MXTJ502 (1:2/1:5/1:10): molar ratio of PDMS:XTJ502= 1:2/1:5/1:10)

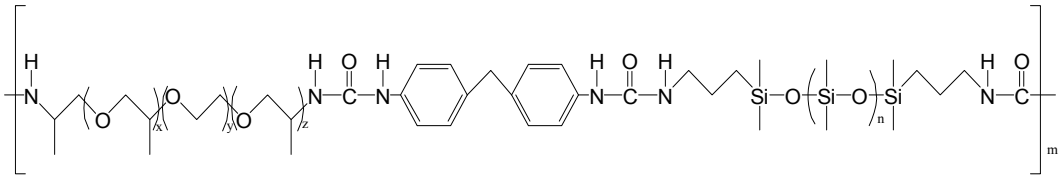

Scheme 5.3. PEG/PPG containing PDMS-polyurea copolymer

A12MPOSS copolymer. A portion of PDMS in the reaction is substituted with an amine terminated polyhedral oligomeric silsesquioxane (aminoethylamino-propylisobutyl POSS AM0275, MW=917.65, Gelest) (Scheme 5.4). The molar ratio was (A12MPOSS1.2: 10wt.% POSS; A12MPOSS1.5: 38wt.% POSS)

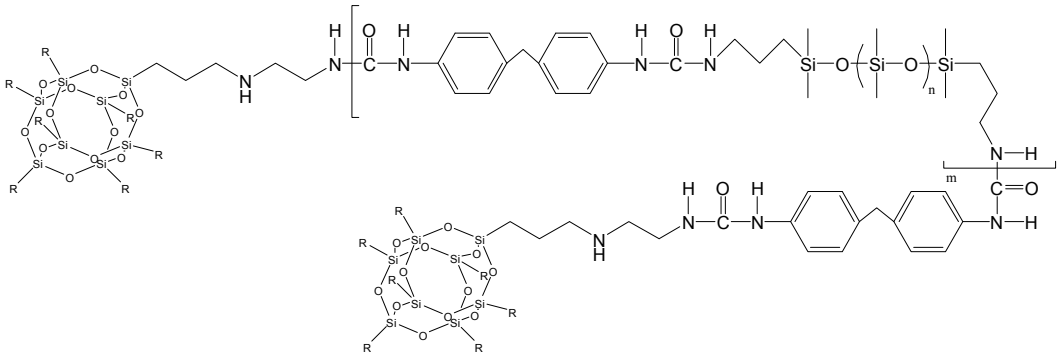

Scheme 5.4. POSS containing PDMS-polyurea copolymer

A12M/PDMS-clay and A12MNIMS nanocomposite. Nanocomposites were prepared by mixing the appropriate molar ratio of MDI and PDMS (A12) with the required amount of nanoparticles. PDMS modified clay and propyl sulfonate PEG/PPG ammonium modified silica (Scheme 5.5) were used. The polymerization reaction was carried out over a period of 6 hours.

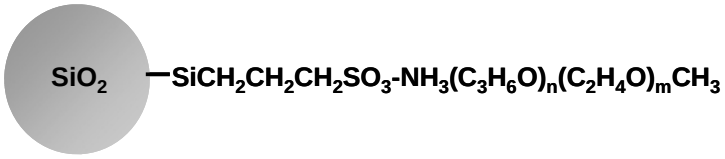

Scheme 5.5. Silica based ionic nanoparticles

Table 5.2. List of the selected PDMS-polyurea copolymers and nanocomposites.

Copolymers*	Description	Composition (molar ratio)
A12M	Pure copolymer	A12:MDI=1:1, A12(PDMS, Mw=1000)
A15M	Pure copolymer	A15:MDI=1:1, A15(PDMS, Mw=3000)
A32M	Pure copolymer	A32:MDI=1:1, A32(PDMS, Mw=30000)
A12MF8	Fluorinated 3-component random copolymer	A12:MDI:F8=1:2:1
A32MF8	Fluorinated 3-component random copolymer	A32:MDI:F8=1:2:1
A12MXTJ502(1:2)	PEG containing 3-component random copolymer	A12:MDI:XTJ502=1:3:2
A12MXTJ502(1:5)	PEG containing 3-component random copolymer	A12:MDI:XTJ502=1:6:5
A12MXTJ502(1:10)	PEG containing 3-component random copolymer	A12:MDI:XTJ502=1:11:10
A12MXTJ506	PEG containing 3-component random copolymer	A12:MDI:XTJ506=1:2:1
A12MT403	PPG containing 3-component random copolymer	A12:MDI:T403=1:1.15:0.1
A12MPOSS1.2	Copolymer with POSS chain-end	A12:MDI=1:1, 10wt.% POSS
A12MPOSS1.5	Copolymer with POSS chain-end	A12:MDI=1:1, 38wt.% POSS
A12MPDMSclay	Copolymer blend with PDMS modified clay	A12:MDI=1:1, 10wt.% PDMS-clay
A12MNIMS	Copolymer blend with PEG/PPG modified silica	A12:MDI=1:1, 10wt.% PEG/PPG-silica

FT-IR characterized were recorded on a Mattson Galaxy 2020 FTIR single-beam spectrometer under a nitrogen atmosphere. All Galaxy 2000 series benches provide a resolution limit of 4 wavenumbers (cm^{-1}), and they use either a deuterium triglycine sulphate (DTGS) or mercury cadmium telluride (MCT) detector and potassium bromide (KBr) beamsplitter to cover the spectral range from 600cm^{-1} to 400 cm^{-1}.

Dynamic Mechanic Analysis (DMA) tests were performed in tensile mode using a DMA2980 from TA instruments. 30x6 mm^2 rectangular shape, free standing samples were cast from solution. Spectra were taken from -130 to 200 ^oC at a single frequency (1Hz).

Tensile tests were performed on an Instron 5800 Series controller equipped with a 5kN load cell. Dog-bone shape specimens were cast from solution. Every set of samples was measured five times for accuracy.

X-ray photoelectron spectroscopy (XPS) was performed on a Surface Science Instrument SSX-100 UHV system.

Dynamic Contact Angle (DCA) measurements were made on a Cahn Radian DCA analyzer using a fixed, transfer speed of 24μm/s. Specimens consisted of free standing films cut into 1x3 cm^2 rectangles.

Surface topography was characterized with a MicroXAM interferometric Surface Profiler from ADE Phase Shift using the optical non-contact mode. The technique provides a 1nm vertical and 500 nm lateral resolution, respectively.

Scanning Electronic Microscopy (SEM) images were obtained on a Keck Field Emission Scanning Electron Microscope (FE-SEM), LEO 1550. The spatial resolution is 1nm at 20keV and 2.5nm at 5keV, respectively.

Marine Testing. (1) Settlement of spores of Ulva. Spore settlement assays were conducted using standard methods. Spore density was assessed by cell counts on fixed slides using a fluorescence microscope to visualize cells and image analysis software

for counting. Sporelings (young plants) were grown for 7 days. Sporeling biomass was quantified by measurement of the in-situ fluorescence of chlorophyll in a Tecan fluorescence plate reader. Fluorescence was recorded as Relative Fluorescence Units (RFU).

(2) Attachment strength of sporelings of Ulva. The strength of attachment of the sporelings was assessed using a water jet. One of each of the six replicate slides was subjected to a single impact pressure. A series of water pressures were used and the proportion of biomass removed determined using the fluorescence plate reader (initial biomass – remaining biomass = biomass removed).

(3) Leachate testing. Coatings and glass slide controls were soaked in 100mL of filtered seawater for six days. At 72 hour intervals, the seawater is replaced and approximately 100 brine shrimp nauplii are exposed to this leachate. Their survival is monitored for two days after which the mortality of the brine shrimp subjected to the experimental coating's leachate is compared with the mortality in the control solutions.

(4) Settlement of barnacle cypris larvae. The settlement assay consists of placing a 0.4mL drop of seawater containing 20-40 barnacle (Balanus amphitrite) cypris larvae on the experimental coatings. The larvae were allowed to settle for 72 hours, or until the settlement rate on glass control surfaces reached 50%. At this time, the number of barnacles that had settled on each surface was counted and compared to the settlement rates of the controls (glass slides) [38]. All marine tests were performed on coatings deposited on glass slides by spray-coating.

Selected fouling organisms. The coatings were evaluated using two common fouling organisms viz. the green alga Ulva and the barnacle Balanus amphitrite. Dispersal of Ulva is mainly through motile, quadriflagellate zoospores (approximately 7-8 μm in length), which are released in large numbers and form the starting point of the assay (Callow et al. 1997). The swimming spores settle and adhere through discharge of a

glycoprotein adhesive (Callow & Callow 2006) then rapidly germinate into sporelings (young plants), which adhere weakly to silicone fouling-release coatings (Chaudhury et al. 2005, Finlay et al. 2008). The barnacle, Balanus amphitrite (Clare and Hoeg 2008) liberates nauplii that develop through six planktonic stages to the highly specialised settlement stage – the cypris larva (cyprid), which explores surfaces using a reversible adhesion mechanism. Once a suitable site for settlement has been located, permanent cement is discharged that anchors the larva in place during metamorphosis and early juvenile development.

Spray-coating Process. All of the samples prepared for marine testing were made by a standard spray-coating process (Scheme 5.6).

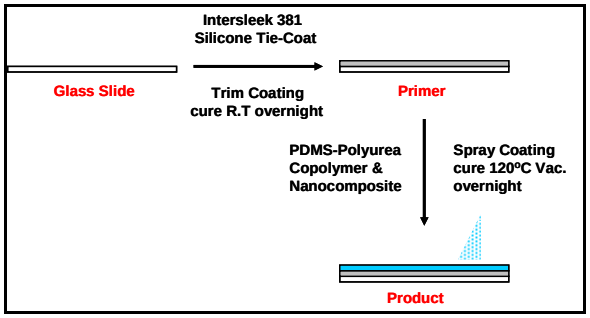

Scheme 5.6. Standard glass slides used as substrate. Trimming Intersleek 381 (commercial available, light greyish) as Tie-coating, with a top coat of Intersleek 381, a typical antifouling material. Coating thickness ranged from several hundreds nanometers to several microns. For a specific sample, the thickness was uniform, for different samples, the thickness varied.

5.3 Results and Discussion

Characterization by FT-IR. FT-IR measurements were used to measure the degree of completion of polymerization and possible formation of side products. As polymerization proceeds the number of amine groups of the diamine and the carbon-

nitrogen double bonds of the diisocyanate reactants decrease by forming an amide group in the copolymer. Due to the overlap of the amine/amide groups we focused mainly on changes in intensity of the C=N stretching at 2200~2350 cm^{-1} as an indication of the degree of polymerization reaction. The low intensity of the peak characteristic of the C=N from MDI after polymerization suggests that the reaction proceeds to completion in most cases. According to figure 5.1a, the diamine F8 shows the least reactivity probably due to its lowest basicity because of the presence of strong electronegative groups (fluorinated aniline). That the decrease in intensity is due to the reaction with the PDMS rather than self-addition was confirmed by running a control in the absence of PDMS under identical conditions. No decrease in the IR intensity was observed confirming that the MDI indeed reacts with the PDMS to form a copolymer. Additionally it was found that the reaction of the MDI with the amine terminated PDMS is almost completed within the first 180 minutes with minimal changes even after the reaction was extended overnight (Fig. 5.1b).

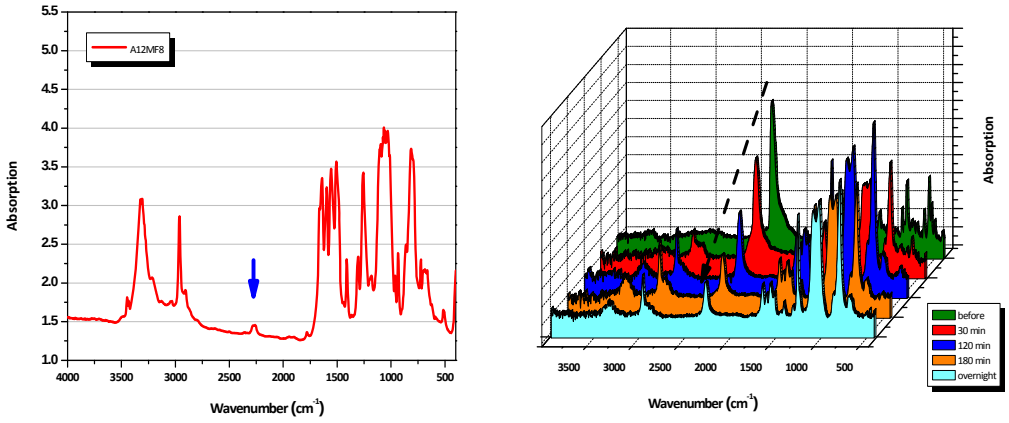

Figure 5.1 (a) FT-IR static identification A12MF8 (left); (b) FT-IR dynamic tracing A12M (right)

Mechanical Properties of PDMS-polyurea copolymers. The mechanical properties from tensile testing and DMA measurements show some interesting trends. Figure 5.2a shows the stress-strain plots for the three basic copolymers. All copolymers exhibit elastomeric behavior with extensive elongation before failure. The PDMS content (A32>A15>A12) in the segmented copolymers affects the extent of microphase separation and the ability of the hard and/or soft domains to crystallize [39-42], both of which affect the mechanical properties of the copolymers. When the relative fraction of the hard domain is low, hard microdomains dispersed in a continuous soft matrix are formed. The hard domains act as physical cross-links to reinforce the soft matrix. As the fraction of the hard domains increases, their connectivity increases and eventually leads to a network structure. The modulus of the copolymers containing 80, 92 and 99% PDMS is 85.9, 16.4 and 0.38 MPa respectively. Consistent with the tensile testing the storage modulus obtained from DMA shows a range of moduli covering more than three orders of magnitude (Fig. 5.2b). Thus a series of materials based on the PDMS-polyurea copolymers with a range of mechanical properties is readily accessible.

The mechanical response is mainly governed by the chemical composition and the resulting copolymer morphology. A phase-separated morphology is expected because of the incompatibility between the hard (MDI) and the soft (PDMS) domains. In block copolymers, the covalent bonding between different segments results in several phase-separated morphologies. A phase-separated morphology is theoretically predicted at a critical value of $\chi N \sim 10.5$, where χ and N are the Flory-Huggins interaction parameter and degree of polymerization, respectively. Although the presence of strong secondary interactions such as hydrogen bonding adds to the complexity of the system, a similar transition is expected for segmented copolymers.

All copolymers clearly exhibit a Tg at -115ºC due to the soft, PDMS segment (Fig. 5.2b). For the A32M copolymer based on the longest PDMS chains melting of the crystalline PDMS phase is observed at – 55 °C. The lack of a distinct hard domain Tg is not surprising given the extent and strength of hydrogen bonding and the lack of cooperative segmental motion in the isocyanate domains. All copolymers present a remarkably broad, temperature independent rubbery plateau. The distinct glass transition of the PDMS phase and flat rubbery plateau suggest a high degree of phase separation in all systems. The broad, temperature independent plateau is attributed to the presence of strong hydrogen-bonding in the hard domain, which extends softening of the hard segment to higher temperatures. Softening of the hard segments will lead to a decrease in the plateau modulus. In addition to varying the length of the PDMS segment, the modulus of the materials can be controlled over a wide range (Fig. 5.2b) by using short-chain (e.g. fluorinated) diamines, or by adding nanoparticles to form nanocomposites. The three-component random copolymer A12MF8 exhibit a storage modulus of 335MPa at room temperature which is more than two thousand times stronger than the pure copolymer A32M (0.17MPa). All nanocomposites show consistently higher modulus compared with the pure copolymer. The storage modulus of POSS based nanocomposites is 104 and 250 MPa for systems containing 10 and 38 wt% POSS, respectively (POSS1.2; POSS1.5). Thus, the mechanical response of the copolymers can be easily fine-tuned. One of the objectives of this study was to correlate the effect of modulus on fouling release behavior (vide infra).

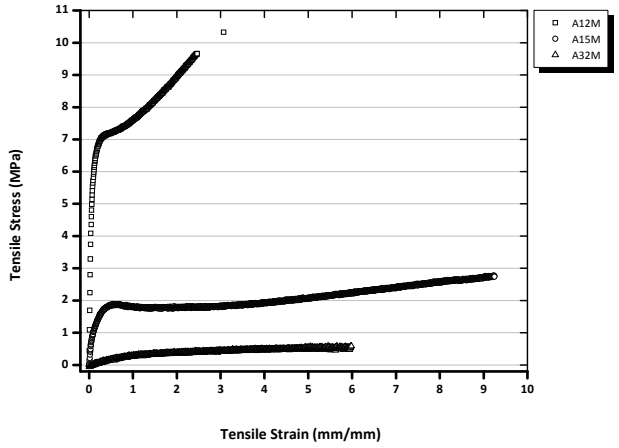

Figure 5.2 (a) Mechanical properties by tensile testing

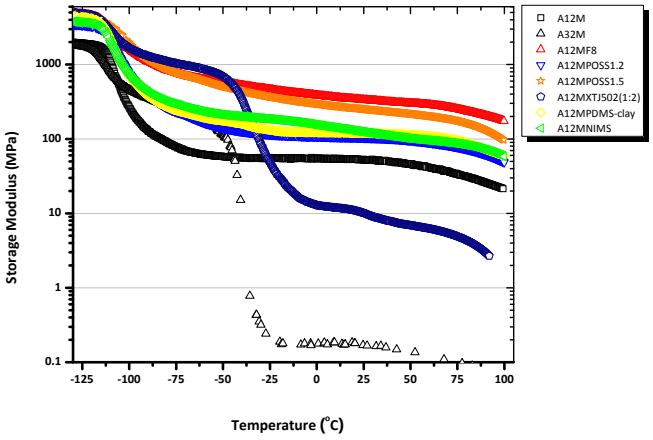

Figure 5.2 (b) Mechanical properties by DMA

Surface Characterization. For two-component segmented copolymers, it is relatively easy to define their molecular structure based on AB repeat units; however, multi-component copolymers are far more complex. For example, three-component random copolymers such as A12MF8, contain MDI, whose reactivity is higher than other aliphatic type isocyanates, and two kinds of diamines, A12 and F8. Even though the

three components could be arranged randomly overall, the divergent reactivity among them still can lead to a microscale segregation. Additionally, surface segregation is expected to add another level of complexity. To that end we have used XPS measurements to characterize the surface composition of the coatings and compare with the calculated (bulk) values (Fig. 5.3). For the pure copolymer (A12M) the surface is enriched with silicon and oxygen compared to the bulk values. The opposite is true for carbon. Introducing the amine terminated POSS groups seems to partially reverse the effect especially at higher POSS loadings. The POSS shows a strong tendency of diffusing to higher surface energy region, and self-assembling during solvent vaporization [43]. Interestingly, introduction of the fluorine containing diamine leads to surface with a slight variation of composition for the surface and the bulk.

.

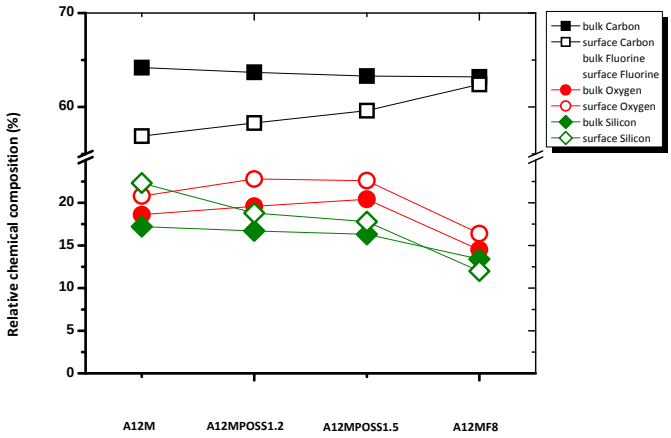

Figure 5.3 Comparison of surface composition using XPS measurements to calculated bulk values for a series of copolymers.

Dynamic Contact Angle, DCA, measurements were used to complement the XPS analysis. The DCA measurement is based on the Wilhelmy plate method [44-47]. As shown in equation (1), the measured force (F), is a difference between the wetting

force and the buoyancy counter force. The wetting force equals the surface tension of the liquid (γ_L), perimeter of sample (P), and contact angle (cos θ). The buoyancy counter force is equal to the density of the liquid (ρ_L), gravitational constant (g), cross sectional area of sample (A), and depth of immersion (d).

$$F = \gamma_L P \cos\theta - \rho_L g A d \qquad (1)$$

The DCA measurements provide information on both advancing and receding contact angle as well as possible hysteresis. The advancing angle is obtained during the wetting process while the receding during the de-wetting process. Figure 5.4 shows the results for several PDMS-polyurea copolymers. Teflon was included for comparison. Note that in all materials the advancing angle is comparable and even higher than PTFE (112^o). We believe the PDMS segments of the copolymers are mainly contributing to this hydrophobic behavior. However, in contrast to PTFE various hydrophilic domains such as urea segments are present on the surface leading to a relatively lower receding angle. Contact angle hysteresis strongly relates to chemical heterogeneity and surface roughness. All samples show a large hysteresis compared to Teflon indicating the existence of chemical/topographical heterogeneities due to the phase separation.

POSS containing nanocomposites exhibit what is known as the superhydrophobic effect [48] which has been proposed for potential biofouling prevention [49]. A12MPOSS has an advancing angle of 140 degrees. However, its receding angle is only 30 degree. This kind of large contact angle hysteresis can be indicative of amphiphilic character.

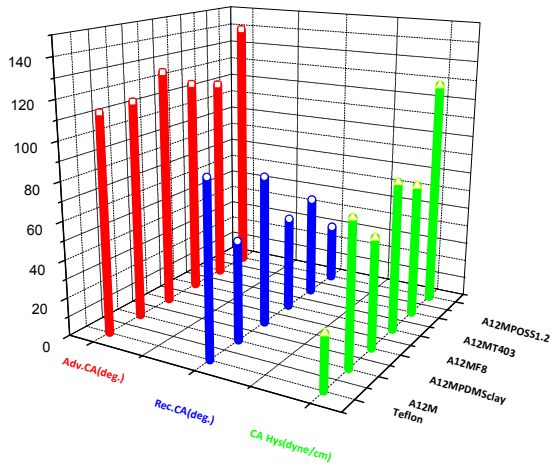

Figure 5.4 Dynamic contact angle measurement

Studies of morphology and topography. Interferometric profilometer results are shown in Figure 4.5. As the chemistry is varied so is the surface topography of the samples. For example, introducing the fluorinated amine leads to a different profile (Fig. 5.5a). The bright spots throughout the bright bands are probably due to the crystalline segments in the polymer chain. The fluorinated-diamine, F8, can force the F8/MDI/F8 repeat unit into a highly regular arrangement and more crystalline segments. These features were not observed in the pure copolymer A12M (Fig. 5.5b).

We were able to control the surface morphology by introducing other groups and nanoparticles into the copolymers. For example, addition of polyethylene glycol/polypropylene glycol (Fig. 5.5d) leads to a much smoother surface compared to the pure copolymer A12M (Fig. 5.5c). We hypothesize that the smoother surface is due to more polar/hydrophilic domains present which have a higher probability to migrate to the surface or induce secondary interactions (H-bonding). This feature could have an important implication in biofouling. Nanoparticles can play a significant role in phase separation of various immiscible polymer blends and, thus, surface

topography [50]. Depending on their surface chemistry, nanoparticles can be miscible with only the hard, soft or both phases. Thus the nanoparticles not only provide reinforcement but can influence phase separation. When clay nanoparticles are used a layered topography can be seen (Fig. 5.5e). The last example is based on nanocomposites containing POSS (Fig. 5.5f). A network structure can be seen in this case. The network formation depends on the POSS loading.

Owing to our interest in using these copolymers as fouling release surfaces we investigated the temporal evolution and aging of surface morphology and topography. The fresh A32MF8 (Fig. 5.5a) sample did not show any macroscale (300x300 μm^2) features and only some indefinite patterns on the smaller scale. However, after annealing a pattern characteristic of phase separated domains started to appear. After 10 days of annealing a pattern similar to the cast samples was obtained, suggesting that the pattern forming process is similar to crystalline growth, as molecules take time to arrange, aggregate, fold, and evolve.

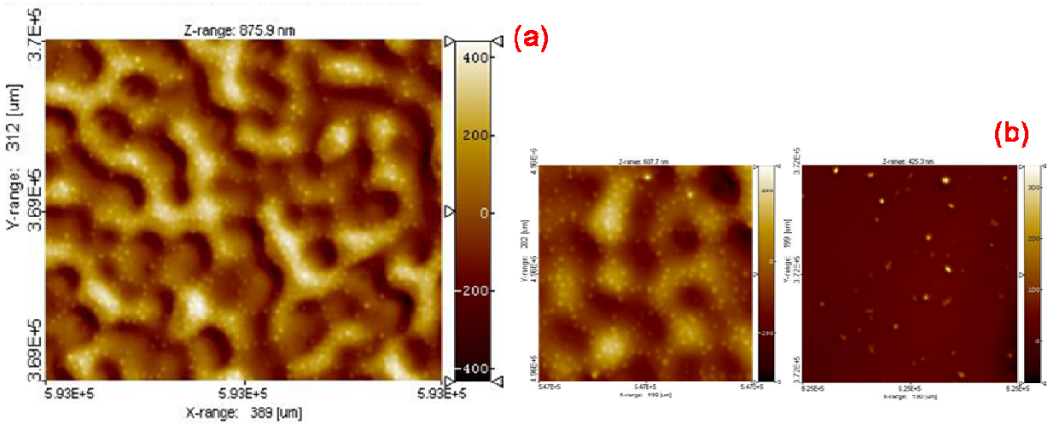

Figure 5.5 2-D profilometer measurements of spin-coating samples (a) A32MF8; (b) Comparison of A32MF8 (left) and A12M (right) at higher magnification

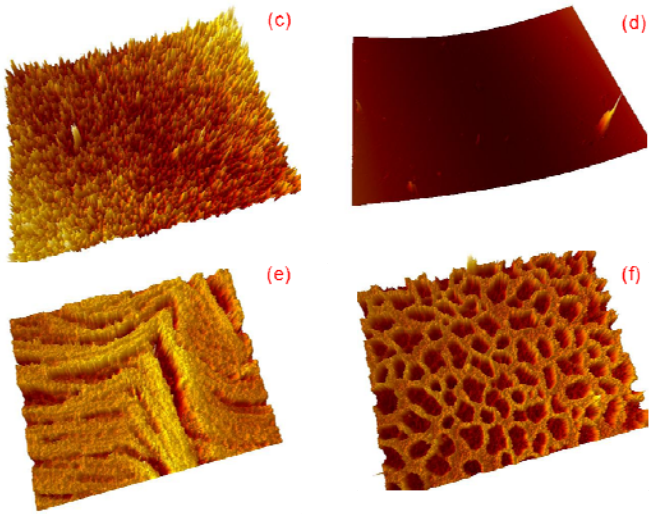

Figure 5.5 3-D profilometer measurements of solvent-casting samples (c) A12M; (d) A12MT403; (e) A12MPDMSclay; (f) A12MPOSS1.5

Scanning electron microscopy images of fractured surfaces for a series of copolymers and nanocomposites were taken in an effort to provide morphological information of the interior of the samples (Fig. 5.6). The image of the pure copolymer A12M (Fig. 5.6a) shows a bright/dark pattern characteristic of a phase separated morphology. The A12MPOSS copolymer (Fig. 5.6b) shows entirely different features. However, this different morphology is more prevalent towards the top of the sample (free surface). The rest of the sample appears more similar to the base copolymer. Consistent with the profilometry studies the POSS clusters appear to segregate to the free surface of the sample.

The last example is an image of A12MNIMS (Fig. 5.6c) based on silica nanoparticles functionalized with a charged corona. These ionic nanoparticles originally have a particle size around 20 nm. After blending with the copolymer, the nanoparticles aggregate into bigger sizes (~100nm). The polymer matrix is dominated

by PDMS rich domains. We expect that the nanoparticles because of their polarity will be attracted to the urea rich domains. The nanoparticles appear distributed into several bands parallel to the sample surface. The origin of the band formation is not clear at present.

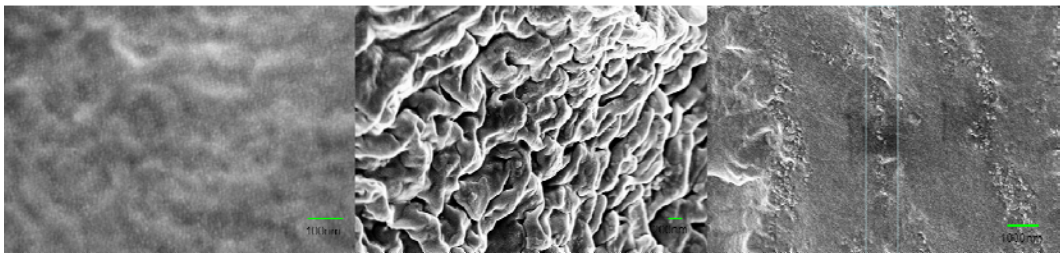

Figure 5.6 SEM image of (a) A12M; (b) A12MPOSS; (c)A12MNIMS (from left to right)

Marine Testing. Owing to our interest in developing fouling release coatings, samples were prepared by spray-coating and tested with two different test organisms. None of the samples showed any signs of toxicity after two weeks of leaching. Standard methods for spore settlement and sporeling adhesion strength of Ulva were used. The results were compared against two standards: glass slide and Silastic^{R}-T2 (Dow Corning), a PDMS elastomer prepared as described in Schumacher et al [51]. Settlement density of spores on the PDMS-polyurea coatings and the two standards is shown in Figure 5.7. Spore settlement was higher on all PDMS-polyurea copolymers compared to the glass and PDMS standards. The corresponding sporeling removal using a water jet with different surface water pressure is shown in Figure 5.8 and summarized as required pressure for 50% removal in Table 5.3. As expected the PDMS control shows a higher percentage removal compared to glass at equivalent water pressure. The neat A12M copolymer shows a higher removal than PDMS at all

pressures. Recently, POSS was reported as ideal additive for polysiloxane-based antimicrobial coating [52]. In our study, the performance of POSS modified A12M (A12MPOSS) was poor at the lowest water pressure, but became better at higher pressures. Furthermore, a clay-based nanocomposite showed even better removal while the fluorine containing A12M copolymer outperformed all samples.

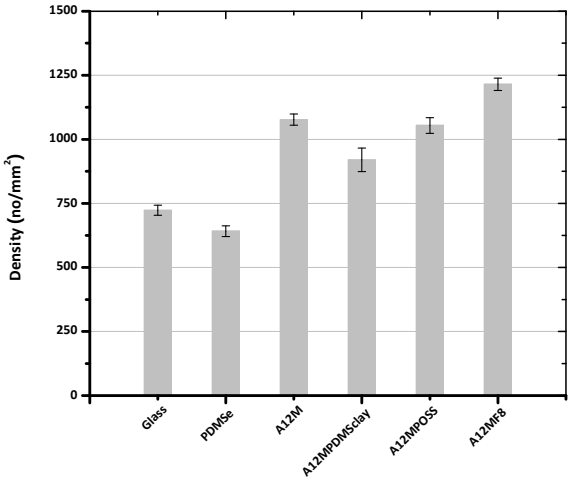

Figure 5.7 The settlement density of spores of *Ulva* on coatings.

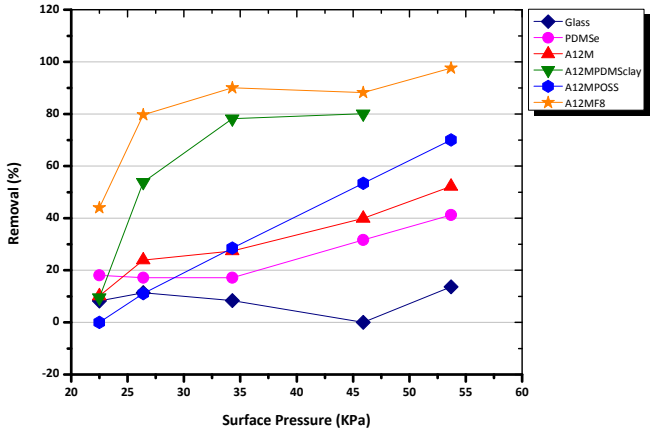

Figure 5.8 Detachment of 7 day old sporelings of Ulva plotted as a function of surface water pressure (kPa).

Table 5.3. Surfaces arranged in order of ease of fouling-release. Critical surface pressures for 50% removal of sporeling biofilm derived from curves. Extrapolation for some points has been necessary.

Surface	Estimated surface pressure (kPa) for 50 % removal
A12MF8	23
A12MPDMSclay	26
A12MPOSS1.5	44
A12M	52
PDMSe	62 (extrapolated)
Glass	80 (extrapolated)

Another set of coatings was tested for settlement of barnacle cypris larvae. Figure 5.9 shows the percent mortality of brine shrimp (Artemia sp.) after exposure to the coating leachates. There is no significant difference in the mortality of brine shrimp subjected to the leachate of the copolymer coatings and that from the glass control suggesting that there are no toxic elements detected in the coatings. The corresponding barnacle (Balanus amphitrite) cypris larvae settlement is shown in figure 5.10. Settlement on the PDMS control was significantly higher than on coating A12MXT403 (ANOVA, $F=26.095$, $p<0.0001$). More importantly, the settlement was inhibited on all other coatings. The cyprids in those samples were alive and active also indicating that toxicity was not detected and was not an issue with these larvae

We hypothesize that the improved anti-settlement performance of the copolymer coatings might be due to the presence of polyethylene glycol segments in the copolymers. Thus, we have synthesized a series of copolymers based on amine-terminated PEG. It is important to distinguish between monofunctional and bifunctional amine terminated PEG as it will be either part of the copolymer chain end or main chain, respectively. We have also adjusted the molar ratio between PDMS and PEG in an effort to balance the fouling release behavior with the mechanical

properties of the coatings. Large amounts of soft PEG segments can sacrifice the mechanical properties. The tri-functional T403 is fully dominated by PPG. The presence of more hydrophobic PPG and/or the resulting cross-linked structure leads to worse settlement behavior albeit better than the control. These new copolymer coatings are environmentally friendly and exhibit low or no barnacle larvae settlement.

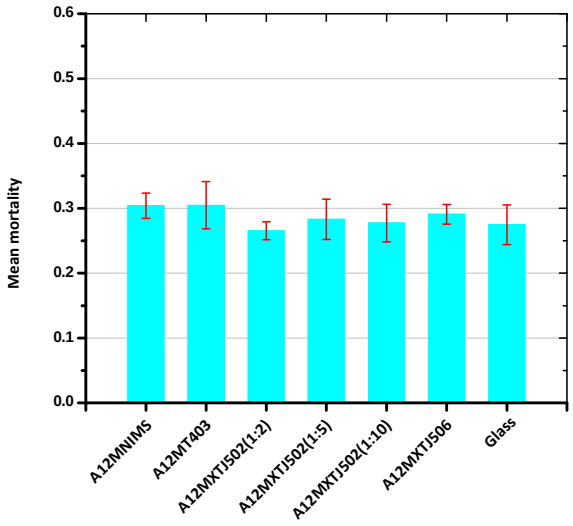

Figure 5.9 Mean mortality of brine shrimp after exposure to coating leachates.

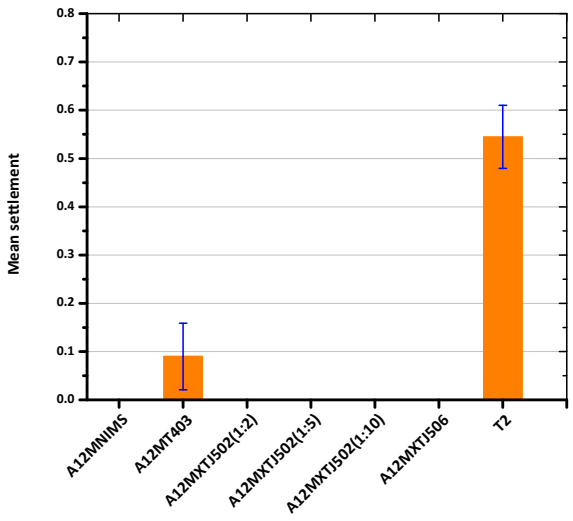

Figure 5.10 Mean settlement of barnacle cypris larvae analyzed by coating.

Marine Testing at Cornell. More marine testing was performed at Cornell University in cooperation with Prof. Harvell Drew [53-58] in the Ecology and Evolutionary Biology Department and his graduate student David Baker. The experimental thin-film samples are made by direct casting to avoid the roughness issues associated with spray coating and therefore provide more information about the intrinsic antifouling properties of the materials. The testing was carried out in an artificial tank meant to imitate the sea ecology system. The tank was made from non-toxic materials in order to decrease the damage to the growth of the microorganism, and limit the external factors. The typical short term experiments allowed the microorganisms to settle for 2~5 weeks.

Standard purification procedure for the experimental samples:
Air-dry the experimental samples at least 24hrs (first stage)
Soak in de-ionized water and uniformly shake for 24hrs (~300r.p.m)
Again air-dry the experimental samples at least 24hrs (second stage)
Soak in acetone and uniformly shake for 24 hrs (~300r.p.m)
Store the experimental samples and solvent separately

The best outcome of this testing was the development of a new evaluation scheme which is convenient and reliable. This evaluation sequence is composed of scanning and imaging analysis, UV-VIS spectrum analysis, and spectrum photometric equation derivation [59]. After systematically compiling and graphing all data, a conclusion can easily be reached.

First short term experiment

This was the first marine testing experiment (Table 5.4) conducted in an artificial tank in place of the real sea environment. This motivation is to quickly get a concept of the samples performance so that further modification can be made. It is known [60] that the targeted microorganism will easily wash out with acetone, so spectroscope analysis can be used to evaluate the amount of fouling.

The data from UV-VIS spectroscopy is presented in figures 5.11-13. However data analysis is also an important issue. The results in figure 5.11 show the absolute intensity of the spectrum. Although the baseline wasn't flat and fluctuated frequently, the absolute intensity may still represent certain characteristics of the samples. The systems mixed with commercial biocide generally attracted more settlement than others. This is due to the production process which only allowed the biocide to be retained on the samples surface and hence was easily washed away. A well-developed biocide should be well dispersed throughout the polymer matrix, and gradually diffuse to the interface over time. Halloysite could be a potential candidate for biocide materials and was investigated in subsequent studies.

Only focusing on samples 3-11 one interesting trend can be seen. The A12M series (3-5) and A32M series (9-11) had relatively less settlement than the A15M series (6-8), thus the settlement is not in proportion to molecular weight (A32>A15>A12). Because pure PDMS (32) has the best antifouling performance it might be expected that the antifouling performance would worsen as the PDMS content is decreased. A32M (99% PDMS, 1%polyurea) performed reasonably well and further decreasing the PDMS content continued to worsen performance as seen in A15M (92% PDMS, 8% polyurea). However, beyond a certain critical concentration, increasing the urea group content (and therefore decreasing PDMS content) actually enhanced antifouling performance as seen in A12M (80%PDMS, 20%polyurea). In

this sample, the urea linkage also proved beneficial in repelling fouling. Therefore, given these trends finding the appropriate ratio of PDMS to polyurea is critical.

Figure 5.12 represents the results from the integration of the peak area and Figure 5.13 was constructed using the following known [59] equations:

chlorophyll a=$11.93E_{664}$-$1.93E_{647}$

chlorophyll b=$20.36E_{647}$-$5.50E_{664}$

Using these methods, the overall trends observed were similar to those noted using absolute intensity analysis; the commercial biocide systems performed the worst, and the relation among the A12M, A15M, and A32M series was preserved. Figure 5.14 was produced by imaging analysis. Although, some small differences can be seen when compared to the UV-VIS spectrum analysis, the general trends are preserved. The systems containing commercial biocide were poor antifouling performance, and the relative fouling settlement appeared as A15M>A12M>A32M. Additionally the nanoclay composites seemed to enhance fouling (10%>3%>pure).

Table 5.4 Description of testing samples for first short term experiment

No.	sample	discription
1	Intersleek381	Elastomeric Foul Release Tie Coat
2	Intersleek425	Elastomeric Foul Release Coating
3	A12M	Copolymer MDI+A12
4	A12M25A3	Copolymer filled with 25A clay at 3% wt. loading.
5	A12M25A10	Copolymer filled with 25A clay at 10% wt. loading.
6	A15M	Copolymer MDI+A15
7	A15M25A3	Copolymer filled with 25A clay at 3% wt. loading.
8	A15M25A10	Copolymer filled with 25A clay at 10% wt. loading.
9	A32M	Copolymer MDI+A32
10	A32M25A3	Copolymer filled with 25A clay at 3% wt. loading.
11	A32M25A10	Copolymer filled with 25A clay at 10% wt. loading.
12	A15M25A3_N521949	Copolymer filled with 25A clay at 3% wt. loading. + 5% commercial biocide N521949
13	A15M30B3_N521949	Copolymer filled with 30B clay at 3% wt. loading. + 5% commercial biocide N521949
14	A15M25A3_N556297	Copolymer filled with 25A clay at 3% wt. loading. + 5% commercial biocide N556297
15	A15M30B3_N556297	Copolymer filled with 30B clay at 3% wt. loading. + 5% commercial biocide N556297
16	A15M25A3_Ziram5	Copolymer filled with 25A clay at 3% wt. loading. + 5% commercial biocide Ziram
17	A15M30B3_Ziram5	Copolymer filled with 30B clay at 3% wt. loading. + 5% commercial biocide Ziram
18	A15M25A3_Algaefix5	Copolymer filled with 25A clay at 3% wt. loading. + 5% commercial biocide Algaefix
19	A15M30B3_Algaefix5	Copolymer filled with 30B clay at 3% wt. loading. + 5% commercial biocide Algaefix
20	A15M25A3_Diuron5	Copolymer filled with 25A clay at 3% wt. loading. + 5% commercial biocide Diuron
21	A15M30B3_Diuron5	Copolymer filled with 30B clay at 3% wt. loading. + 5% commercial biocide Diuron
22	A12MF3_25A	Three components random copolymer filled with 25A clay at 3% wt. loading.
23	A12MF3	Three components random copolymer MDI+A12+F3
24	A15MF3	Three components random copolymer MDI+A15+F3
25	A15MF3_25A	Three components random copolymer filled with 25A clay at 3% wt. loading.
26	A15M_Melamine	Three components random copolymer MDI+A15+Melamine
27	A32MF3	Three components random copolymer MDI+A32+F3
28	A32MF3_25A	Three components random copolymer filled with 25A clay at 3% wt. loading.
29	A12MP	Copolymer filled with Phosphorous clay at 3% wt. loading.
30	A12M30B3	Copolymer filled with 30B clay at 3% wt. loading.
31	A12M30B10	Copolymer filled with 30B clay at 10% wt. loading.
32	PDMS	Pure Polydimethylsiloxane

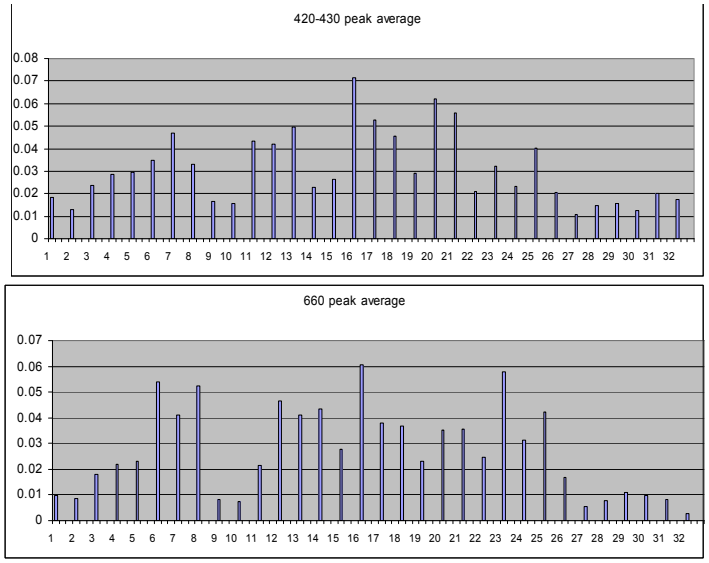

Figure 5.11 UV-VIS spectrum analysis; from absolute peak intensity

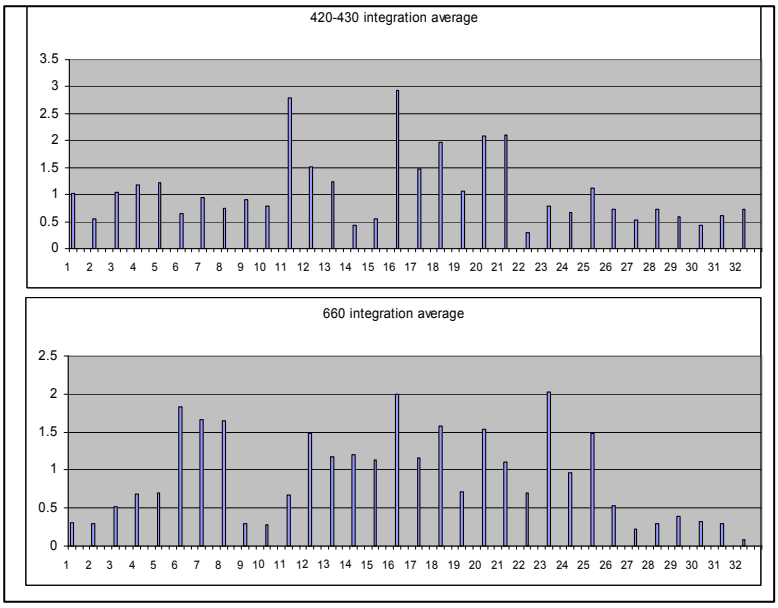

Figure 5.12 UV-VIS spectrum analysis; from integrated peak area

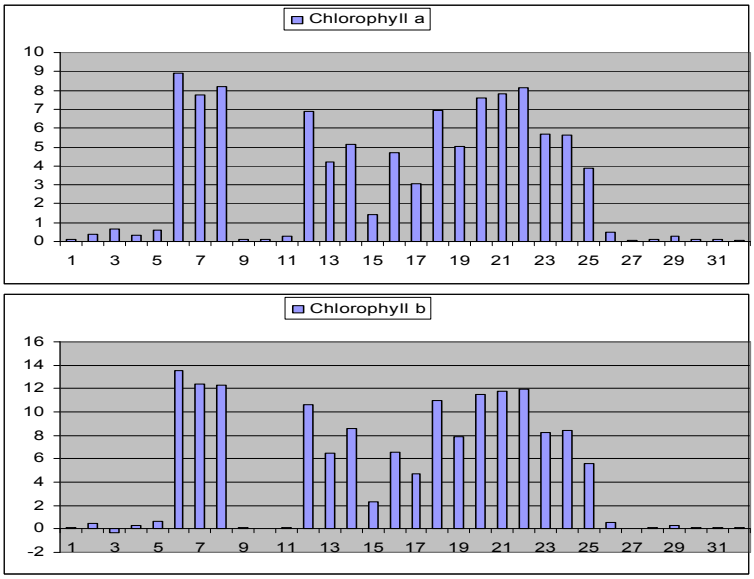

Figure 5.13 UV-VIS spectrum analysis; from equation calculation

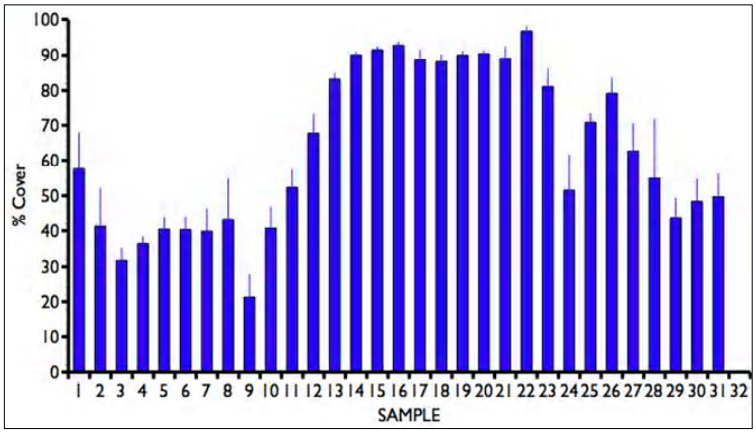

Figure 5.14 Imaging analysis

Second short term experiment

The length of this experiment (Table 5.5) was 20 days. (Fig. 5.15). The same purification process described previously was applied. Scanning analysis was used to observe the remaining amount of microorganisms at each stage (Fig. 5.16).

Based on the initial scanning analysis, it was determined that sample position in the tank had a significant influence on the microorganism distribution. Samples located near the water source can be considered to be at a dynamic site (Fig. 5.17) which leads to heavier fouling. Taking the Teflon sample (Fig. 5.16) as an example, the microorganisms appeared to grow more rapidly at the dynamic site compared to the static site; however, as previously mentioned, different species of organisms prefer particular environments. Since in fouling experiments, many variables are involved that could affect the outcome, we attempted to limit the number of variables tested. External factors are so influential that certain variations could be more important than the intrinsic properties of the materials thus to compare the materials themselves, all external variations were fixed as much as possible.

Table 5.5 Description of testing samples for second short term experiment

Ref no.	color	composition	Descriprion
1	red	A12M	Pure copolymer
2	white	A12M25A	Copolymer filled with 25A clay at 3% wt. loading.
3	green	Teflon	commercial product, as standard
4	yellow	A12MF6	Three components random copolymer MDI+A12+F6
5	orange	A32MF6	Three components random copolymer MDI+A32+F6
6	blue	A32MF8	Three components random copolymer MDI+A32+F8

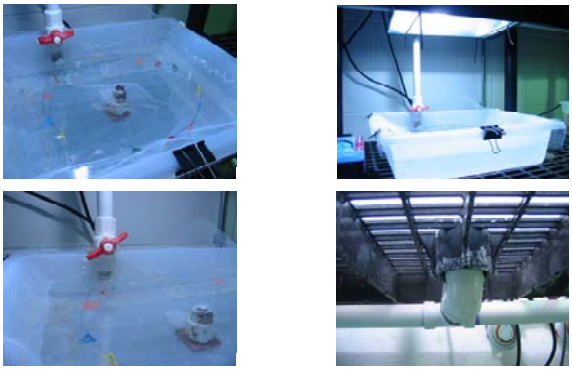

Figure 5.15 Second short term experiment set-up

(a)

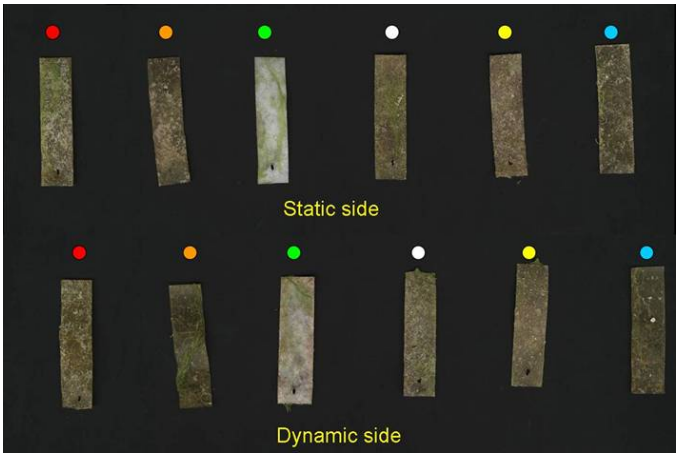

(b)

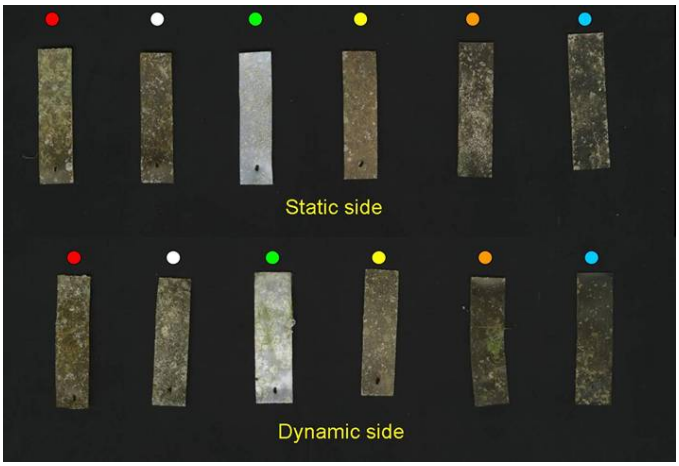

Figure 5.16 Scanning image (a) thin film samples after first stage air-dried, (b) thin film samples after second stage air-dried

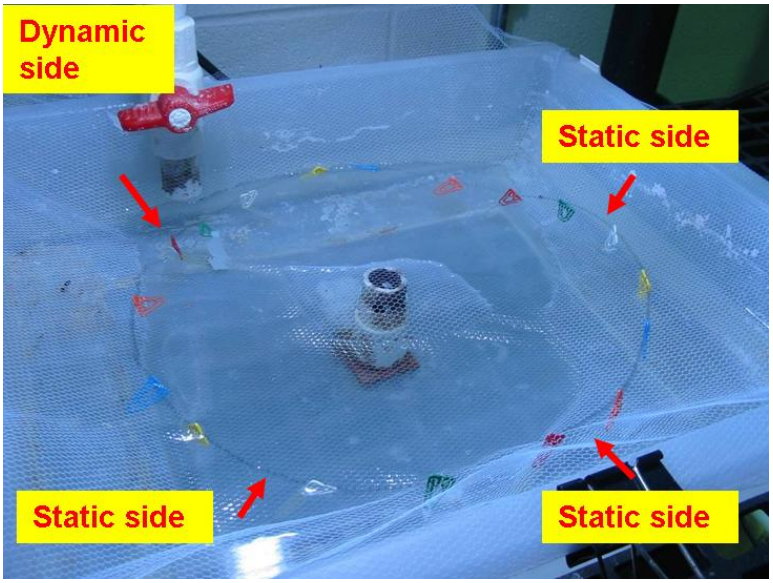

Figure 5.17 Random distributions of the samples

The majority of the target microorganisms could be washed away by acetone which can then be used for UV-VIS spectral analysis (Fig. 5.18). UV-VIS spectral measurements can be greatly influenced by small variations or impurities in the solvent being analyzed so all variables must be controlled as much as possible. The target signal located at 660nm is attributed to one species of Chlorophyll [60]. Calculations on this signal allow us to compare the relative antifouling performance of each sample based on this one organism (Fig. 5.19). The fluorinated polyurea copolymer samples (A12MF6, A32MF6, A32MF8) seem to have better performance than the standard Teflon.

On the other hand, the signal located at 560nm and attributed to a different fouling organism, showed the opposite trend. This method of analysis, UV-VIS spectroscopy, is appropriate only for investigating limited species of microorganisms.

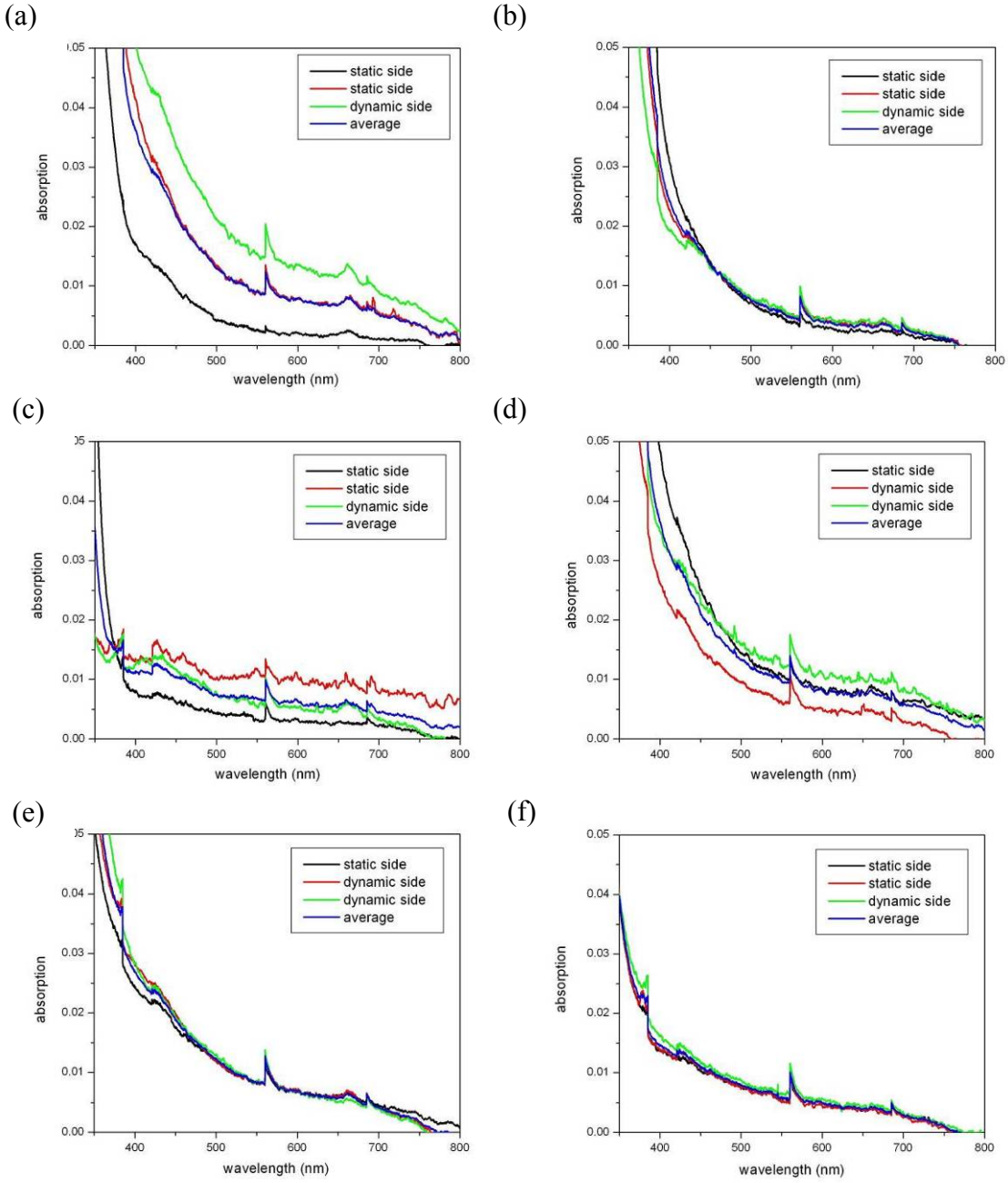

Figure 5.18 UV-VIS spectrum analysis results (a)A12M, (b)A12M25A, (c)A12MF6, (d)A32MF6, and (e)A32MF8

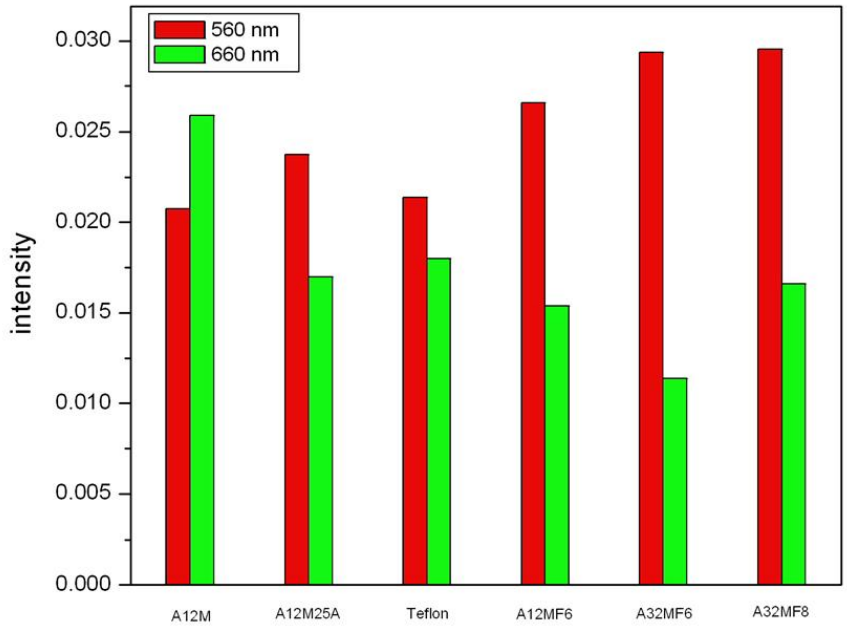

Figure 5.19 Chlorophylls a UV-VIS quantitative analysis

Third short term experiment

To avoid the variables introduced by differences in current speed, this experiment only focused on samples placed at static sites (Fig. 5.20). Only five different polymers were tested (Table 5.6).

The results from the scanning analysis (Fig. 5.21) showed highly reproducible results this time as opposed to the outcome of the previous experiment. The Teflon and A12MF8 samples seem to have less fouling settlement in general; this was especially true in the case of A12MF8 to which the microorganisms rarely attached. The thin-film surface of the A12MF8 appeared to change color which is due to the existing amide or isocyanide group undergoing oxidation in the environment. This is an important discovery because in imaging analysis the surface color differences are used to determine the amount of fouling. Thus, the color change in the A12MF8

samples due to oxidation could mistakenly be attributed to fouling accumulation if care is not exercised when interpreting results. The pure polymer A12M demonstrated the worst performance under scanning analysis, thus the chemical modifications made can be deemed successful in enhancing the antifouling properties of this polymer.

The UV-VIS spectrum analysis (Fig. 5.22-23) results were slightly different than those using scanning analysis. The pure polymer still exhibited relatively poor antifouling properties, however in this case the Teflon performed better than A12MF8. Several factors deserve consideration in this discussion. First, the intensity of the UV-VIS spectrum was obviously lower than in previous experiments because the static position attracts fewer target microorganisms. Also, the ecology of the tank, meant to simulate a real environment, was constantly changing thus the natural life cycles of certain microorganisms could have an effect on the results. Thus it is important to know the natural evolution and conditions of the testing environment.

Table 5.6 Description of testing samples for third short term experiment

Ref no.	composition	Descriprion
1	Teflon	commercial product, as standard
2	A12M	Pure copolymer
3	A12MF8	Three components random copolymer MDI+A12+F8
4	A32MF8	Three components random copolymer MDI+A32+F8
5	Polymer S	Poly(1,4-butylene succinate), extended with 1,6-diisocyanatohexane

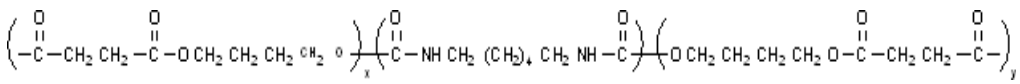

Polymer S =

Poly(1,4-butylene succinate), extended with 1,6-diisocyanatohexane

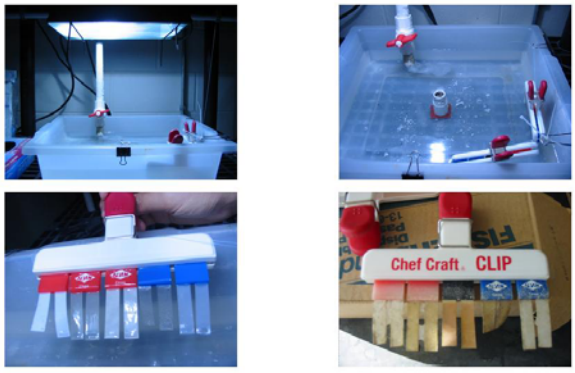

Figure 5.20 Third short term experiment set-up

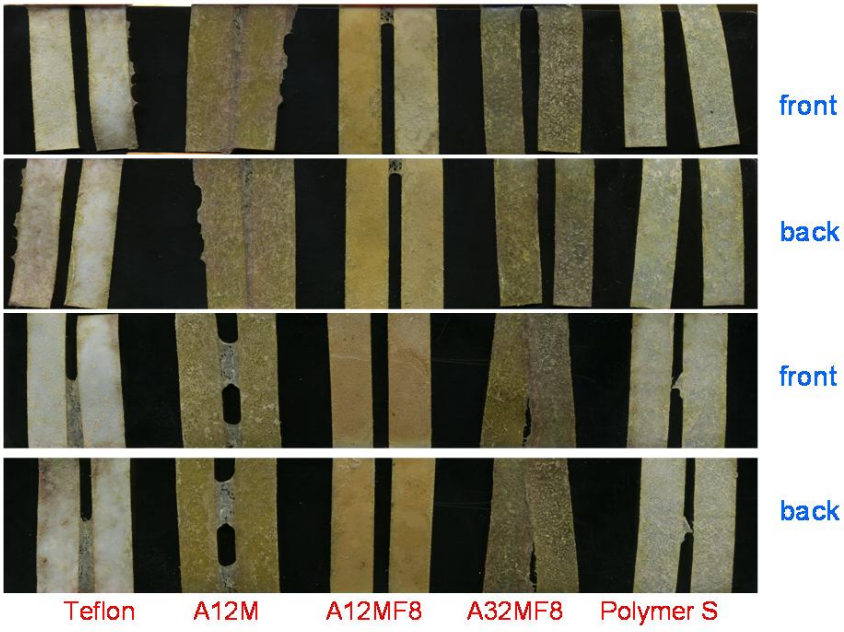

Figure 5.21 Thin-film samples after first stage drying

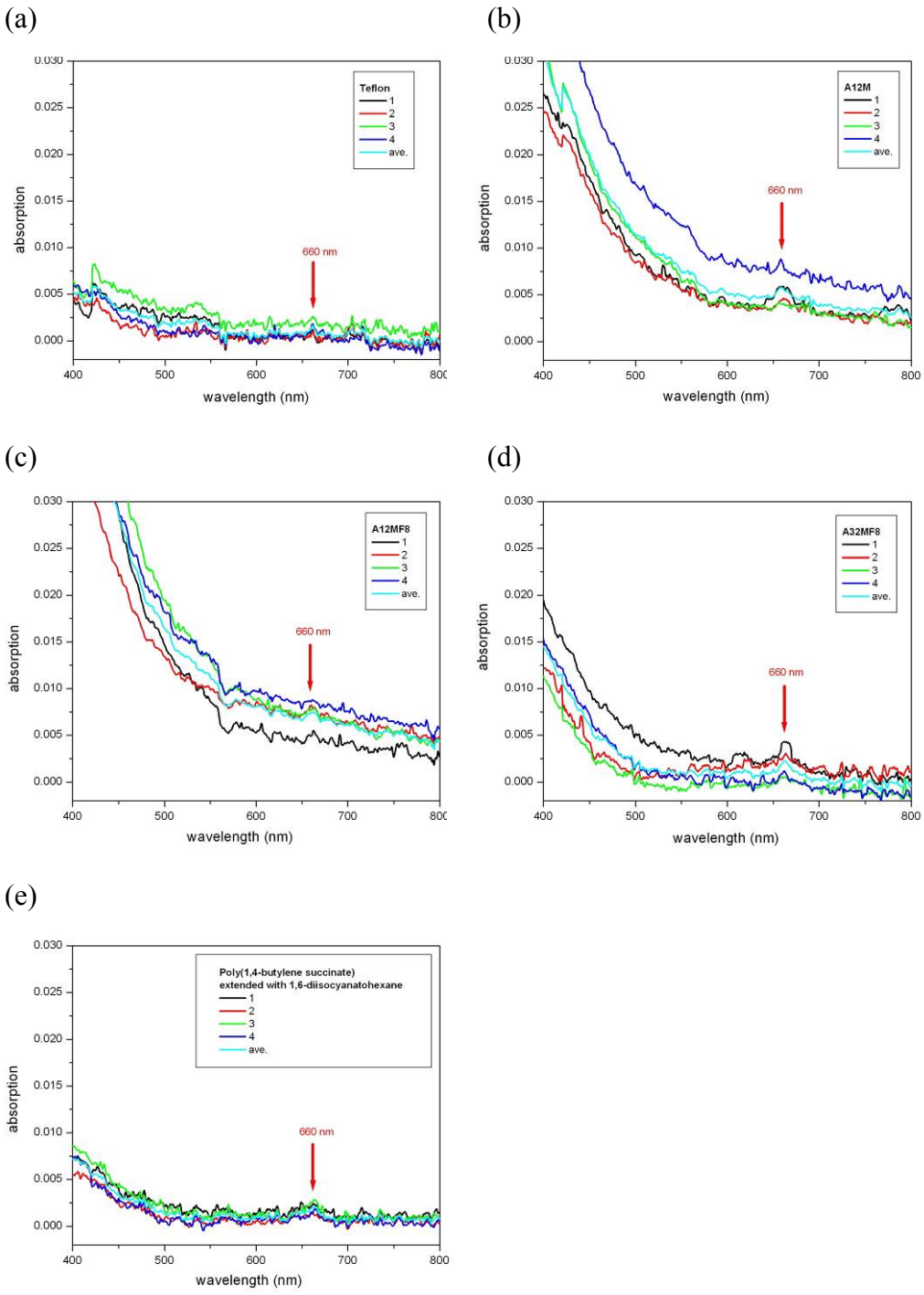

Figure 5.22 UV-VIS spectrum analysis results (a)Teflon, (b)A12M, (c)A12MF8, (d)A32MF8, and (e)Polymer S

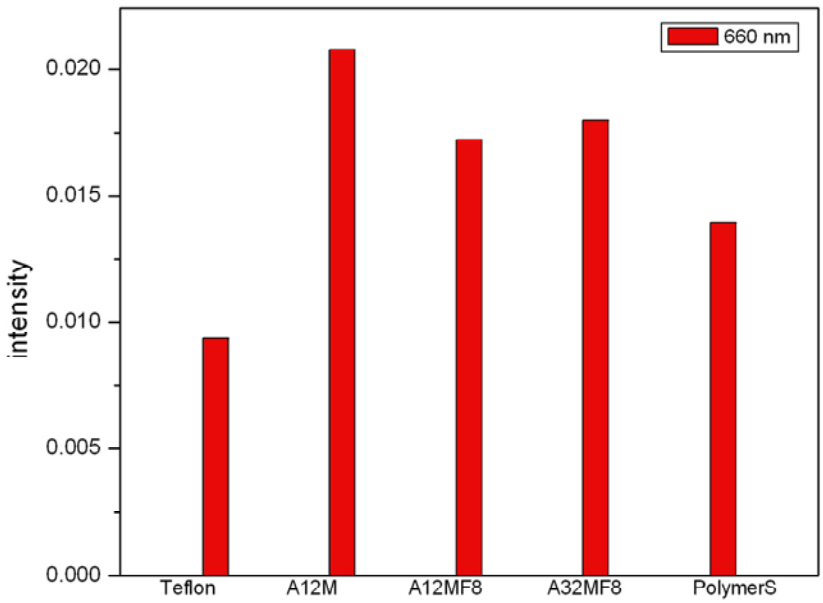

Figure 5.23 Chlorophylls a UV-VIS quantitative analysis

Fourth short term experiment

Poly (ethylene glycol) and its derivatives are excellent materials for minimizing protein absorption [61-64]. This could be one component of a microorganism's adhesion mechanism so the A12MD400 and A12MD2000 materials (Table 5.7) were specifically designed to minimize this. Also, the effect of the length of the repeat unit on antifouling properties was investigated. The experimental set-up (Fig. 5.24) was quite similar to previous experiments with nylon fishing line used to replace the plastic clamp because of the unstable dye used on its surface.

The scanning analysis (Fig. 5.25) revealed an unusual situation. Samples contaminated by fouling organisms are ordinarily light green in color; however in this test the samples became darker than usual. It is obvious that the fouling species dominate during this time period are different than during previous testing times. The pure PDMS and A12MF8 still showed less settlement than other materials. Although

pure PDMS can initially resist fouling, once settlement does occur there is generally a strong binding force present that makes the fouling organisms extremely difficult to remove. Oxidation and its associated color change were again observed in the A12MF8 samples, but relatively little fouling was present. The sample containing halloysite, A12MSM1M, didn't perform well in this test though the idea of adding halloysite remains promising.

Table 5.7 Description of testing samples for forth short term experiment

Ref no.	composition	Descriprion
1	P400M	block copolymer MDI+P400
2	P2000M	block copolymer MDI+P2000
3	A12MSM1M	Copolymer filled with SM1M at 3% wt. loading.
4	A12MF8	Three components random copolymer MDI+A12+F8
5	PDMS	pure Polydimethylsiloxane

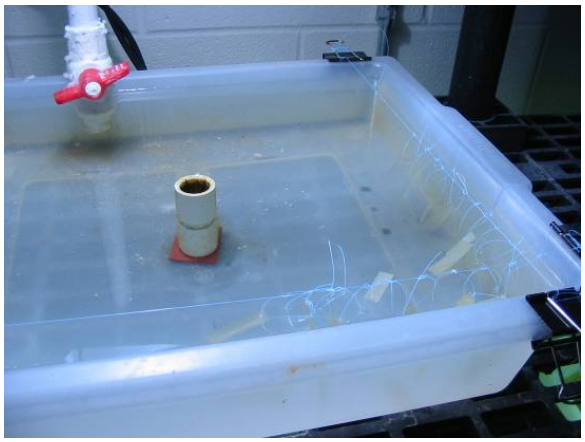

Figure 5.24 Forth short term experiment set-up

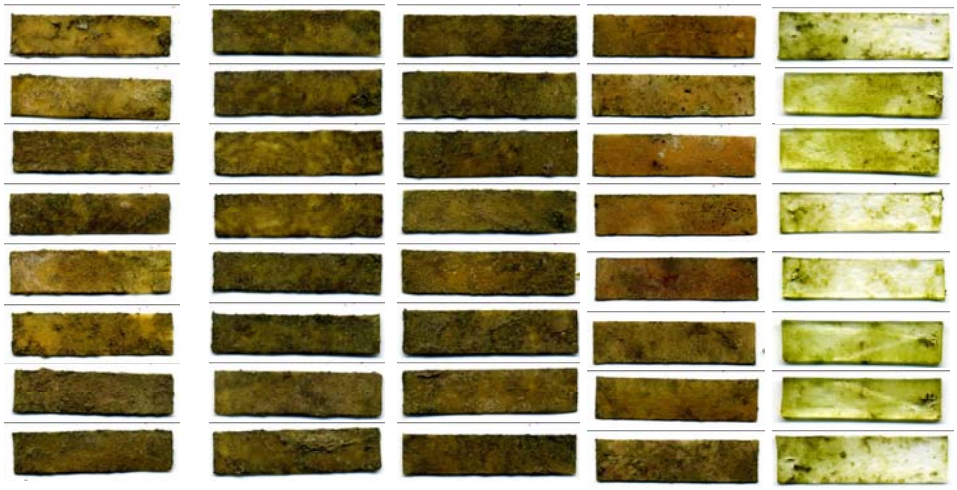

Figure 5.25 Scanning analysis

5.4 Summary

In summary, we have synthesized a series of new PDMS-polyurea segmented copolymers and nanocomposites and evaluated their fouling release behavior. The synthetic approach is scalable and large scale coatings can be produced readily using standard techniques such as spray coating.

The extent of microphase separation and the ability of different domains to crystallize affect the surface and bulk properties of the copolymers and nanocomposites. By varying the amount of the soft PDMS segments as well as using nanoparticles for reinforcement we were able to develop copolymers with moduli covering a range of more than four orders of magnitude. Surface studies using profilometry and AFM show surface nanostructuring due to phase separation with both nano and microscale features. The morphology and topography can be further modified by the presence of fluorinated groups in the copolymer or the presence of nanoparticles in nanocomposites.

All copolymers and nanocomposites are stronger (in some cases by orders of magnitude) than neat PDMS. Preliminary studies on the settlement and removal of Ulva show that the critical pressure to remove 50% of sporelings is at least comparable and in some cases lower than on neat PDMS. Additionally a series based on mono-, bifunctional PEG segments shows improved settlement behavior of barnacle larvae compared to standard PDMS. These findings are quite significant as the new coatings combine the fouling release characteristics of PDMS but are much stronger and tougher than PDMS. Further studies will examine the fouling-release characteristics of adult barnacles.

REFERENCES

1. Omal, I; *Chem. Rev.*, ***2003***, 103, 3431-3448

2. Townsin, R. L.; *Biofouling*, ***2003***, 19, 9–15

3. Schultz, M. P.; *Biofouling*, ***2007***, 23, 331-341.

4. Yebra, D. M.; Kiil S., Kim, D. J.; *Progress in Organic Coatings*, ***2004***, 50, 75–104

5. Kitona, Y.; Nogata, Y.; Shinshima, K.; *Biofouling*, ***2004***, 20, 93-100

6. Nogata, Y.; Kitano, Y.; Yoshimura, E.; *Biofouling*, ***2004***, 20, 87-91

7. Statz, A. R.; Meagher, R. J.; Barron, A. E.; *J. Am. Chem. Soc.*, ***2005***, 127, 7972-7973

8. Dobretsov, S.; Dahms, H. U.; Qian, P. Y.; *Biofouling*, ***2006***, 22, 43-54

9. Yebra, D. M.; Kiil, S.; Weinell, C. E.; Kim, D. J.; *Biofouling*, ***2006***, 22, 33-41

10. Berglin, M.; Wynne, K. J.; Gatenholm, P.; *Journal of Colloids and Interface Science*, ***2003***, 257, 383-391

11. Schmidt, D. L.; Brady, R. F.; Lam, K.; Chaudhury, M. K.; *Langmuir*, ***2004***, 20, 2830-2836

12. Pullin, R. A.; Nevell, T. G.; Tsibouklis, J.; *Materials Letter*, ***1999***, 39, 142-148

13. Bullock, S.; Johnson, E. E.; Willson, T.; Wynne, K. J.; *Journal of Colloids and Interface Science*, ***1999***, 210, 18-36

14. Brady, R. F.; Aronson, C. L.; *Biofouling*, ***2003***, 19, 59-62

15. Berglin, M.; Lonn, N.; Gatenholm, P.; *Biofouling*, ***2003***, 19, 63–69

16. Schmidt, D. L.; Coburn, C. E.; DeKoven, B. M.; Potter, G. E.; *Nature*, ***1994***, 368, 39-41

17. Brady Jr. R. F.; *Progress in Organic Coatings*, ***1999***, 35, 31-35

18. Brady, R. F.; Singer, I. L.; *Biofouling*, ***2000***, 15, 73-81

19. Chaudhury, M. K.; Finaly, J. A.; Callow, M. E.; Callow, J. A.; *Biofouling*, ***2005***,

21, 41-48

20. Truby, K.; Wood, C.; Stein, J.; Wendt, D. E.; Smith, C. M.; Montemarano, J.; *Biofouling*, ***2000***, 15, 141-150
21. Wood, C.; Truby, K.; Stein, J.; Wendt, D. E.; Montemarano, J.; Swain, G.; Meyer, A.; *Biofouling*, ***2000***, 16, 311-322
22. Wynne, K. J.; Swain, G. W.; Ulik, J.; *Biofouling*, ***2000***, 16, 277-288
23. Kavanagh, C. J.; Swain, G. W.; Montemarano, J.; Meyer, A.; Wiebe, D.; *Biofouling*, ***2004***, 19, 381-390
24. Hoipkemeier-Wilson, L.; Schumacher, J. F.; Callow, M. E.; Finlay, J. A.; Callow, J. A.; Brennan, A. B.; *Biofouling*, ***2004***, 20 53-63
25. Kim, J.;Nyren-Erikson, E.; Stafslien, S.; Chisholm, B. J.; *Biofouling*, ***2008***, 24, 313-319
26. Ramsay, D. B.; Dickinson, G. H.; Wahl, K. J.; *Biofouling*, ***2008***, 24, 109 – 118
27. Stein, J.; Truby, K.; Wood, C.; Wendt, D. E.; Smith, J.; Montemarano, J.; Meyer, A.; *Biofouling*, ***2003***, 19, 87-94
28. Gudipati, C. S.; Greenlief, C. M.; Johnson, J. A.; *J. Polym. Sci. A, Polymer Chemistry*, ***2004***, 42, 6193-6208
29. Gudipati, C. S.; Finlay, J. A.; Callow, J. A.; Callow, M. E.; *Langmuir*, ***2005***, 21, 3044-3053
30. Marabotti, I.; Morelli, A.; Orsini, L. M.; Jenko, M. ; *Biofouling*, *2009*, 25, 481-493
31. Cecchet, F. ; Meersman, B. D.; Jonas, A. M.; *Langmuir*, ***2006***, 22, 1173-1181
32. Ekin, A.; Webster, D. C.; Callow, J. A.; Callow, M. E.; *J Coat. Technol. Res*., ***2007***, 4, 435-451
33. Krishnan, S.; Ober, C. K.; Callow, E. M; *Langmuir*, ***2006***, 22, 5075-5086
34. Krishnan, S.; Ober, C. K.; Callow, E. M; *Biomacromolecules*, ***2006***, 7, 1449-1462
35. Unal, S.; Yilgor, I.; Yilgor, E.; Long, T. E.; *Macromolecules*, ***2004***, 37, 7081-7084

36. Pathak, J. A.; Twigg, J. N.; Roland, C. M.; *Macromolecules*, ***2008***, 41, 7543-7548

37. Chang, W. H.; Scriven, R. L.; Porter, S.; *Ind. Eng. Chem. Prod. Res. Develop.*, ***1973***, 12, 278-288

38. McMaster, D. M.; Bennett, S. M.; Detty, M. R.; *Biofouling*, ***2009***, 25, 21-33.

39. Yilgor, I.; Yilgor, E.; *Polymer Reviews*, ***2007***, 47, 487–510

40. Kajiyama, M.; *Macromolecules*, ***1990***, 23, 1244-1248

41. Shetha, J. P.; Yilgor, E.; Erenturk, B.; Wilkes, G. L.; *Polymer*, ***2005***, 46, 8185–8193

42. Harrell, L. L.; *Macromolecules*, ***1969***, 2, 607-612

43. Misra, R.; Fu, B. X.; Morgan, S. E.; *Journal of Polymer Science: Part B: Polymer Physics*, ***2007***, 45, 2441-2455

44. Schmidt, D. L.; DeKoven, B. M.; *Langmuir*, ***1996***, 12, 518-529

45. Uilk, J. M.; Mera, A. E.; Fox, R. B.; Wynne, K. J., *Macromolecules*, ***2003***, 36, 3689-3694

46. Lee, Y. L.; *Langmuir*, ***1999***, 15, 1796-1801

47. Meijer, M. D.; Haemers, S.; Cobben, W.; Militz, H., *Langmuir*, ***2000***, 16, 9352-9359

48. Tuteja, A.; Choi, W.; Cohen, R. E.; *Science*, ***2007***, 318, 1618-1622

49. Marmur, A.; *Biofouling*, ***2006***, 22, 107-115

50. Vo, L. T.; Giannelis, E. P.; *Macromolecules*, ***2007***, 40, 8271-8276

51. Schumacher, J. F.; Carman, M. L.; Callow, M. E.; Callow, J. A.; Finlay, J. A.; Brennan, A. B.; *Biofouling*, ***2007***, 23, 55-62

52. Majumdar, P.; Lee, E.; Chisholm, B. J.; *Polymer*, ***2009***, 50, 1124–1133

53. Dube, D.; Kim, K.; Alker, A. P.; *Mar. Ecol. Prog. Ser.*, **2002**, 231, 139–150

54. Petes, L. E.; Harvell, C. D.; Peters, E. C.; *Mar. Ecol. Prog. Ser.*, **2003**, 264, 167-171

55. Kim, K.; Dobson, A. P.; Harvell, C. D.; *Marine Conservation Biology*, 9, 149-166

56. Alker, A. P.; Kim, K.; Dube, D. H.; Harvell, C. D.; *Coral Reefs*, **2004**, 23, 397–405

57. McCallum, H.; Kuris, A.; Harvell, C. D.; *TRENDS in Ecology and Evolution*, in press

58. Harvell, C. D.; Mitchell, C. E.; Ward, J. R.; Altizer, S.; *Science*, **2002**, 296, 2158-2162

59. Jeffery, S. W.; Humphrey, G. F.; *Biochem. Physiol Pflanzen*, ***1975***, 167. 191-194

60. Thunemann, A. F.; Schutt, D.; Sachse, R.; Schlaad, H.; *Langmuir*, **2006**, 22, 2323-2328

61. Zhu, J. M.; Marchant, R. E.; *Biomacromolecules*, in press

62. Nie, F. Q.; Xu, Z. K.; Huang, X. J.; *Langmuir*, **2003**, 19, 9889-9895

63. Ulbricht, M.; Matuschewski, H.; Oechel, A.; Hicke, H. G.; *Journal of Membrane Science*, **1996**, 115, 31-47

64. Ishizone, T.; Han, S.; Hagiwara, M.; *Macromolecules*, **2006**, 39, 962-970